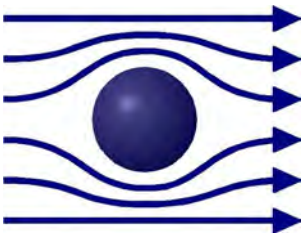

Walther-Meißner-Institut
für
Tieftemperaturforschung

Technische Universität
München

Bayerische Akademie
der
Wissenschaften

Transport measurements in 214 High-temperature superconductors

---

Diplomarbeit

Toni Helm

Themensteller: Prof. Dr. Rudolf Gross
Garching, 12. January 2009

Contents

Abstract

This thesis presents detailed c-axis magnetotransport measurements performed on a set of single crystals of the electron-doped 214 high temperature superconductor $Nd_{2-x}Ce_xCuO_4$ in steady (up to 28T) and pulsed (up to 65T) high magnetic fields. For the first time angle-dependent magenetoresistance oscillations (AMRO) and Shubnikov-de Haas (SdH) quantum oscillations have been observed in an electron-doped cuprate system. These results demonstrate a very high quality of the crystals grown in the Walther-Meissner-Institute and prove the existence of a well-defined Fermi surface in the bulk of the crystals, covering a large part of the phase diagram ranging from $x = 0.15$ (optimal doping) to 0.17 (strong overdoping). The AMRO observed in overdoped samples with $x = 0.16$ and $x = 0.17$ are qualitatively similar to AMRO reported for hole-overdoped $Tl_2Ba_2CuO_{6+\delta}$. For the doping level $x = 0.17$ high frequency SdH oscillations, originating from a large coherent Fermi surface cross-section, were found, which could not be seen in samples with lower doping levels. Instead, the sample with $x = 0.16$ exhibited SdH oscillations of low frequency. The latter originate from a small FS pocket, thus revealing a significant reconstruction of electron orbits, as compared to the $x = 0.17$ composition. Similar slow oscillations of a slightly higher frequency are found in measurements for an optimally doped crystal, with $x = 0.15$. The results obtained from the analysis are discussed in terms of a two-band model, related to an antiferromagnetic ordering and compared to the hole-doped cuprates.

Zusammenfassung

Die vorliegende Arbeit behandelt detaillierte c-Achsen-Transportmessungen, welche an einer Probenreihe von Einkristallen des Elektron-dotierten Hoch-Temperatur-Supraleiters $Nd_{2-x}Ce_xCuO_4$ in konstanten bis zu 28T hohen Magnetfeldern sowie in gepulsten bis 65T hohen Magnetfeldern durchgeführt wurden. Zum ersten Mal konnten winkelabhängige Magnetowiderstands-Oszillationen (AMRO) und Shubnikov-de Haas (SdH) Quantenoszillationen in Elektron-dotierten Kupratverbindungen gemessen werden. Diese Resultate bestätigen die außerodentlich hohe Qualität der im Walther-Meissner-Institut mittels Fließzonen-Verfahrens gewachsenen Kristalle. Und sie erbringen den endgültigen Beweis für die Existenz einer wohldefinierten Fermifläche im Kristall, wobei ein breiter Bereich des Phasendiagramms von optimal dotiert $x = 0.15$ bis hin zu stark überdotiert $x = 0.17$ abgedeckt wird. Die in überdotierten Proben mit $x = 0.16$ und $x = 0.17$ beobachteten AMRO's zeigen große Übereinstimmungen mit AMRO Daten, gemessen in Loch-überdotiertem $Tl_2Ba_2CuO_{6+\delta}$, auf. Für die Dotierung $x = 0.17$ wurden hochfrequente SdH Oszillationen gefunden, die auf eine große zusammenhängende Fermifläche schliessen lassen, für geringere Dotierungen aber nicht beobachtet werden konnten. Stattdessen zeigen sich für die Probe mit $x = 0.16$ niederfrequente SdH Oszillationen. Im Vergleich zu $x = 0.17$ ist diese Frequenz auf eine sehr kleine zusammenhängende Fermifläche zurück zu führen, was eine signifikante Rekonstruktion der Elektronenbahnen andeutet. Die gleichen langsamen Oszillationen, mit etwas größerer Frequenz, zeigten sich in Messungen für eine Probe mit otimaler Dotierung $x = 0.15$. Die von der Auswertung erhaltenen Daten werden hinsichtlich eines Zwei-Band-Modells in Verbindung mit antiferromagnetischer Ordnung diskutiert und mit Loch-dotierten Kupraten verglichen.

1 Introduction and motivation

1.1 High-temperature superconductors

During the last two decades enormous effort has been put into the investigation of the origin of high-temperature superconductivity (HTSC) in cuprate compounds. The principal question of how the pairing mechanism can be explained fundamentally had led to a large diversity of different experimental methods that have been applied or newly developed to examine this material group. Nevertheless the origin of HTSC could not yet be clarified satisfactorily.
It should be pointed out that the cuprates aside from superconductivity (SC) do reveal some interesting physics depending on doping that are covered within this material class. Thus, the major task is to distinguish between the properties that are coming from sample specific properties (like cleanness or homogeneity) and the one that are intrinsic to the cuprate superconductors in general.
It is well known that the cuprates have a layered crystal structure. Basically the number of copper-oxide-layers in the crystallographic elementary cell depends on the chemical composition. Thus, one divides the cuprates into families, see Table 1.1, where some examples for hole-doped cuprate compounds and their critical temperatures T_c are given. The very first found cuprate superconductors $La_{2-x}Ba_xCuO_4$ and $La_{2-x}Sr_xCuO_4$ belong to the Rare earth-214-compounds [1].

family	example	abbreviation	T_c [K]
Rare earth-based	$La_{2-x}Sr_xCuO_4$	(La214)	38
Yttrium-based	$YBa_2Cu_3O_{7-\delta}$	(Y123)	92
Bismuth-based	$Bi_2Sr_2CuO_{6-\delta}$	(Bi221)	10
	$Bi_2Sr_2CaCu_2O_{8-\delta}$	(Bi2212)	93
	$Bi_2Sr_2CaCu_2O_{8-\delta}$	(Bi2223)	110
Thallium-based	$Tl_2Ba_2Ca_2Cu_3O_{8-\delta}$	(Tl2223)	125
Mercury-based	$HgBa_2Ca_2Cu_3O_{8-\delta}$	(Hg223)	133

Table 1.1: Hole-doped cuprate families with critical temperature T_c for optimal doping level x

So far the dramatic variation in critical temperature from one family to another is not understood completely. The superconducting state in cuprates strongly depends on the carrier concentration that is the doping level x. Here one distinguishes hole doping on the one hand and electron doping on the other hand. The undoped parent compounds are electrical Mott insulators, which show antiferromagnetic (AFM) ordering of the Cu-ions within the CuO_2-layers. The correlations between critical temperature T_c and doping level are conflated in the schematic cuprate phase diagram (see Fig.1.1). It is constructed on the basic results of many different experiments applied to the various compounds. Still many features of this phase diagram are discussed controversally.

The Mott insulating state at $x = 0$ can be explained best by the Hubbard model, where a strong on-site Coulomb repulsion U is responsible for the splitting of the conduction band into a fully filled lower and an empty upper Hubbard band [2, 3]. Therefore, at $x = 0$ the Fermi energy lies in between the bands and an energy gap exists, which causes the insulating state.

SC sets in not until the electron concentration in the conducting planes is lowered by hole

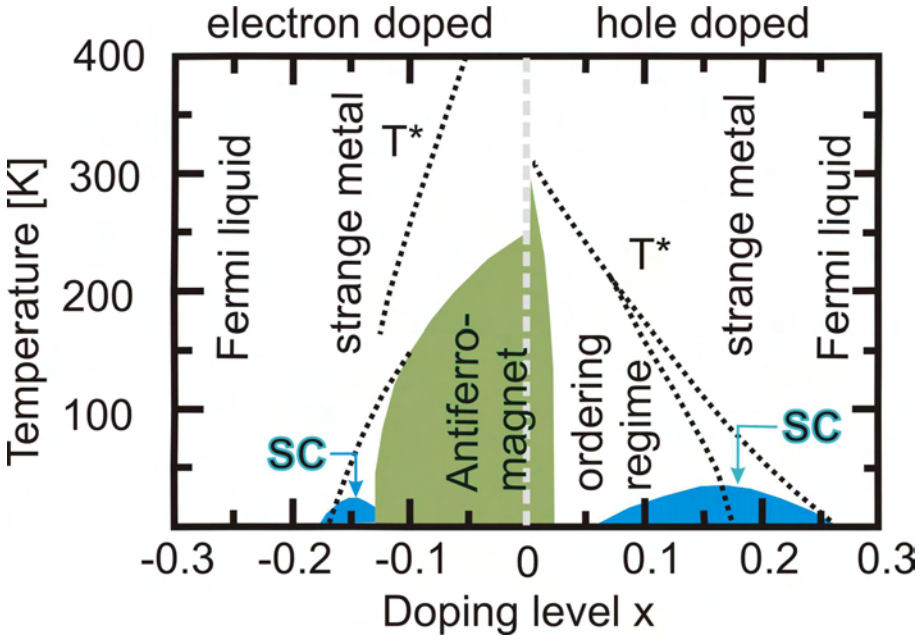

Figure 1.1: Schematic phase diagram based on data for the hole-doped $La_{2-x}Sr_xCuO_4$ and the electron-doped $Nd_{2-x}Ce_xCuO_4$, dashed lines indicate transition into an ordering regime, the so-called pseudogap state, which is discussed controversially. For example, if this ordering coexists with SC up to a quantum critical point or even throughout the whole superconducting range is not yet clear (indicated by the split line for the hole-doped side). For the electron-doped side it is reported to exist up to optimal doping level

doping. Thus, in terms of the Hubbard model, the Fermi level enters the lower Hubbard band. For example in $YBa_2Cu_3O_{7-\delta}$ doping is controlled by appropriate oxygenation. For this compound the oxygen content can be controlled with high accuracy. [4,5]. On the hole-doped side, it is generally accepted that SC arises for doping levels within $0.05 \leq x \leq 0.27$, with a maximum critical temperature at optimal doping $x = 0.16$.

The situation on the electron-doped side of the phase diagram is by far not as well understood. However, it is also possible to achieve SC in cuprate systems by increasing the electron concentration, which corresponds in terms of the Hubbard model, to a doping into the upper Hubbard band. The range $0.12 \leq x \leq 0.18$ in doping, where SC sets in, on the electron-doped side is more narrow compared to the hole-doped side and the highest critical temperature of $T_c = 25$K at optimal doping, $x = 0.15$, is comparably smaller. The 214 cuprate family of $Ln_{2-x}Ce_xCuO_4$, with the Lantanoides Ln=Nd, Pr, Sm as acceptor atoms, represents the electron-doped side. For as-grown crystals SC does not occur until they are annealed to high temperatures in low oxygen partial pressure, where the apical oxygen, located at sites between the CuO_2-layers is reduced to improve structural order. Recent studies show that this apex-oxygen rather affects the order of the crystal structure, which suppresses SC as well, than contributes to the doping [6].

The main problem of experiments has been the preparation of a set of high quality samples covering the full spectrum of the phase diagram. Thus, in earlier works the results depended strongly on sample quality and have not been very reliable. Due to a large progress in crystal growth and the sample quality of hole-doped crystals, this side of the phase diagram is now well examined. For the electron-doped cuprates a strong improvement in the sample quality has been achieved during the last years by using the traveling solvent floating zone (TSFZ) method for the crystal growth [6]. This opens new opportunities for investigations on the electron-doped side of the phase diagram.
Despite all efforts the underlying pairing mechanism of high-temperature SC in cuprates is still controversially discussed.

1.2 Experimental state of the art

At present, for both sides of the phase diagram, hole- and electron-doped, the main target of experimental activities has been to investigate the evolution of the electronic state from an AFM Mott insulator to a high temperature superconductor. One interesting effect, common for both sides, is in general the so-called pseudogap. This phenomenon can be understood as the appearance of an anisotropic suppression of electronic states near the Fermi energy level, originating from a not yet clearly understood ordering process. It is still unclear whether the pseudogap is related to SC being a precursor like performed pairs or whether it is not related to SC at all.
To investigate the electronic structure of cuprates, during the last five years several experiments in high magnetic fields on hole-doped compounds have found evidence for the existence of a well established Fermi surface (FS) in the normal state at different doping levels. In 2003 the effect of angle-dependent magnetoresistance oscillations was observed by Hussey et al. [7]. They studied electrical c-axis magnetotransport (current applied perpendicular to the copper oxide layers) in an overdoped $Tl_2Ba_2CuO_{6+\delta}$ (Tl2201) compound in steady magnetic field up to 45T. Fig.1.2a exhibits the data of this experiment, where they measured the inter-layer resistivity with respect to the field direction, which is determined by the polar angle θ and the azimuthal angle ϕ, as shown in the insert of Fig.1.2a. Their approach to simulate these data [8] was based on the existence of a large coherent quasi-two-dimensional FS, with a weak inter-layer coupling, enclosing about 2/3 of the first Brillouin zone, as shown in Fig.1.2b. Its overall shape and size were in agreement with band structure calculations and Hall measurements [9, 10].
In 2007 the first observation of Shubnikov-de Haas (SdH) quantum oscillations in underdoped $YBa_2Cu_3O_{6.5}$ (Y123-II) in 62T pulsed magnetic fields [12] brought evidence for a well established FS with small pockets, in contrast to the overdoped topology, and initialized a discussion, whether such pockets are compound specific or generic for hole-doped high-T_c superconductors. Before, angle-resolved photoemission spectroscopy (ARPES) as well as scanning tunneling microscopy measurements [11], like shown in Fig.1.2c for underdoped $La_{2-x}Ba_xCuO_4$, found signs of a fragmented FS in the underdoped regime, with fragments located at four narrow nodal positions. These methods do not see small pockets. Further works on Y123 [13] and Y124 [14] measured quantum oscillations, coming from FS pockets, supported the scenario of pockets being a generic property for hole-underdoped cuprates. Recently done torque measurements on underdoped Y123 even revealed two de Haas-van Alphen (dHvA) frequencies resulting from two different kinds of pockets at very low temperatures [15]. The latest publication reports the observation of a high frequency SdH oscillation in strongly overdoped Tl2201 (with $x = 0.30$) [16], giving evidence for the

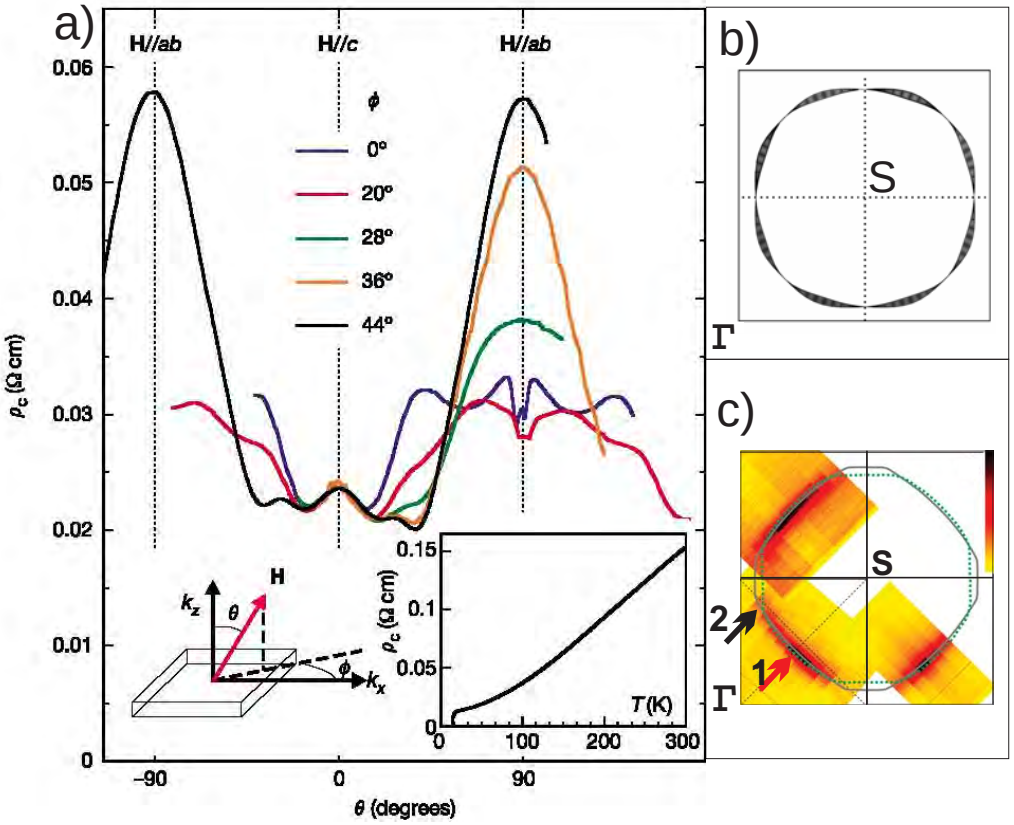

Figure 1.2: (a) AMRO data observed by Hussey et al. [7] showing the c-axis resistivity of hole-overdoped Tl2201 during turns from field parallel to the CuO-layers ($\theta = \pm 90°$) to perpendicular ($\theta = 0°$) for different azimuthal angles ϕ. (b) shows the suggested large coherent FS and (c) presents the energy gap mapping from scanning tunneling microscopy on $La_{2-x}Ba_xCuO_4$ [11], where the color black marks energy gap equal to zero

existence of a coherent large FS like suggested from the above mentioned AMRO in similar compounds.

On the electron-doped side the Fermi topology is not yet explored well. In past, the main problem has been a lack of high quality single crystals. In literature one finds a few publications about ARPES measurements on single crystals (grown with the TSFZ technique) from the far underdoped regime up to optimally doping level, $x = 0.15$ [17–21]. These measurements see a zone-diagonal spectral weight in the first Brillouin zone at $(\frac{\pi}{2a}, \frac{\pi}{2a})$ arising for doping levels above $x = 0.10$. One attributes it to a FS centered around $S = (\frac{\pi}{a}, \frac{\pi}{a})$, like it is shown in Fig.1.2 for $x = 0.13$, which has small fragments on the diagonal positions. Kusko et al. [22] succeeded in simulating this fragmented FS by the use of a two-band model, which was adopted by Millis et al. to explain there Hall data [23] . Recently done ARPES-studies [21] on a series of $Nd_{2-x}Ce_xCuO_4$ with $x = 0.13; 0.15; 0.16; 0.17$, observe a unusual change of the FS topology towards a closed FS orbit by increasing the doping level, see Fig.1.3.

As ARPES only can be applied on smooth surfaces, samples must be cleaved or well polished. In easily cleaved materials like for example hole-doped $Bi_2Sr_2CaCu_2O_{8-\delta}$ ARPES studies revealed similar FS fragments, looking like disconnected arcs [24]. At the same time, for underdoped yttrium-based compounds SdH and dHvA oscillations found clear

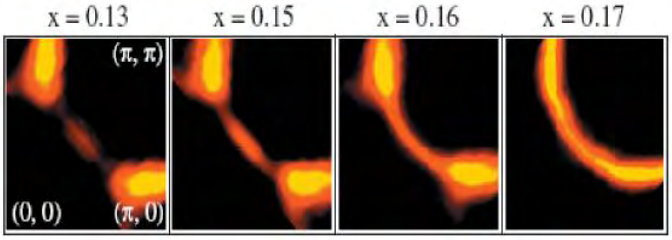

Figure 1.3: ARPES studies of the doping-dependent FS evolution on a series of electron-doped $Nd_{2-x}Ce_xCuO_4$ single crystals by Matsui et al. [21]

evidences for the existence of small pockets, which stands in contradiction to the arcs seen in ARPES. $YBa_2Cu_3O_{6.5}$ for example, is reported to have a self-doping of its surface due to polarity [25], which is a problem for ARPES, since it essentially is a surface and not a bulk sensitive technique. It was recently reported that ARPES results on the $Nd_{2-x}Ce_xCuO_4$ system depend on the energy of the used photons, hence, on the photon penetration depth [26]. However, even at the highest energy, the penetration depth does not exceed two CuO_2 layers, which does not guarantee probing bulk properties.
Therefore, a reliable experimental method, revealing bulk properties, is needed, to investigate the electronic structure of electron-like cuprates. Like already shown for hole-doped cuprates, magnetotransport studies in high magnetic fields can give a deep insight into the FS properties of the bulk. The recent discovery of magnetic quantum oscillations in those compounds gave a strong motivation for the high-field investigations of the electron-doped cuprates presented in this thesis. In the following, *c*-axis magnetotransport studies on $Nd_{2-x}Ce_xCuO_4$ single crystals are presented that reveal FS properties in the bulk of this material for different dopings x and contribute to the discussion above.

This work is constructed as follows:

The second chapter introduces the reader to the theoretical background of the high magnetic field effects studied in this thesis.

In third chapter the main properties and characteristics of the investigated compounds are presented.

The fourth chapter describes the particular experimental setups, which have been used during this work.

In the fifth chapter all data and the main results are exhibited, described and analyzed in detail.

The sixth chapter discusses the yielded data and compares them to the state of the art.

In the Conclusion the main results are summarized and a brief outlook is given.

2 Theoretical basics

2.1 Semiclassical electrons in magnetic fields

In the semiclassical model, an electron moving in a magnetic field $\mathbf{B}$ is subject to the Lorentz force bfF_L. The rate of change in the momentum of the electron $\hbar\dot{\mathbf{k}}$ is equal to the Lorentz force

$$\hbar\dot{\mathbf{k}} = bfF_L = -e\left(\mathbf{v}\times\mathbf{B}\right), \tag{2.1}$$

where, $-e$ is the electronic charge and v the electron velocity, B is the magnetic Field. The velocity of an electron is related to energy ϵ_k over

$$\mathbf{v}(\mathbf{k}) = \frac{1}{\hbar}\nabla_k\epsilon_{\mathbf{k}}, \tag{2.2}$$

where $\hbar$ is the reduced Planck constant, and stays always perpendicular to the Lorentz force. One immediately can see from Eq.(2.1)that only the component of the electron wave vector normal to the magnetic field is changing with time. Consequently, the electron moves in k-space along an orbit of constant energy perpendicular to the field. Here, only the situation of *closed orbits* will be discussed, but it must be mentioned that these orbits also can be open. In real space $\mathbf{v}$ has a component parallel as well as perpendicular to the field, thus the electron moves along a helical trajectory. The angular frequency with which the electron traces the orbit is called cyclotron frequency ω_c. From Eqs.(2.1) and (2.2) it follows that the time dt to traverse an element $d\mathbf{k}$ along the orbit in k-space is

$$dt = \frac{\hbar^2 d\mathbf{k}}{e\nabla_k\epsilon_k\times\mathbf{B}} = \frac{\hbar^2}{eB}\frac{dk\Delta k_\perp}{\Delta\epsilon_k}, \tag{2.3}$$

where $\Delta k_\perp$ is the change of wave component normal to $\mathbf{k}$ orbit in the plane perpendicular to $\mathbf{B}$, corresponding to a change $\Delta\epsilon$ of energy. Taking the area element $ds = dkk_\perp$ gives

$$dt = \frac{\hbar^2}{eB}\frac{\Delta\left(ds\right)}{\Delta\epsilon_k} \tag{2.4}$$

Integration over one complete orbit yields the time period of circulation, $T = 2\pi/\omega_c$ and, hence, the cyclotron frequency

$$\omega_c = \frac{2\pi eB}{\hbar^2}/\left(\frac{\partial s}{\partial\epsilon_k}\right)_{k_\parallel} = \frac{eB}{m_c}, \tag{2.5}$$

where the component $k_\parallel$ parallel to $\mathbf{B}$ is constant and

$$m_c = \frac{\hbar^2}{2\pi}\left(\frac{\partial s}{\partial\epsilon_k}\right)_{k_\parallel} \tag{2.6}$$

is called the cyclotron mass. For a gas of free electrons of mass m_e it follows

$$\epsilon_k = \frac{\hbar^2 k^2}{2m_e}, \tag{2.7}$$

where the constant energy surfaces are spheres with radius k. Because of the nature of the Fermi distribution only the energies close to the Fermi level are important and, thus, for a certain Fermi vector k_F this gives the Fermi energy $\epsilon(k_F)$. Here the cyclotron frequency is simply

$$\omega_c = \frac{eB}{\hbar m_e}, \tag{2.8}$$

where m_e is the electron mass.

2.1.1 Magnetoresistance in conventional metals

From Eq.(2.1) it is clear that the Lorentz force does not change the electron energy, since it is always perpendicular to the electron velocity. At low fields the electron momentum $\mathbf{k}$ does not change significantly during the scattering time τ, thus, the trajectory is only slightly curved. In this case, the radius of the curvature, called Larmor radius, $r_L = \hbar k_F/(eB)$ is much larger than the mean free path l. Hence, when $r_L >> l$, it is shown in literature [27] for the relative change in resistivity

$$\frac{\rho(B) - \rho(0)}{\rho(0)} \equiv \frac{\Delta\rho(B)}{\rho(0)} \propto \left(\frac{l}{r_L}\right)^2 \propto B^2 \tag{2.9}$$

At fields, at which the Lamor radius becomes smaller than the mean free path ($r_L \leq l$), the momentum of each individual electron will considerably change within the time τ. Therefore, the velocity $\mathbf{v_k} = \frac{\partial\epsilon(\mathbf{k})}{\partial\mathbf{k}}$ will vary depending on the momentum. To calculate the conductivity one has to solve the Boltzmann kinetic equation in the presence of electric and magnetic fields. Using the semiclassical τ approximation one obtains for the conductivity tensor:

$$\sigma_{\alpha\beta} = -\frac{2e^2\tau}{(2\pi\hbar)^3}\int \frac{df_0}{d\epsilon} v_\alpha(\mathbf{k})\bar{v}_\beta(\mathbf{k})d\mathbf{k}, \tag{2.10}$$

where α, β are the x,y,z-components and $\frac{df_0}{d\epsilon}$ is the equilibrium Fermi distribution function. $\bar{v}_\beta(\mathbf{k})$ is the velocity averaged over the scattering time:

$$\bar{v}_\beta(\mathbf{k}) = \frac{1}{\tau}\int_{-\infty}^{0} v_\beta(\mathbf{k}, t)e^{t/\tau}dt \tag{2.11}$$

Consequently, the conductivity is determined by the averaged velocity, which strongly depends on magnetic field. In the high field limit, $\omega\tau >> 1$ (or $r_L/l << 1$), the electron completes many turns around the closed Fermi surface and therefore the time averaged velocity tends to zero.

2.2 Landau quantization

The origin of de Haas-van Alphen oscillations is the quantization of the electron motion, which restricts the permitted states. We start from the Bohr-Sommerfeld quantization of a periodic motion

$$\oint \mathbf{p}\cdot d\mathbf{q} = (n+\gamma)\,2\pi\hbar\ ;\ n = 0, 1, 2...\ , \tag{2.12}$$

where $\mathbf{p}$ and $\mathbf{q}$ are the canonical conjugated momentum and position variables. γ is the phase variable which is exactly 1/2 for a parabolic band (case of free electrons) but in

general depending on energy and field it is slightly different. For an electron in magnetic field

$$\mathbf{p} = \hbar\mathbf{k} - e\mathbf{A} \; ; \; \mathbf{q} = \mathbf{r}_\perp, \tag{2.13}$$

where $\mathbf{A}$ is the vector potential of $\mathbf{B}$ and $r_\perp$ the vector in the plane of the electron orbit.

$$\oint (\hbar\mathbf{k} - e\mathbf{A})\, d\mathbf{r}_\perp = (n+\gamma)\, 2\pi\hbar \tag{2.14}$$

Integrating Eq.(2.1) with respect to time, so one can transform the first part of the integral. For the second part, Stoke's theorem is used, taking into account that the curl of the vector potential is the magnetic field. Therefore the integral is transformed into

$$\mathbf{B} \cdot \oint (\mathbf{r} \times d\mathbf{r}_\perp) - \int_{S_\perp} \mathbf{B} \cdot d\mathbf{S}_\perp = (n+\gamma) 2\pi\hbar/e, \tag{2.15}$$

where $d\mathbf{S}_\perp$ is the vector element of the area enclosed by $r_\perp$ in real space. $\mathbf{r}$ can be replaced with $\mathbf{r}_\perp$, because of the vector product any part of $\mathbf{r}$ parallel to $\mathbf{B}$ will give no contribution. This results in $\mathbf{B} \oint (\mathbf{r}_\perp \times d\mathbf{r}_\perp)$ for the first part, which is $2BS_\perp$ and the second part gives $-BS_\perp$. Thus (2.13) results in:

$$\Phi = BS_\perp = (n+\gamma) 2\pi\hbar/e, \tag{2.16}$$

which is nothing else but the magnetic flux Φ through the area ($\perp\mathbf{B}$) enclosed by the electron orbit quantized in terms of the universal *flux quantum*

$$\Phi_0 = \frac{h}{2e} \tag{2.17}$$

From Eq.(2.1) follows that

$$d\mathbf{r}_\perp = \frac{\hbar}{e\mathbf{B}} d\mathbf{k} \tag{2.18}$$

Hence, one easily gets the connection between the area of the orbit in real space $s_\perp$ to the one in the $\mathbf{k}$-space $S_\perp$

$$s_\perp = \left(\frac{\hbar}{eB}\right)^2 S_\perp \tag{2.19}$$

and consequently

$$S_{\perp,n}\left(\epsilon_k, k_{||}\right) = (n+\gamma)\, 2\pi e B\hbar, \tag{2.20}$$

where the area $S_\perp$ depends on the constant energy of the considered orbit and the value $k_{||}$ parallel to the field, marking the point at which the cross section is regarded. This is the **Onsager** relation (1952), which was derived independently by I. M. Lifshitz at about the same time but published two years later (Lifshitz and Kosevich 1954).
If $k_{||}$ is varied for a constant field B the orbits of constant energy will form a cylinder parallel to the field, the so-called Landau cylinder. Then the Onsager relation can be understood in the way that it restricts the allowed states in $\mathbf{k}$-space to lie on the Landau cylinders. Applied to the free electron gas, described by the parabolic dispersion Eq.(2.7) the Onsager relation yields:

$$\frac{\hbar^2}{2m_0}\left(k_x^2 + k_y^2\right) = (n+1/2)\, \frac{e\hbar}{m_e} B \tag{2.21}$$

in coordinates of the plane perpendicular to the field. This is the simple case of co-axial circular cylinders for free electrons (shown in Fig.2.1), which, in general, are not parallel to the field or even cylindrical. In zero field, the number of electronic states per unit volume of $\mathbf{k}$-space is $\frac{2V}{2\pi^3}$.

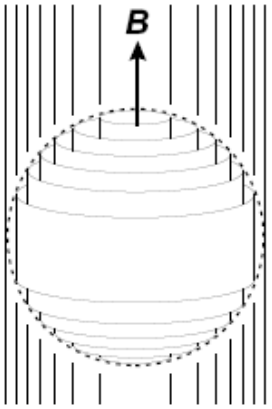

Figure 2.1: Co-axial Landau tubes parallel to the applied magnetic field in the case of free electrons

By switching on the field the allowed states are restricted to the Landau cylinders and, therefore, with

$$\Delta S = S_{n+1} - S_n = \frac{2\pi e}{\hbar} B, \tag{2.22}$$

the area in between two adjacent cylinders, one can estimate the number of states D lying on a Landau cylinder surfaces for a certain height to

$$D = \frac{\Delta S \Delta k_{||} V}{4\pi^3} = \frac{eV\Delta k_{||}}{2\pi^2\hbar} B \tag{2.23}$$

For experimentalists it is of interest at what rate, with increasing magnetic field, subsequent Landau cylinders leave the Fermi surface. From the Onsager relation Eq.2.20 follows:

$$(1/B_{n+1} - 1/B_n) = \frac{2\pi e}{\hbar} \frac{1}{S_{extr}}, \tag{2.24}$$

where S_{extr} is the cross section of the Fermi surface perpendicular to the field. Due to this fact physical quantities, depending on the density of states near the Fermi energy, show oscillations periodic in $1/B$, with the frequency

$$F = \frac{1}{\Delta(\frac{1}{B})} = \frac{\hbar}{2\pi e} S_{extr} \tag{2.25}$$

2.3 De Haas-van Alphen (dHvA) oscillations

In 1930 W.J. de Haas and P.M. van Alphen discovered oscillations in measuring the field dependence of the magnetization of bismuth at around 14.2K the evaporation temperature of hydrogen.
To understand this effect, one usually starts the magnetic field dependence of the thermodynamical potential Ω. The derivative of Ω with respect to field is

$$\mathbf{M} = -\left(\nabla_{\mathbf{B}}\Omega\right)_{\xi}, \tag{2.26}$$

where the chemical potential ξ is kept constant. For a system of conduction electrons obeying the Fermi-Dirac statistics, the thermodynamical potential Ω is given by the sum over all possible states ϵ

$$\Omega = -k_B T \sum_{\epsilon} \ln\left(1 + \exp\left(\frac{\xi - \epsilon}{k_B T}\right)\right), \tag{2.27}$$

where k_B is the Boltzmann constant. After including the degeneracy and energy eigenvalues E_n of the nth Landau levels this becomes

$$\Omega = -k_B T \int_{-\infty}^{\infty} dk_{||} \left(\frac{eHV}{2\pi^2\hbar}\right) \sum_{n} \ln\left(1 + \exp\left(\frac{\xi - E_n}{k_B T}\right)\right) \tag{2.28}$$

where the integral is taken over all the orbits defined by $k_{||}$. The solution of the integral above is done by using the Poisson summation formulas or the Euler-MacLaurin formulas. As a result one receives an oscillatory component of Ω:

$$\tilde{\Omega} = \left(\frac{e^5}{8\pi^7\hbar S''}\right)^{1/2} \frac{VB^{5/2}}{m_c} \sum_{p=1}^{\infty} \frac{1}{p^{5/2}} \cos\left[2\pi p\left(F/B - 1/2\right) \pm \pi/4\right], \tag{2.29}$$

where only slices in the vicinity of extremal areas add up constructively and

$$S'' = \left| \frac{\partial^2 S_{extr}}{\partial k_{||}^2} \right|_{extr}, \tag{2.30}$$

The components of **M** parallel to **B** are derived from the thermodynamical potential as followed:

$$M_{||} = -\left(\frac{\partial \Omega}{\partial B}\right)_{E_F} \tag{2.31}$$

Thus,

$$\tilde{M}_{||} = -\left(\frac{e^5 B}{2\pi^5 \hbar A''}\right)^{\frac{1}{2}} \frac{VF}{m_c} \sum_{p=1}^{\infty} \frac{1}{p^{3/2}} \sin\left[2\pi p\left(\frac{F}{B} - \frac{1}{2}\right) \pm \frac{\pi}{4}\right] \tag{2.32}$$

Until this point one can only model an idealized situation pretty far away from experimental conditions in reality. It becomes necessary to regard effects of finite temperature, finite relaxation time τ due to electron scattering and sample inhomogeneity, and effects of electron spin. All these effects give contribution in a form of reduction factors R_T, R_D, R_S (which have to be included in Eq.(2.32), leading to the *Lifshitz-Kosevich formula* for a three-dimensional electronic system with one extremal orbit.

$$\tilde{M}_{||} = -\left(\frac{e^5 B}{2\pi^5 \hbar A''}\right)^{\frac{1}{2}} \frac{VF}{m_c} \sum_{p=1}^{\infty} R_D R_T R_S \frac{1}{p^{3/2}} \sin\left[2\pi p\left(\frac{F}{B} - \frac{1}{2}\right) \pm \frac{\pi}{4}\right] \tag{2.33}$$

2.4 Damping factors

2.4.1 The effect of finite temperature

Due to the fact that absolute zero is never reached the Fermi distribution is smeared

$$f(\epsilon) = \frac{1}{1 + \exp\left(\frac{\epsilon - \xi}{k_B T}\right)} \tag{2.34}$$

This considered system at finite temperature T can be treated as a superposition of hypothetical metals at $T = 0$ with different Fermi energies distributed in the range of $\Delta\epsilon \sim k_B T$. Each of them contributes with a slightly different frequency which leads to a phase smearing and, hence, to a damping of the oscillation amplitude by

$$R_T(p) = \frac{2\pi^2 p k_B T / (\hbar\omega_c)}{\sinh\left[2\pi^2 p k_B T / (\hbar\omega_c)\right]} = \frac{Kp\mu T/B}{\sinh\left(Kp\mu T/B\right)}, \tag{2.35}$$

where p is the index of the harmonics and

$$\mu = \frac{m_c}{m_e} \tag{2.36}$$

is the cyclotron mass in dimensions of free electron mass and $K = 2\pi^2 k_B m_e/(\hbar e) \approx 14.69\text{T/K}$. Experimentally, one can extract the effective cyclotron mass directly out of the temperature dependence of the oscillation amplitude.

2.4.2 The effect of finite relaxation time

From the uncertainty principle $\Delta\epsilon \approx \frac{\hbar}{\tau} < \hbar\omega_c$ it is known that a finite relaxation time τ leads to a broadening of quantized Landau levels. So, compared to the temperature damping the damping, due to finite τ is expressed through the so-called *Dingle reduction factor*:

$$R_D = exp\left(-\frac{\pi p}{\omega_c \tau}\right) = exp\left(-Kp\mu T_D/B\right), \tag{2.37}$$

where

$$T_D = \frac{\hbar}{2\pi k_B \tau} \tag{2.38}$$

is the Dingle temperature out of which one gets the information about the scattering rate and thus about the mean free path of the sample.

2.4.3 The effect of electron spin

It was explained above that the Fermi edge smearing can be considered as a splitting in different levels which causes an extra damping R_T. Because of electrons having spin up and spin down in magnetic field, the Zeeman splitting lifts the spin degeneracy of the energy levels. Thus, each level splits in two $E_k \pm \frac{1}{2}\Delta E$ with a difference in energy of $\Delta E = g\mu_B B$, where $\mu_B = \frac{e\hbar}{2m_e}$ is the Bohr magneton and g the *Landé* factor (for free electrons $g = 2.0023$). The resulting reduction of the oscillation amplitude is expressed through

$$R_S = \cos\left(\frac{\pi}{2} p g \mu\right) \tag{2.39}$$

2.5 Shubnikov-de Haas (SdH) oscillations

The SdH effect basically originates from deviations of the τ approximation, taking into account different scattering processes, and is, therefore, more complex and more difficult to explain, see [28]. That's why we will not go too deep into the theory in this section. The SdH effect can be satisfactorily described by starting with Pippard's idea [29] that the scattering probability and, consequently, the resistivity are directly proportional to the density of states near the Fermi energy level $D(\epsilon_F)$. It can be shown ,see [30], that $D(\epsilon_F)$ is proportional to the field derivative of the magnetization. Thus the oscillatory part of the resistivity is given by:

$$\frac{\tilde{\sigma}}{\sigma_0} = \sum_{p=1}^{\infty} \frac{1}{p^{1/2}} a_p \cos\left[2\pi\left(\frac{F}{B} - \frac{1}{2}\right) \pm \frac{\pi}{4}\right], \tag{2.40}$$

where

$$a_p = \frac{m_c B}{S''^{1/2}_{extr}} R_T R_D R_S$$

is the oscillation amplitude and σ_0 is the background conductivity. Due to the direct relation to the dHvA effect, the same considerations for the damping factors, are valid in the case of SdH quantum oscillations.

2.6 Angle-dependent magnetoresistance oscillations (AMRO)

Due to several works in the field of organic superconductors during the 90s, the AMRO effect established as a powerful method to explore the Fermi surface geometry by using inter-layer magnetotransport, see Kartsovnik et al. [31]. In this section we consider a layered metal with a cylindrical Fermi surface. From Eq.(2.10) we know that the inter-

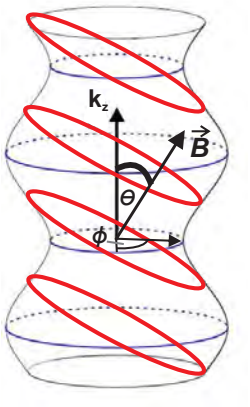

Figure 2.2: Corrugated cylindrical Fermi surface, θ is the polar angle with respect to the direction of the magnetic field, for a certain θ the cross-sections (grey) perpendicular to **B** *have the same area (red) independent of k_z, see [32]*

plane conductivity and, hence, the resistivity in metals with a cylindrical Fermi surface depend on the averaged electron velocity. From this, one would expect clear changes in the behavior of the resistivity by turning the magnetic field from the direction parallel to the conducting layers to perpendicular. Beside an obvious change from a regime with closed FS cross-sections to open orbits, along which the electrons traverse, a new effect has been observed for several layered compounds [31]. At certain polar angles θ the resistivity is enhanced. The first calculation for the polar angle positions, at which an AMRO maximum should appear for a cylindrical Fermi surface, was done by Yamaji [32]. He considered a simplified energy dispersion for a slightly corrugated cylindrical Fermi surface:

$$\epsilon(k) = \frac{\hbar^2}{2m}(k_x^2 + k_y^2) - 2t_\perp \cos(k_z d) \tag{2.41}$$

where $t_\perp << \epsilon_F$ is the interlayer overlap integral and d the interlayer spacing constant. He showed that for certain polar angles the cross-sectional orbit area (perpendicular to the magnetic field **B** becomes independent of the position in k_z-direction, see Fig.2.2. In the ideal case, all the cross-sections have the same area when

$$|\tan\theta| = \frac{\pi}{k_F d}(n - 1/4) \ ; \ n = 1, 2... \tag{2.42}$$

Eq.(2.42) is called "Yamaji's condition". AMRO are a semiclassical effect, that is why they can even be observed at conditions, where quantum oscillations are suppressed completely. Later on, it was Yagi et al. [33], who simulated AMRO by numerical integration of Eq.(2.10) and using the energy dispersion from Eq.(2.41). The physical nature of AMRO's is understood in the following. One can see from Eqs.(2.10),(2.11) that the conductivity

σ_{zz} depends on the velocity in k_z-direction averaged over one period of the motion on the cross-section perpendicular to the field. With Eqs.(2.2) and (2.5) for an electron traversing such an orbit, the mean velocity is

$$\overline{v_z} = \frac{1}{\hbar}\overline{\partial\epsilon/\partial k_z} = -\frac{\partial S(k_z)/\partial k_z}{\hbar\partial S/\partial\epsilon_{k_z}} = -\frac{\partial S(k_z)/\partial k_z}{2\pi\hbar m_c} \tag{2.43}$$

From this consideration it becomes clear that, if the orbit area becomes independent of the k_z-position, the velocity amounts to zero and, consequently, the conductivity shows a minimum. In real systems, the basal plane has typically a lower symmetry than circular and, additionally, the vector $h = (u_x, u_y, h_z)$ of the interlayer hopping has an in-plane component u. Thus Yamaji's condition Eq.(2.42) for maximums in the resistivity then has to be modified to [34]

$$|\tan\theta| = [\pi(n - 1/4) \pm (\mathbf{k}_\perp^{max} \cdot \mathbf{u})]/k_\parallel^{max} d, \tag{2.44}$$

where positive and negative polar angles θ are included with plus and minus, respectively. The vector $\mathbf{k}_\parallel^{max}$ lies within the plane perpendicular to $\mathbf{B}$ and $k_\parallel^{max}$ is defined as its projection in the direction of the field with maximum value. By applying this condition to field rotations in different planes (set by the azimuthal angle ϕ) perpendicular to the layers, one can derive the shape of the Fermi surface, in a non-circular case. This procedure is also called caliper measurement [35] because of its method of shape determination.

2.7 Magnetic breakdown

The topology of the Fermi surface is determined by the band structure properties of the material. As long as the cyclotron energy $\hbar\omega_c$ is much smaller than the relevant band energy around the Fermi energy ϵ_F, the electrons traverse along well established paths, like the above mentioned orbits. For high enough fields, electrons can tunnel, with a certain probability, from one band to another, if Δ_g, the gap between them, is sufficiently small. This effect is called *magnetic breakdown* [36] and the probability P of electrons to tunnel between the bands increases exponentially with increasing magnetic field:

$$P = \exp\left(-B_{MB}/B\right), \tag{2.45}$$

where B_{MB} is the breakdown field which can be estimated as

$$B_{MB} \approx \frac{m_c \Delta_g^2}{e\hbar\epsilon_F} \tag{2.46}$$

In other words, magnetic breakdown can be expected for conditions, where ´

$$\hbar\omega_c \gtrsim \Delta_g^2/\epsilon_F. \tag{2.47}$$

3 The 214 high-temperature superconductor $Nd_{2-x}Ce_xCuO_4$

The rare earth copper-oxides Re_2CuO_4 are AFM Mott-insulators, composed of two dimensional CuO_2 planes. This AFM correlations weaken by doping either holes or electrons into the conducting layers. This can be achieved by partly substitution of the rare earth by either higher or lower valent atoms. Restricting ourself to the electron-doped compounds like $Re_{2-x}Ce_xCuO_4$, with the Re=Pr, Nd, Sm. These compounds become superconducting upon doping with the 4-valent Ce atom. For this thesis a set of different doped high quality single crystals has been prepared, covering the whole superconducting range $x = [0.13 - 0.17]$ on the electron-doped side of the phase diagram. In the following the crystal structure of $Nd_{2-x}Ce_xCuO_4$, its difference to the hole-doped cuprates and the process of growing crystals with high quality is presented.

3.1 Crystal structure

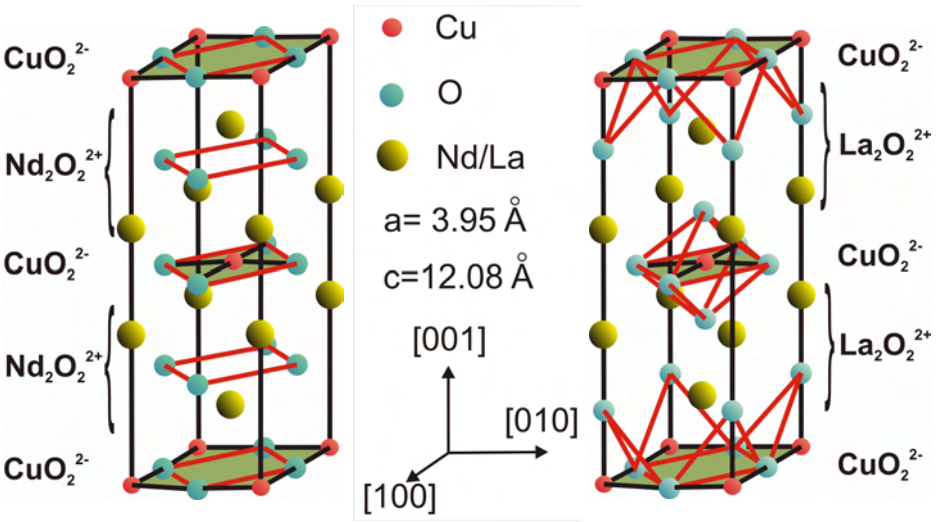

Figure 3.1: T' and T structure of electron- and hole-doped 214 cuprates, respectively

All electron-doped cuprates are based on the body centered (bc) tetragonal T'-Nd_2CuO_4 structure (with space group $I4 = mmm$), which is closely related to the T-La_2CuO_4 structure, typically for the hole-doped side. Both, T and T' structure can be regarded as an intergrowth of infinite, flat CuO_2^{2-} layers containing Cu in square planar coordination alternating with $Re_2O_2^{2+}$ layers. The conducting properties are governed by the CuO_2 layers, which are shifted by (1/2,1/2) to each other, resulting in a unit cell of double size. The rare earth oxide layers act as charge carrier reservoir and spacer for the CuO_2 layers. Thus, the single crystals are characterized by a strong in-plane to out-of-plane anisotropy

in electronic transport.
In the T-La_2CuO_4 structure the $La_2CuO_2^{-2}$ layers have the rock salt structure, that is why La has a total oxygen coordination number of 9. Therefore oxygen is located at the apical positions above and below Cu in the CuO_2^{2-} layers. In the center of the unit cell the, typical for cuprates, tetragonally distorted octahedral Cu-O coordination sphere is received, see Fig.3.1. Generally, this structure is called the perovskite structure, which most of the cuprates are based on. In contrast in the T'-Nd_2CuO_4 structure the $Nd_2O_2^{2+}$ layers have a fluorite structure with an oxygen coordination number of 8 for the rare earth atom, leaving vacant the apex oxygen position directly below and above the Cu ions, see Fig.3.1.

3.2 Crystal growth

Here, a brief introduction to the basics of the growing process of high quality $Nd_{2-x}Ce_xCuO_4$ single crystals is given. For further details about crystal growth and techniques see literature [37] The 214 compounds are incongruently melting solid solutions. They do not

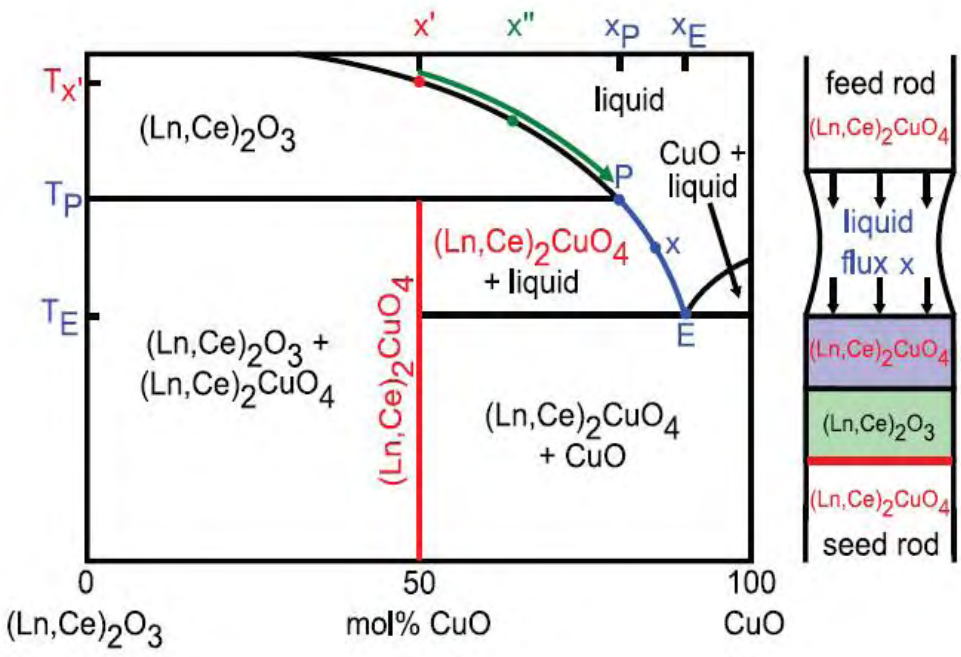

Figure 3.2: Left: 214 compositional phase diagram and the principle composition of a fed rod [6]; Right: A local vertical solvent zone of composition x is hold by surface tension between the seed and feed rod ("floating zone"). The 214 phase from the polycrystalline feed rod is dissolved continuously into the melt on the upper solid-liquid interface and crystallized on the lower liquid-solid interface. In equilibrium state the solvent traverses the polycrystalline feed rod ("traveling solvent") and on its bottom side the 214 single crystal is grown.

melt uniformly at a certain temperature, but decompose at the peritectic point P into a Ln_2O_3 phase and a liquid, rich in copper-oxide. In general, the formation of a peritectic phase takes place in systems with big differences in the melting points of the component phases. For the Ln_2O_3 - CuO system the melting points are reported at temperatures of $T > 2300°C$ [38] and 1100°C [39], respectively. To grow the 214 phase, which is stable at room temperature, special methods have to be applied. Looking into the compositinal

phase diagram in Fig.3.2, where the temperature and related phase boundaries are plotted versus the concentration, only the system $(LnCe)_2CuO_4$ - CuO is of importance. The liquidus line (blue line in Fig.3.2) between the peritectic point P and the eutectic point E marks the temperature and concentration range, where the 214 phase can be grown. At the eutectic point E two parameters are of interest. The lowest melting temperature in this phase diagram T_E and the eutectic concentration x_E, at which all components melt and crystallize simultaneously. The first reported single crystals, by Hidaka et al.(1989) [40] have been grown in crucibles. All commonly used crucible materials like refractory ceramics or noble metals are known to react with the aggressive melts and solutions of the copper oxide superconductors [41], introducing impurity atoms from the container material into the crystals. Another disadvantage of crucible growth for these solid solution systems is a inhomogeneous doping with Cerium. resulting from the fact that the distribution coefficient differs from unity. This, intrinsically, leads to a doping gradient in the crystals, grown from crucibles [42, 43].
The improvement in crystal quality is closely connected with the solution of these two main problems. Therefore, for our crystals the traveling solvent floating zone (TSFZ) technique was used. The functional principle of this technique is shown in Fig.3.2. The system consists of a feed and seed rod and a local solvent zone in-between. This vertical floating zone is only held by surface tension and has a composition x between E and P in the steady state growth process of the 214 phase. During growth polycrystalline feed material is dissolved continuously at the solid-liquid interface on the top and the material is transported within the solvent by diffusion and convection to the second solid-liquid interface at the bottom side, where the crystallization occurs. The molten solvent zone is traversed to the top of the feed rod by moving four parabolic mirrors, which act as the heat source, vertically to the top. As a result the solvent traverses slowly the feed rod, leaving behind a single crystalline rod. When using a flux pellet of composition x between P and E, steady state growth conditions can be reached from the beginning of the growth process. Otherwise, when starting with the 214 phase, $(LnCe)_2O_3$ is grown at first and simultaneously the solvent composition becomes richer of copper oxide, moving from x' via x'' to x_P, indicated by the green arrow in Fig.3.2, where the crystallization of the 214 phase sets in.
From the discussion above it is obvious that the modern TSFZ method has many advantages compared to flux growth methods using a crucible. The purity of the crystals is only affected by the purity of the starting materials and the contamination problems due to crucible corrosion are avoided. In addition, by using suitable growth conditions (oxygen partial pressure, flux composition, temperature, growth velocity) one can overcome the problem of an inhomogeneous Ce doping and large crystals of several centimeters in length can be grown under exactly the same conditions. This is the basic requirement for homogeneous crystals.

Annealing after the growth

This step is crucial for the superconducting properties of the 214 cuprates. To reduce tensions and disorder in the crystal structure the as-grown samples have to be annealed to temperatures close to the point of decomposition. For hole-doped crystals like $YBa_2Cu_3O_{7-\delta}$ the oxygen content and the doping, respectively, can be adjusted continuously within $0 \leq \delta \leq 1$ depending on the annealing parameters [4, 5].In the 214 crystals only a tiny amount of oxygen within $0.02 \leq \delta \leq 0.06$ can be removed/added without decomposi-

tion [44–47]. Nevertheless, this small amount of oxygen strongly affects the Nèel temperature as well as the transition temperature in the superconducting state [44, 45], although the doping is primarily governed by the Ce substitution. The general consensus of all these studies is that bulk superconductivity and sharp transition curves are only obtained by a severe reduction treatment very close to the stability limit of the compounds.

3.3 Advantages of electron-doped single crystals

One advantage of the electron-doped over the hole-doped compounds, with respect to our magnetotransport measurements, is their much lower upper critical field B_{c2}. Consequently, superconducting effects are expected to be less influential than in hole-doped cuprates with their high T_c and B_{c2} values [48]. For the preliminary characterization of our samples the available magnetic fields up to 15T perpendicular to layers are already high enough to access the normal state for all available doping levels at $T = 1.4$K, as the highest value of $B_{c2,\perp}$ derived from resistivity measurements [49] is stated to be at 10T for the optimally doped $Nd_{2-x}Ce_xCuO_4$ in fields perpendicular to the conducting layers. Another advantage is that the carrier concentration can be directly derived from the Ce content, which is precisely controllable during the synthesis. Finally, our compound offers the possibility to cover the whole SC range by only a small change in doping. This is particularly important for understanding hoe the electronic properties develop with doping within one system.

3.4 Doping dependent evolution of the Fermi surface for electron-doped cuprates

The conventional description of the motion of electrons in solids is in terms of electrons, propagating with a dispersion defined by a band structure calculation and modified by a self-energy function expressing the effects of interactions not included in the band calculation. Fig.3.3 shows the principle shape of the in-plane Fermi surface (FS), suggested for optimal electron-doping, $x = 0.15$. It is well fitted by the following band dispersion [50]:

$$\epsilon(\mathbf{k}) = -2t_1(c_x + c_y) + 4t_2c_xc_y - 4t_3(c_x^2 + c_y^2 - 1) + \alpha, \tag{3.1}$$

where $c_i = \cos k_i a$, a is the in-plane lattice constant and $t_1 = 0.38$ eV, $t_2 = 0.32 \cdot t_1$ and $t_3 = 0.5 \cdot t_2$ are the doping independent nearest neighbor transfer integrals. This dispersion is solved for: $\epsilon(\mathbf{k}) - \alpha = 0$, which corresponds, in the case of $\alpha = 0$, to optimal doping. Therefore, the doping dependence is adjusted over the parameter α. The parameters t_1, t_2 and t_3 have been obtained from band theory calculations for a class of hole-doped compounds by a "down-folding" procedure [51] and the band dispersion was derived from band structure calculations in $YBa_2Cu_3O_{7-\delta}$ by Andersen et al. [50]. The nearest neighbor integral values vary depending on the cuprate material family. Further evidence that these parameters provide a reasonable representation of the basic dispersion of the electron-doped materials comes from comparison to ARPES data , see Millis et.al [22, 23].
The FS is centered around $S = (\frac{\pi}{a}, \frac{\pi}{a})$ in the Brillouin zone. Due to the antiferromagnetism (AFM), existing in all underdoped cuprates, so-called hot spots become important in the Brillouin zone, see Fig.3.3. These are the crossing points of the AFM Brillouin zone

boundary and the FS, where the electrons undergo strong coherent backscattering with vector $Q = (\frac{\pi}{a}, \frac{\pi}{a})$. AFM arises due to the underlying spin-density-wave background from a certain AFM ordering of the copper spins in the conducting layers. For hole-doped compounds, spins order at relatively high temperatures ($T \leq 300$K) in a simple AFM colinear structure [52, 53], that doubles the crystallographic unit cell in the CuO_2 layers. Although the parent compounds of electron-doped copper oxides, such as Nd_2CuO_4, also have AFM spin structures, doubling the CuO_2 unit cell, the Cu^{2+} moments order to several phases with different AFM noncollinear spin structures depending on temperature and field [52–59]. These noncollinear spin structures appear in Nd_2CuO_4 because of the presence of magnetic exchange interaction between Cu^{2+} and Nd^{3+}.
In this regions the FS is gapped as long as AFM correlations are strong enough. Because of this FS fragmentation at the hot spot regions, the treatment of the electron-doped compounds within a two-band model is more appropriate than a single band description. Due to the strong backscattering of the charge carriers, the first Brillouin zone is folded and the levels are split by the energy gap 2Δ at the degeneracy points. This gap is proportional to the strength of AFM correlations, which obviously depend on the Ce content x. The new two-band dispersion is given by:

$$E_k^{\pm} = \frac{1}{2}\left[\epsilon_k + \epsilon_{k+Q} \pm \sqrt{(\epsilon_k - \epsilon_{k+Q})^2 + 4\Delta^2}\right], \tag{3.2}$$

where Δ represents a certain energy gap, which is due to the newly introduced ordering, where the electrons become subject to coherent backscattering with vector $\mathbf{Q} = (\frac{\pi}{a}, \frac{\pi}{a})$. ϵ_k corresponds to the original large FS, which exists for $\Delta = 0$ and ϵ_{k+Q} is the FS shifted due to the interaction with the AFM sublattice.
After lifting the degeneracy at the hot spots by 2Δ, a hole-like pocket centered the each quadrant of the first BZ as well as an electron-like pocket centered at $(\pm\frac{\pi}{a}, 0)$ and $(0, \pm\frac{\pi}{a})$ are formed. The doping dependent evolution of Δ and, hence, the evolution of the upper (+) and lower band (-) has been simulated by Kusko et al. [22] and has been compared to ARPES data. For the undoped parent compound in the Mott insulating state the Fermi energy lies within the band gap. Hence, the lower band is fully occupied corresponding to one electron per Cu ion. With increasing doping, the band gap is closing gradually. The upper band is crossing the Fermi energy, at first, at low doping levels and consequently small electron-like pockets appear. With further doping the electron pockets increase and change their shape from circular to square-like.

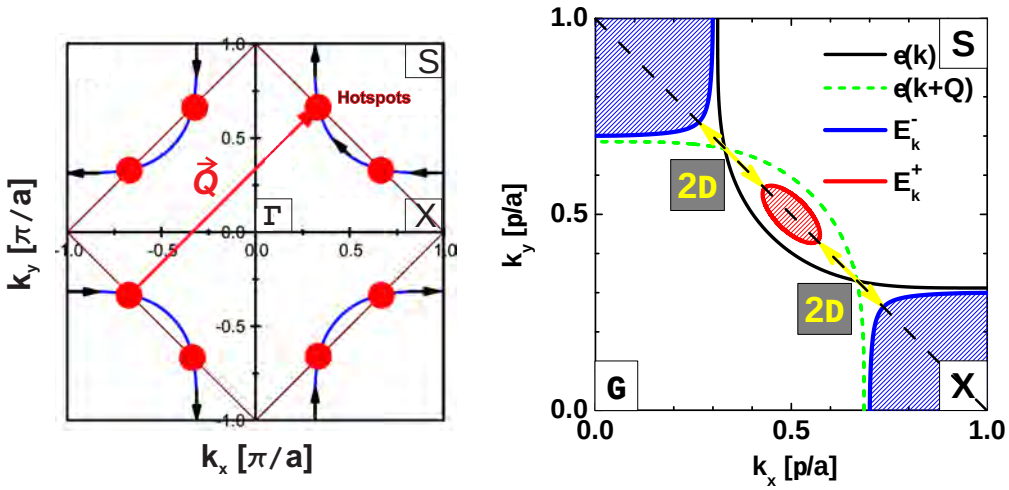

Figure 3.3: Left: The diamond shaped AFM in-plane Brillouin zone enclosing half of the first BZ. The red points indicate the hotspots, where electrons undergo backscattering with **Q**. *Right: Example FS derived from two band model with an existing gap* Δ *within the first quadrant of the Brillouin zone, showing electron-like pockets around* X *and hole-like around* $(\frac{\pi}{2a}, \frac{\pi}{2a})$

4 Experimental chapter

4.1 Sample preparation

Since the as-grown crystals, grown by the Traveling-Solvent-Floating-Zone technique, do not show SC in their as-grown state [1], all crystals, which were used in the experiments reported in this thesis, have been annealed under the same conditions to reduce the apical oxygen content. Fig.4.1left shows an as-grown single crystal rod, where the copper oxide layers are oriented parallel to the long side of the rod and the c-axis grows out sidewards. Therefore the dimension in c-direction of the samples is limited by the thickness of the rod. Within this thickness usually more than one grain is present. These are macroscopic regions of different growth direction, which have to be separated manually. Grain boundaries can be detected by a polarization microscope and samples were cut out of the rods in a way that they consisted only of one grain. With the help of a Laue camera the orientation of the c-axis (see Fig.4.1 right) and a-axis were determined within a precision of less than 0.5°. By gradually grinding of the a, b-surfaces an uniform thickness in c-direction is realized. In the last step four cuts perpendicular to each other, parallel to the a, c or b, c-plane, respectively, are set, yielding samples dimensions of $(a \times b) = (0.5 \times 1.0)\text{mm}^2$ for the surfaces and a thickness $(c = 0.1 - 0.4)\text{mm}^2$, depending on the grain size. These crystals receive a standard reduction treatment in an argon gas flow at 960°C for 20h to achieve sharp transitions in the zero field temperature curves followed by moderate cooling $(50 - 100\text{K/h})$ to room temperature.

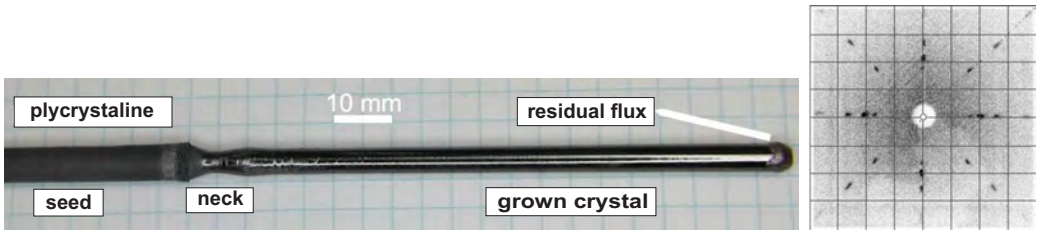

Figure 4.1: Left: a 6mm *thick polycrystalline feed rod with neck indicating the starting point of the growth process, the grown single crystal rod with its shiny surface and the eutectically solidified residual flux on the top; Right: Detected Laue back scattering shows the orientation of the c-axis [001] grown out sidewards*

Contacting and fixing the samples

Contacts with low ohmic contact resistances are crucial to get sufficiently low-noise signals with a small phase component. For the electrical contacts the silver paste Dupont 4929 was used. In order to get an adequate consistency, the paste is diluted with butyl acetate

[1] As-grown, optimally doped $Nd_{1.85}Ce0_{0.15}CuO_4$ crystals are already superconducting with a broad transition with $T_c < 10\text{K}$, when grown in an atmosphere of low oxygen partial pressure.

before contacting. Under an optical microscope Platinum wires of 20µm diameter are attached to the sample surface manually by using silver paste. The contact resistances achieved by simply drying under ambient conditions are in the range of several hundred up to kilo ohms. Therefore, the contacted crystals, including the wires, were cured by a heat treatment at 400°C for at least 1h in air, which leads to contact resistances of $10 - 50\Omega$. Note that this short heat treatment does not affect notably the oxygen content of the sample, since the oxygen mobility at this temperatures is very small in cuprates, see Erb et al. [60, 61].

It turned out that the samples feel a strong torque which is strongest for the super-

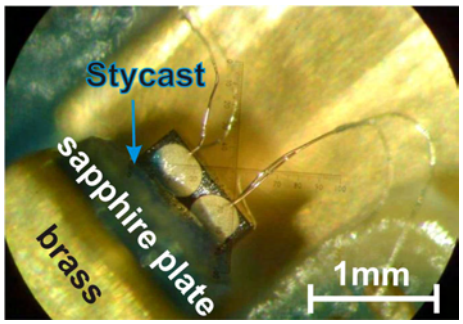

Figure 4.2: Contacted and mounted $Nd_{1.85}Ce_{0.15}CuO_4$ crystal $(1 \times 0.5 \times 0.15)\text{mm}^3$ *under the optical microscope*

conducting current perpendicular to the magnetic field. Therefore, we used Stycast 2850 FT as glue, prepared with Catalyst 24 LV, to fix the samples on a sapphire plate. Sapphire is chosen because of its perfect electrical insulating and good thermal conducting properties. Stycast 2850 FT is characterized by a high thermal conductivity, small thermal expansion and a low viscous consistency, before it hardens. Fig.4.2 shows a mounted $Nd_{1.85}Ce_{0.15}CuO_4$ sample.

4.2 High magnetic fields

Three different magnet sites have been used for the experiments of this thesis. In the following a brief overview is given of how high magnetic fields are produced. Usual magnets are coils of certain geometries which concentrate a homogeneous field in their center.

Superconducting magnets

To apply a steady magnetic field up to 17T, a superconducting magnet from Cryogenics was used in the Walther-Meissner-Institute. Two coils of different superconducting materials (Nb_3Sn for the inner and NbTi for the outer coil) are mounted co-axially on a common base and coupled in series. Cooling is realized by a bath of liquid ^4He surrounding the coils completely. To induce and adjust the field the coils are connected to an external current source ($0 \rightarrow 120$A). For experiments at constant fields the coils can be brought in the persistent mode. For that reason, the coil system is equipped with a superconducting shunt. During the charging of the coil this shunt has to be heated to become normal conducting, i.e. resistive. When the desired field is reached the shunt heating can be stopped and the external power supply disconnected. Thus very stable fields are achieved and the noise level is small, since the power supply is decoupled. The limiting factors for

superconducting magnets are the finite critical currents and fields of the coil materials. Today fields up to ≈ 21T can be achieved with superconducting magnets.

Resistive magnets

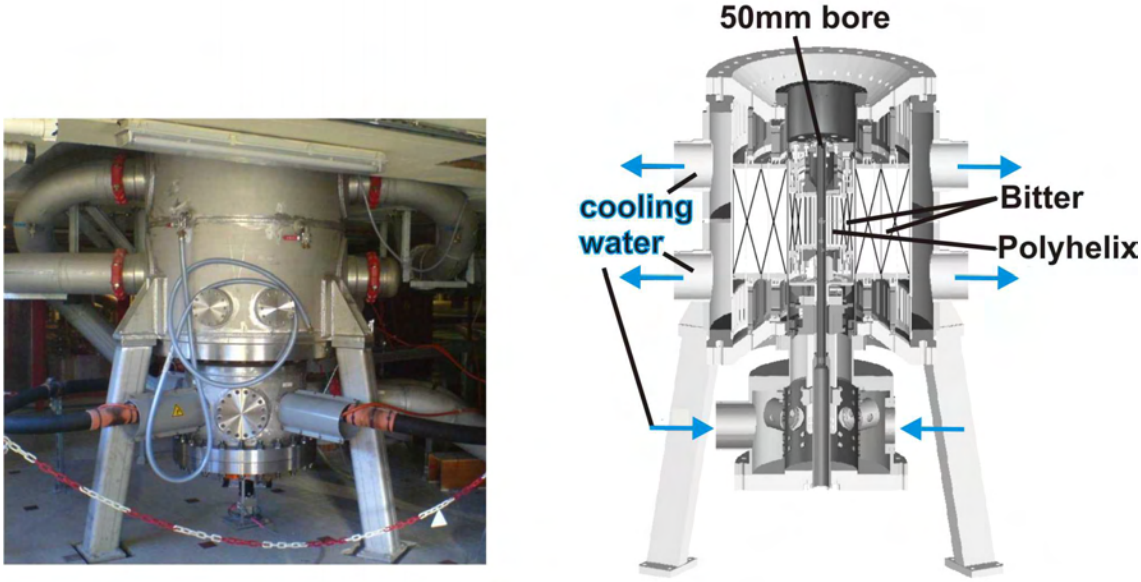

Figure 4.3: 28T *Magnet with bore diameter:* 52mm, *homogeneity:* $700 \times 10^{-6} cm^{-3}$, *power:* 24MW, *max current:* 31kA, *cooling water rate: up to* 280L/s

At present, magnetic fields above 21T can only be produced by resistive magnets. The need of large cooling systems and power supplies for the operation of such systems, however, makes the use of these kind of magnets expensive.
To keep the resistance as low as possible, the coils usually consist of copper or highly conducting copper alloys. In Grenoble a power of 24MW is needed for the current and the water cooling system to produce a field of 28T. Here the Joule heat produced in the coil by the electrical power is drawn off by deionized water, which flows under high pressure through gaps between the conducting material. This causes strong vibrations in the system, which result in a higher noise for the measurements. At such fields the coils must be constructed very robust to withstand the enormous Lorentz forces.

There are two kinds of resistive Magnets:

Bitter magnets

A Bitter coil is a stack of copper discs which are electrically isolated from each other, apart from a small segment of about 20°. Through drill holes, located parallel to the coil axis, deionized water is pumped with high pressure for the cooling. A problem of these Bitter coils is the radial distribution of the current, which cannot be influenced, but is inversely proportional to the distance from the coil axis.

Polyhelix magnets

A polyhelix coil consists of several copper coils fitted coaxially into each other. The advantage in comparison to the Bitter magnet is, that the current density can be optimized radial to the field. Fig.4.3 shows th 28T magnet system used in Grenoble, which consists of a combination of a polyhelix surrounded by two Bitter coils. Since the power, necessary for the cooling and magnet operation, is proportional to the squared field value, highest fields with resistive magnets are limited due to technical and financial reasons. Hybrid magnets, a combination of a resistive coil surrounded by a superconducting magnet can even produce higher fields, above 40T. The American National High Magnetic Field Laboratory is running such a hybrid magnet, with an at the moment unique maximum field of 45T. Fields above 50T can only be achieved by pulsed field techniques, where one can apply much higher currents for only short pulses in the range of few milliseconds to a second.

Pulsed field magnets

In principle, the coils used in pulsed fields (see Fig.4.4a) consist of several hundred windings of copper-niobium wire and ten to twenty layers with high electrical isolating material in between. For the necessary high currents in the coils one needs a power source, which can produce high currents for a short time scale. In the High Field Laboratory Dresden a high energy capacitor bank, keeping up to 50MJ, is used. The maximum voltage of 24kV is then transferred over thyristor switches into the coil, what results in up to 400kA discharge currents. The high thermal power of up to 5GW to the coils follows from the extreme energy input $Q = \int_0^{t_{pulse}} R(T(t))I(t)^2 dt$, where t_{pulse} is the pulse duration and I the discharge current. Since for such short time scales no efficient permanent cooling can be provided, the energy must be absorbed completely by the coil system. Hence, the coil is immersed completely in a nitrogen reservoir and kept at 77K.

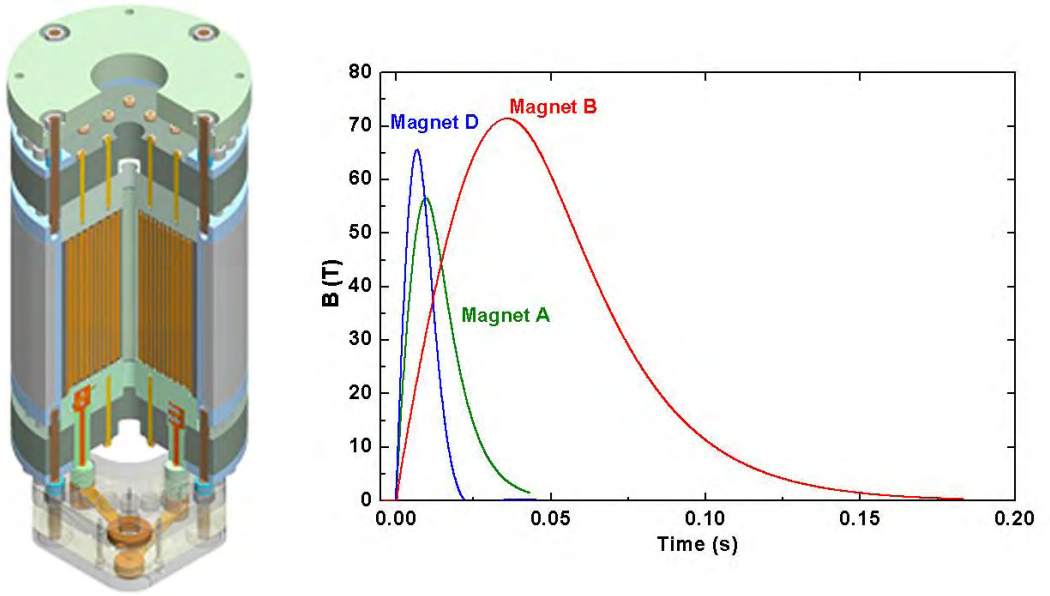

Figure 4.4: Left: 67T pulsed field coil; Right: pulsed field profiles for three different coils available in Dresden, Magnet B was the one used in our experiments (up to $B = 65$T)

4.3 Measurement systems

For the measurement of the inter-layer resistance the standard a.c. four probe method is used. Four contacts are attached to the sample, two on each side parallel to the a, b-plane. One pair of opposite contacts is used to apply the current and the other to measure the induced voltage, see Fig.4.5. This method makes it possible to measure the pure interlayer resistance without the contributions of the contact resistances. Due to the layered crystal structure our cuprate compound shows a large anisotropy in the conductivity for current within or perpendicular to the conducting CuO-layers. The anisotropy ratio is [6]

$$\frac{\rho_c}{\rho_{ab}} \approx 10^4$$

with the inter-layer resistivity $\rho_c = U/I \cdot (ab)/c$ this would correspond to an isotropic system with similar ab-surface area of $(0.5 \times 1.0)\text{mm}^2$ but a thickness of $c \approx 1 - 4\text{m}$. Taking this into account, in our case the current can be regarded as uniformly distributed over the whole bulk.

For the current supply a high ohmic resistor R_2 was set in series to the internal a.c. voltage generator of the Lock-In amplifier[2]. Hence, the a.c. current can be set by adjusting the output voltage from the Lock-In. The reference resistor R_1 of 10 or 100Ω is connected in series to the sample. Thus, the a.c. current can be precisely adjusted and one can be checked if there is any out-of-phase component, showing capacitive contributions. To provide equal conditions, during the measurements in Garching and Grenoble the applied current was always set to 0.1mA with a frequency of $f \approx 300\text{Hz}$. Because of the large resistance value of R_2 compared the sample resistances at room temperature, the change to zero resistance in the superconducting state affects the current by less than 1%, and therefore guaranties a stable current during the whole experiments.

For the pulsed field experiments in Dresden a similar set-up was used with the difference that during the short time-window of $t_{pulse} \approx 0.2\text{s}$ for one pulse, see Fig.4.4b, the raw a.c. voltage signal from the sample has been recorded by an oscilloscope with a sampling rate of $1\mu\text{s}$. The signal is than processed by laboratory self-developed programs using the same technique like the lock-in does. The main advantage is that one can play with the raw data, trying to optimize the signal after the pulse, whereas with the Lock-In one has to make many pulses, playing "try and error", in order to optimize the signal. It should be noted here that the cooling of the coil after a pulse to highest field takes at least four hours, and thus "try and error" would be very time-consuming.
As we were looking for oscillations, we applied higher a.c. currents of $0.5 - 1\text{A}$ and a frequency of 67kHz. This increased the local heating of the contacts on the sample slightly. The temperature in the sample was than evaluated by comparing the critical field, at which superconductivity was suppressed with former measurements at known temperature.

4.4 Two axis rotator

For the angle-dependent resistance measurements a two axis rotation insert is available, which fits to the VTI used in Garching and to the one designed for Grenoble as well. Fig.4.6a exhibits the lower part of the insert dismantled in its components. The rotation is provided via two worm gear units, an outer and an inner part. The sample holder is

[2]In our case we used the Stanford Research devices SR850 and SR830

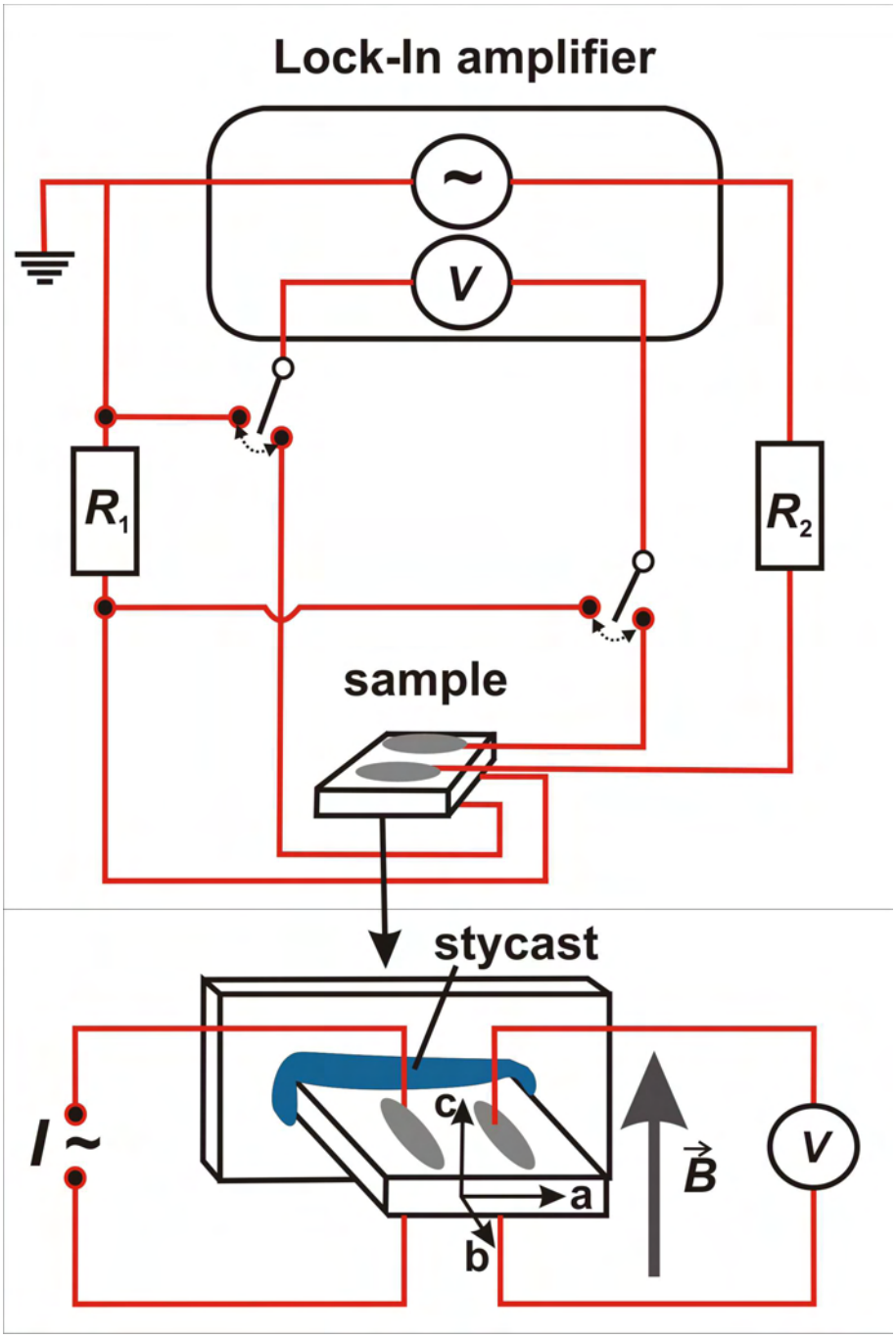

Figure 4.5: (top) Block-diagram of the measuring set-up with a variable reference resistor $R_1 = 10, 100\Omega$ *and excitation resistor* $R_2 = 1, 10, 100\text{k}\Omega$*. The sample voltage is measured by using a Lock-In SR 850 / Sr830; (bottom) Illustration of a contacted sample glued with Stycast 2850 FT (blue) on a sapphire plate,* $20\mu\text{m}$ *thick Platinum wires are attached by using the silver paste Dupont 4929 to the ab-surfaces*

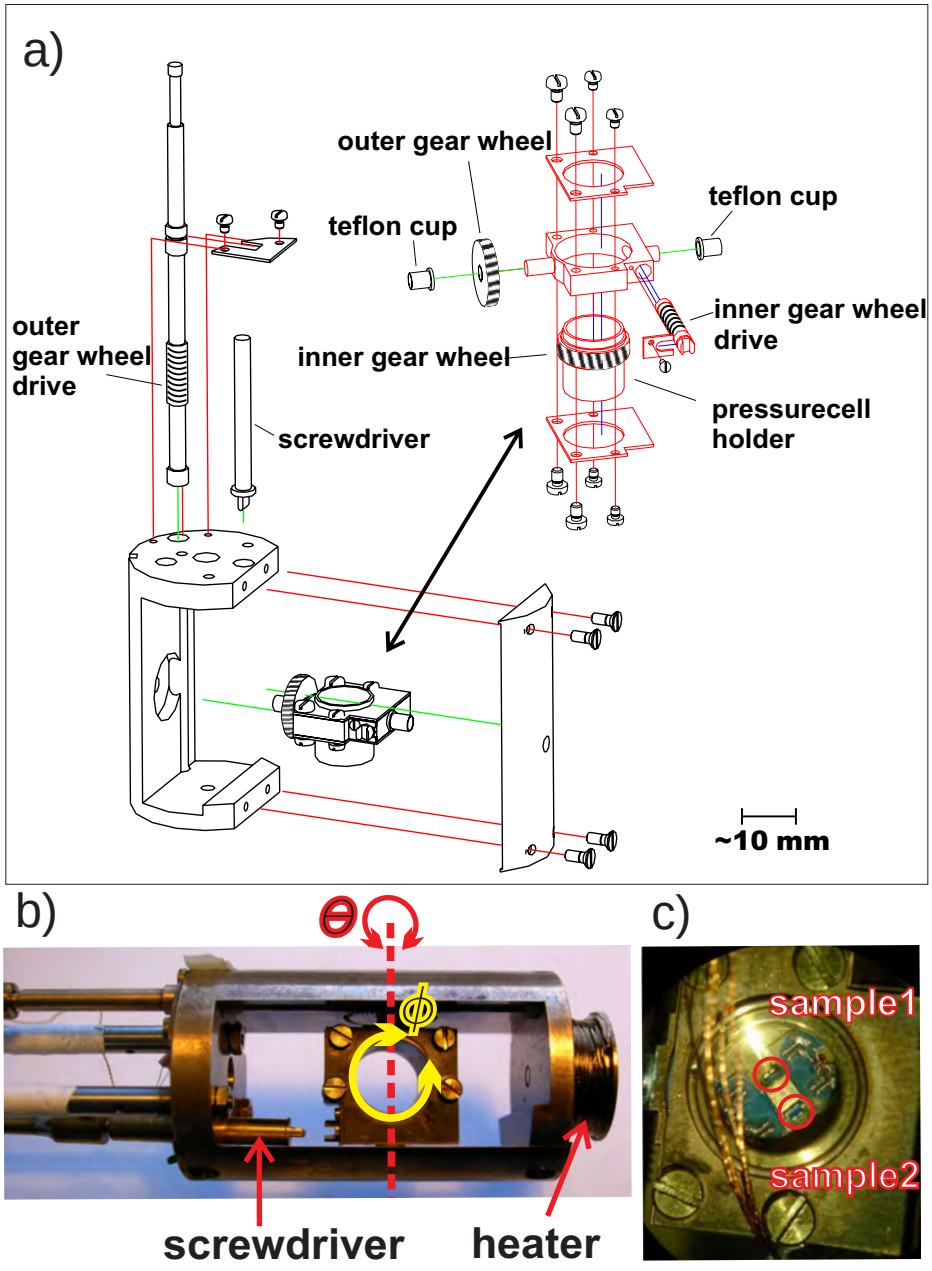

Figure 4.6: a) Explosion drawing of the two axis rotator for angle-dependent measurements; b)Photo of the two axis rotator with introduced rotation angles; c) Sample holder with two samples mounted with the CuO-layers parallel to the rotator platform

fixed inside the inner worm wheel, see Fig.4.6c. Therefore the azimuthal angle ϕ of the cylindrical sample holder is adjusted by the inner rotation. The whole inner part is rotated by the outer worm gear, setting the polar angle θ between the axis of the platform and the magnetic field direction. Thus, one can align a sample in any possible position with respect to the magnetic field. While the outer worm axis is always directly connected to the top of the insert the inner gear must be disconnected during a θ-scan. Thus, if one wants to change the azimuthal position of the sample within the inner rotation unit, the inner worm axis has to be put to the vertical direction (by changing the angle θ)

and a screwdriver, that can be pushed down, has to "catch" the slit on top of the inner worm drive. To turn our samples from the field perpendicular to the field parallel to the conducting layers position, they have been mounted with the c-axis directed perpendicular to the rotation unit. The metal to metal friction on the suspension points is avoided by the use of additional teflon cups placed in between. All the other components in Fig.4.7 are made out of brass. Both angles can be set to an accuracy of $\leq 0.05°$. A piezo-electric motor, stable against the stray field of the magnets, drives the θ rotation axis. Due to a limited speed range of the latter an additional mechanical gear is placed on the top of the insert. The sweeping rate of the sample rotation can thus be continuously changed in a range of $[0.003 - 10]°/s$. The angle rotating axis is coupled by a V-belt to a variable multi-turn resistor, hence, the measured resistance is proportional to the polar angle and is digitized to plot immediately the resistance versus the angle θ.

4.5 Low temperatures, measurement and controlling

For each experiment the method of temperature control and stabilization had to be adjusted to the given dimensions of each magnet site. Here a brief overview is given of the used systems.

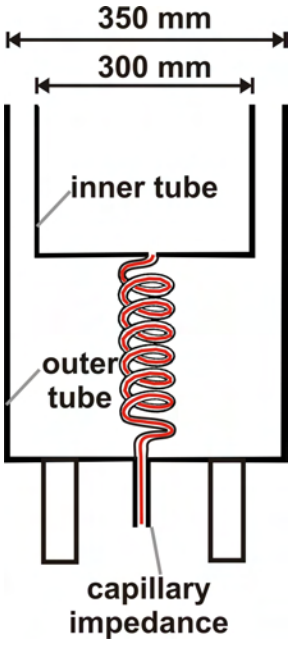

Figure 4.7: Principle of a VTI, Impedance

In the Walther-Meissner-Institute (WMI), a cryostat from Cryogenics has been available, where the 17T superconducting magnet is immersed completely in a reservoir of liquid ^{4}He. To allow a continuous control of the temperature from 1.4K to 300K a variable temperature insert (VTI) was used, see Fig.4.7. It consists of a long tube fixed into a bigger one, where the space in between them can be evacuated or filled with an exchange gas. This assures that the space of the inner tube, where the sample is placed, is thermally decoupled from the environment (in our case the ^{4}He bath). The only connection to the environment, after the dipstick including the sample is put inside the cryostat, is a long, very thin CuNi-capillary ($\Phi_i = 0.65$mm), wound to a spiral at the bottom. As it is filled with a smaller manganese wire ($\Phi = 0.44$mm) inside, it builds a capillary impedance, which results in a constant weak helium flow, when the VTI is submerged into the helium bath. While the inner tube is continuously pumped, a 60Ω resistor, placed next to the sample, is used to adjust a certain temperature over the heating power. The heater control and temperature monitoring is performed with the help of a Lake Shore 340 temperature controller, measuring the resistance of a calibrated Cernox resistor, with a precision of a few mK. For low temperatures between $4.2 - 1.4$K the heater is kept off and due to the continuous pumping the sample space becomes filled with liquid. Temperatures simply are set by adjusting the pressure. Stable temperatures up to 80K are controlled by the heater power in presence of constant helium gas flow. Here temperature sweeps with a ramp speed of $[0.3 - 3]$K/min can be performed. To reach 300K the VTI must be taken out of the helium bath to stop the helium flow.

A similar VTI has been built in the the work shop of the WMI, fitting to our two-axis rotator and to the dimensions of the cryostat in Grenoble, where the 52mm bore hole of the magnet restricts the size of the cryostat and namely of the VTI, too. Thus it was

possible to do angle-dependent resistance measurements in 28T for stable temperatures between $[1.4 - 50\text{K}]$. To guarantee as stable temperatures as possible, during the field sweeps in Grenoble a capacitance sensor was used, because the Cernox shows a weak field dependence. For a sweep to 28T at $[1.4 - 4.2]$K the resistance of the Cernox resistor is found to increase to a value corresponding to a temperature increase of ≤ 0.5K. Whereas in this temperature range no heater is necessary and the uncertainty, originating from the Cernox resistor, does not affect the measurements, because temperature is stabilized by setting the pressure in the sample space, for field sweeps above 4K the capacitance sensor was chosen as reference.

4.5.1 Temperature control in pulsed fields

During the pulsed field experiments a VTI was used, too. However, this time the helium flow could be controlled by a variable needle valve.
There are two possible modes to set the lowest temperature. In the continuous flow mode the needle valve is kept open, the gas flow is set to a constant low value and the sample space is pumped to the lowest temperature. Here the sample is surrounded by gas. In the single shot mode the sample space is filled with liquid at 4.2K, by keeping the pumping rate high for a while with the needle valve fully open, until the sample is immersed in liquid helium completely. Right before the pulse the needle valve is closed and due to constant weak pumping the temperature slowly decreases. When it reaches 1.4K, the pulse is initialized immediately. The main difference of the two modes is the coupling of the sample to the environment. When the sample is immersed in liquid helium a heating, induced by eddy currents or magnetization, during the pulse can be transfered easier than by an exchange gas. On the other hand a liquid transmits vibrations (producing noise) from the coil better than an exchange gas.

5 Experimental data and analysis

In this chapter, the most important data, obtained in the present work, are presented. First, the main characteristics, such as transition temperatures and critical fields, are shown to justify the quality of the samples. Of high importance for the following high field experiments are parameters like conductivity, homogeneity and doping. Comparing them to the properties of hole-doped cuprates, studied in the experiments described in chapter 1.2, helped to evaluate the chances for the observation of similar effects and features in our $Nd_{2-x}Ce_xCuO_4$ samples.
The second part shows the results of angle dependent resistivity measurements for different doping levels in steady magnetic fields up to 28T in the Grenoble High Magnetic Field Laboratory. Each data sets are described and analyzed in detail. The third part exhibits, what was done in pulsed magnetic fields up to 65T in the Dresden High Magnetic Field Laboratory and gives a detailed description of the data and applied analysis.

5.1 Preliminary characterization of samples

In this section a short overview is given about characteristic properties of the examined samples in c-axis magnetotransport measurements in magnetic fields up to 15T. Because of the recent new results in very high fields, presented in the further sections, here the discussion of the preliminary data is kept very short and only some important issues are highlighted. In Fig.5.1 one can find the temperature-dependence of the interlayer resistivity and its evolution at different magnetic fields for each regarded doping level. The transitions temperatures T_c are resolved in the insets.
The zero field resistivity (black curves) shows for all four doping levels a gradual transition from linear (at high temperatures) to an almost quadratic shape (at low temperatures). For $x = 0.13$ the slope changes sign at 50K. This turning point shifts down to below 20K for optimal doping and below 10K for $x = 0.16$ and is not visible any more for the composition $x = 0.17$, which, therefore, seems to be most metal-like. A broad transition would indicate significant doping variations, but all the transitions are within a narrow range of about $2 - 3$K. For $x = 0.13$, SC can be suppressed completely by applying magnetic fields of 10T perpendicular to CuO_2 layers. This critical field tends to drop down rapidly by increasing doping. For $x = 0.15$ it is already below 6T, for $x = 0.16$ below 5T and in the sample with 17% doping level SC is already suppresed at a field of 0.5T.

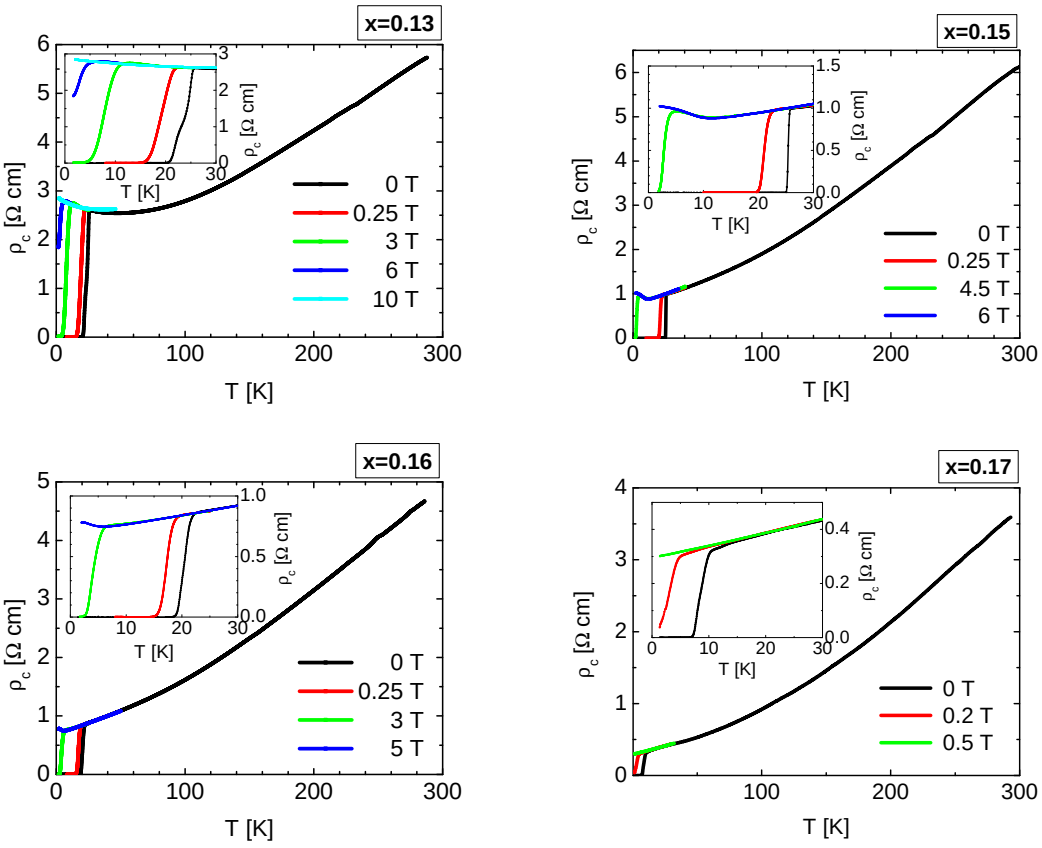

Figure 5.1: c-axis resistivity versus temperature for four different doping levels (black curves); Inset: transition curves for each doping level at different constant fields perpendicular to the layers (colored curves)

Fig.5.2 shows the critical fields depending on temperature for each examined doping level. At temperatures above 25K there is no trace of SC in c-axis magnetotransport any more. At $x = 0.15$ for lowest temperatures an upturn with its maximum at 13.5T shows up, which seems to be shifted to 5T for $x = 0.16$ at 1.4K. Also for $x = 0.13$ right after the transition a weak upturn is discernible. For $x = 0.17$ the slope is positive in the entire field range. These transitions, recorded in the $R(B)$ sweeps up to 15T, were later used for estimating the actual temperature during the pulseed field measurements in Dresden.

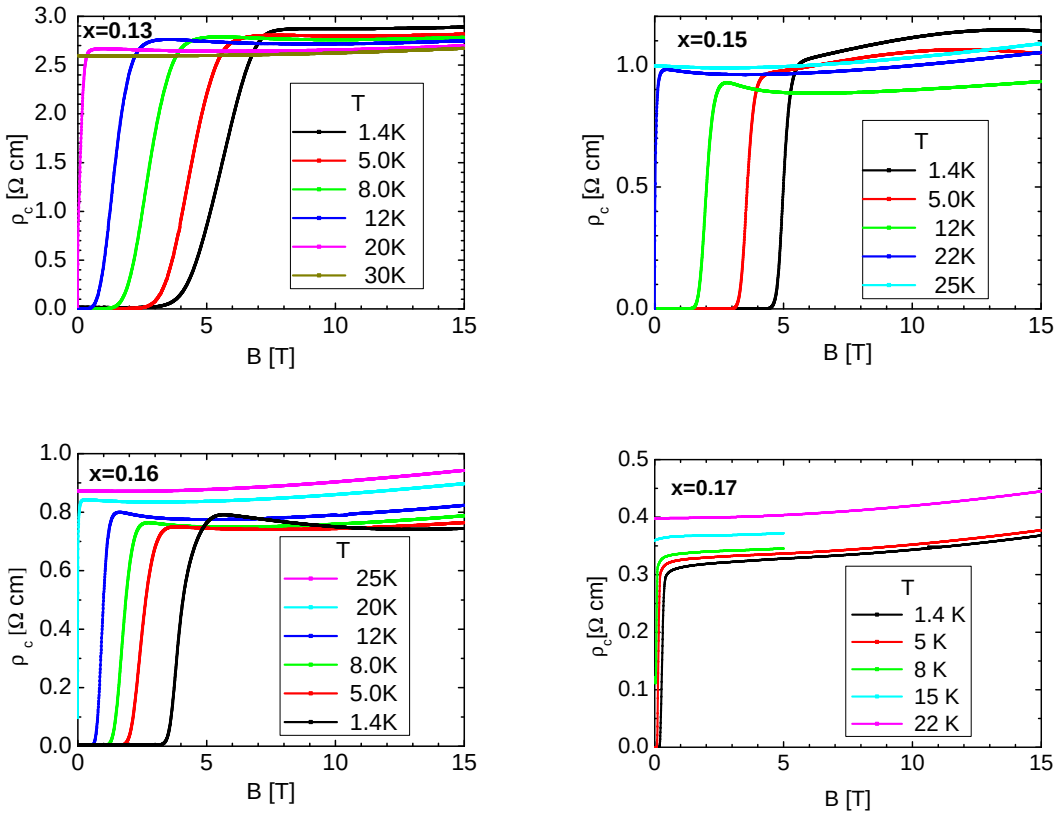

Figure 5.2: c-axis resistivity versus magnetic field (applied perpendicular to the layers) for four different doping levels at different temperatures

Fig.5.3 exhibits two θ-scans at $T = 1.4K$ and $B = 15$T for two different ϕ of overdoped $Nd_{1.83}Ce_{0.17}CuO_4$. The rotation was performed by employing the two-axis rotator, described in the Section 4.4. Due to the design of the rotator, ϕ can only be changed for fixed θ with the rotator platform in vertical position. Therefore, ϕ is fixed during one whole θ-scan. By turning from $\theta = -90°$, what corresponds to $B \parallel$ a,b-plane, the resistivity increases rapidly, up to 3% of $\rho_c(\theta = 0°)$, at $\theta = -75°$, where it starts to decrease again. This maximum is strongly ϕ-dependent and shows a periodicity in 45°. It enhances up to 2.5% at $\phi = 0°$ compared to $\phi = 45°$. At $\theta = 0°$ a second maximum arises with 9% lower resistivity than at $\theta = -70°$ and is independent of ϕ. The inset shows how this hump evolves with field at $T = 1.4$K, here the curves are shifted more near to each other and the function value is, therefore, given in arbitrary units. At fields below 10T no maximum can be seen at this angle. Comparing the shape of the resistivity, plotted versus the polar angle θ, we find many similarities to the AMRO data on Tl2201, already shown in Fig.1.2 of the introduction.

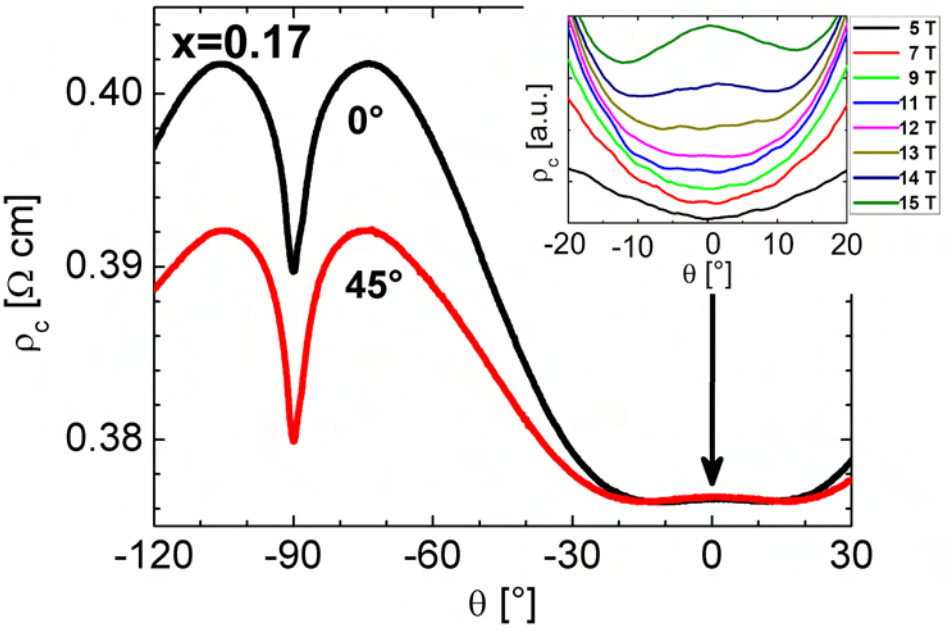

Figure 5.3: Resistivity versus θ at $B = 15$T and $T = 1.4$K; Inset: the field dependence of the hump at $\theta = 0°$, in arbitrary units, because the curves are shifted close to each other by hand for a better illustration

5.2 Steady magnetic fields up to 28 T

5.2.1 AMRO for strongly overdoped samples, $x = 0.17$

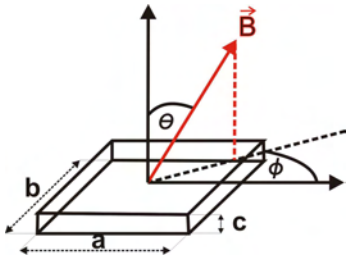

Characteristic angles and axes

So far, for cuprates, angle-dependent magnetoresistance oscillations (AMRO) only have been observed for hole-overdoped Tl 2201 compounds, see Fig.1.2a [7]. Because of promising preliminary characterization data in fields up to 15T (Fig.5.3) in Garching, we chose the doping level $x = 0.17$ for our first θ-scans in a steady high magnetic field of 28T. This is the maximum possible level in electron-overdoping for liquid solution grown $Nd_{2-x}Ce_xCuO_4$ high quality single crystals. Due to the construction of the rotator's sample holder, two samples could be measured simultaneously. So, we measured two samples of the same doping level and were able to check immediately, that the features we see are specific to the sample and not due to noise.
In Fig.5.4 the θ-scans for one sample with 17% doping level for different ϕ-positions in a

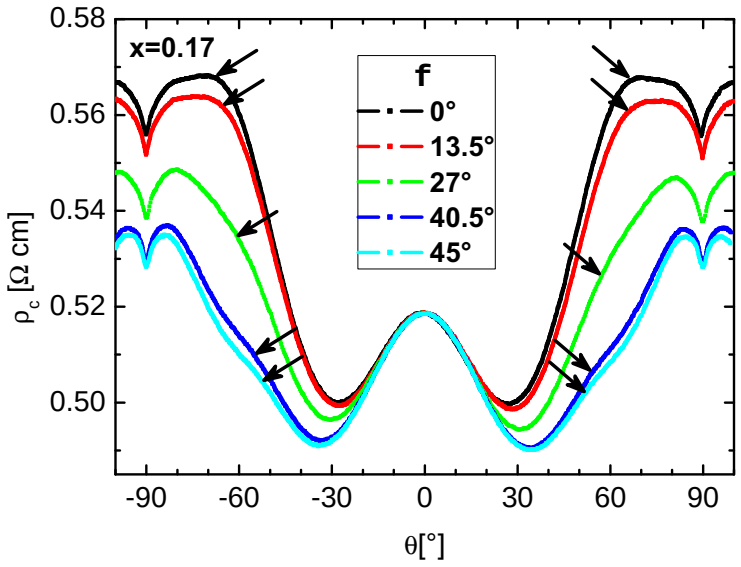

Figure 5.4: $x = 0.17$, Resistivity plotted versus the polar angle θ for different ϕ-settings at lowest possible $T = 1.3$K and highest field $B = 28$T; The arrows mark the positions of the new feature.

magnetic field of 28T are shown. The simultaneously measured second sample reproduces all observed features, but the noise was too strong, so that only plots of sample 1 are used for the discussions below. The general shape of the angular dependence in a magnetic field of 28T is similar to that obtained from scans in fields up to 15T, shown in Fig.5.3. Still, the dip in the resistivity curve at $\mathbf{B} \parallel a,b$-plane, which we relate to remanence of superconductivity, shows up. With increasing magnetic field, obviously the hump becomes more pronounced as compared to the sweeps in 15T. At changing ϕ, the resistivity curves above $\theta = 20°$ and below $\theta = -20°$, respectively, deviate from each other. At $\theta = \pm 90°$ for $\phi = 0°$ the resistivity is enhanced by up to 5% compared to $\phi = 45°$. Additionally, for ϕ set to 45° a new feature becomes clearly visible arround $\theta = 53°$. Actually, this feature, although less pronounced, exists also at other ϕs but at different polar angles θ.
Next to check was how the features depend on temperature and magnetic field and to find out, if they might be related to the AMRO effect, coming from the Fermi surface topology, or to some different origin. In Fig.5.5 one can see that the dip at $\theta = 0°$ slowly loses its deepness by increasing the magnetic field. At present there are still discussions about B_{c2} in electron-doped cuprates. Newest experiments [62], using quasiparticle tunneling across $La_{2-x}Ce_xCuO_4$ grain boundary junctions to probe the superconducting state and its disappearance with increasing temperature and magnetic field, do not even rule out traces of SC to persist up to 25T. Indeed, for our compound we find traces of superconductivity for fields up to 28T, applied perpendicular to the layers. The hump becomes more obvious, as the resistivity around $\theta = 30°$ grows slower with increasing field. It has already been shown, see Fig.5.3, that the hump around $\theta = 0°$ turns into a minimum for fields below 10T at the lowest temperature. The feature at $\theta = 53°$ becomes visible above 18T for $T = 1.3$K and vanishes at temperatures above 20K, see Fig.5.6.

As far as we see from Fig.5.5 and 5.6, the 53° feature, indicated by vertical dashed lines, does not change noticeably its position by changing magnetic field or temperature. This indicates its origin in the Fermi surface geometry. Indeed, the overall angle dependence

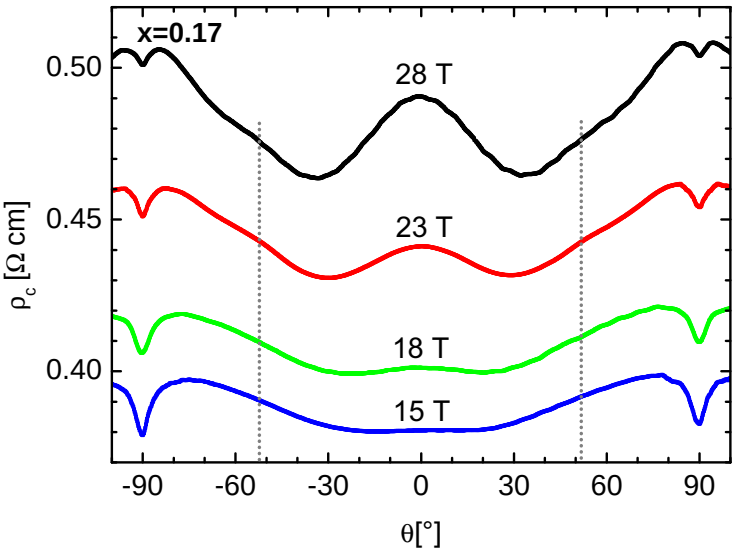

Figure 5.5: $x = 0.17$, θ-scans for different magnetic fields with ϕ set to 45° and $T = 1.3$K

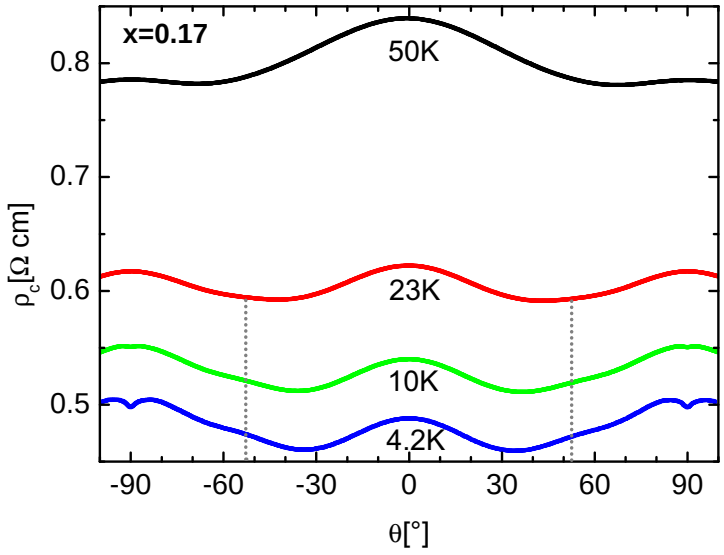

Figure 5.6: $x = 0.17$, θ-scans for different temperatures with ϕ set to 45° and $B = 28$T

and the features look very similar to those observed by Hussey [7] in the hole-overdoped Tl2201 compound. We, therefore, suggest our feature originates from the real AMRO effect. Namely, it corresponds to an AMRO maximum satisfying the conditions - see Eq.(2.44) - presented in the AMRO section of the theory chapter. The origin of the hump at $\theta = 0°$ we do not yet relate to AMRO, see discussions.

To extract the evolution of the AMRO feature with respect to different ϕ, the second

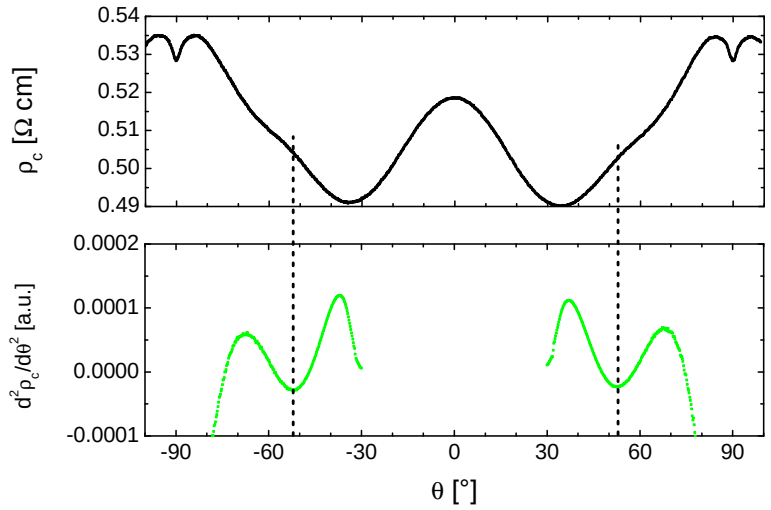

Figure 5.7: $x = 0.17$, The second derivative (green curve), revealing the AMRO position by a local minimum, for $T = 1.3$K, $B = 28$T, $\phi = 45°$ is given as an example.

derivative $\frac{d^2\rho_c}{d\theta^2}$, which gives a minimum at maximum curvatures, was calculated. An illustration is given in Fig.5.7, where the second derivative was calculated for polynomial fits of the original curve at angles between $\theta = 30°$ to $80°$ and $\theta = -30°$ to $-80°$, respectively. θ-scans for seven different azimuthal positions $\phi(0°, 13.5°, 27°, 40.5°, 45°, 54°, 67.5°)$ have been performed and analyzed. For angles of $\phi = 0°$ and $13.5°$ the AMRO feature is very smooth, see Fig.5.1, and therefore hard to locate by applying the second derivative. Thus, the coordinates for these angles could only be estimated tentatively by eye and need to be determined more precisely in higher fields. Fig.5.8 shows the obtained coordinates.

5.2.2 AMRO for moderately overdoped samples, $x = 0.16$

How do changes in doping level affect the newly observed AMRO feature? To answer this question a set of two samples with a doping level of 16% was measured next.

The following results are completely taken from one and the same sample, the second sample showed the same curves and features, but will not be mentioned further on. Fig.5.9 exhibits the data of θ-scans at four different ϕs. The overall shape of the resistivity curve is similar to the one for $x = 0.17$ (shown in Fig.5.4), except that the sample remains superconducting up to 28T for polar angles in the interval $\pm 10°$ around the field direction parallel to the a, b-plane. We observe again the feature similar to that, attributed to AMRO effect, in 17% doped samples. It becomes most pronounced for $\phi = 45°$ at $\theta \approx 50°$ and moves up to $\theta \approx 63°$ for $\phi = 0°$. Unfortunately, it is not as pronounced as in the samples with 17% doping level. Thus, the AMRO positions can only be estimated tentatively.
This time the AMRO feature becomes visible not before 23T, see Fig.5.10, and whether its position changes, depending on field, could not be clarified.
The next similarity to $x = 0.17$ is that for $-90 \leq \theta \leq -20°$ and $+20° \leq \theta \leq 90°$ the resistivity enhances by changing ϕ from $45°$ to $0°$,too (see Fig.5.9). At the maximum

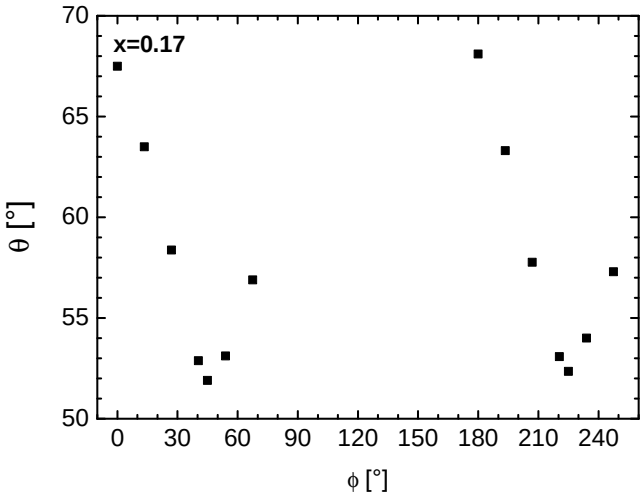

Figure 5.8: $x = 0.17$, Positions of the AMRO feature for different ϕs for the in Fig.5.4 exhibited θ-scans

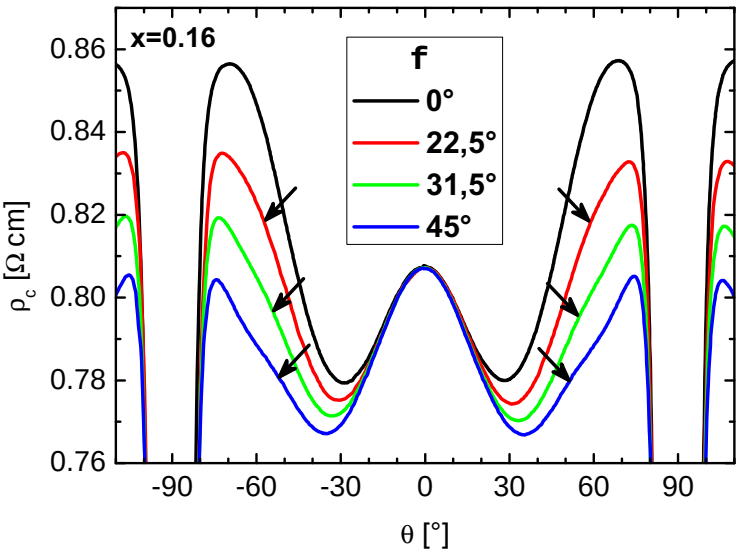

Figure 5.9: $x = 0.16$, θ-scans for different ϕ settings at $T = 1.3$K and $B = 28$T; Arrows mark the AMRO feature positions

resistivity, that is the point around $\theta = 70°$ right before SC sets in, the enhancement is about 6% for $\phi = 0°$ compared to $\phi = 45°$.
At increasing temperature, the ϕ dependence of the resistivity weakens and almost vanishes at around 23K, as one can see in Fig.5.11. There the temperature-dependence for two ϕ settings is shown and the position of the AMRO feature does not show changes for different T, as indicated by dotted gray lines. Here, one important finding is that at higher temperatures, the ϕ-dependent background, which makes it difficult to determine the position of the AMRO correctly, seems to flatten out faster than the AMRO-feature.

So, for example at 10K, it is possible to determine the position of the AMRO feature for $\phi = 0°$ easier. This fact we have not realized during the measurements, thus for future experiments this offers a chance to obtain more detailed information about the evolution of the AMRO positions over the full ϕ-range.

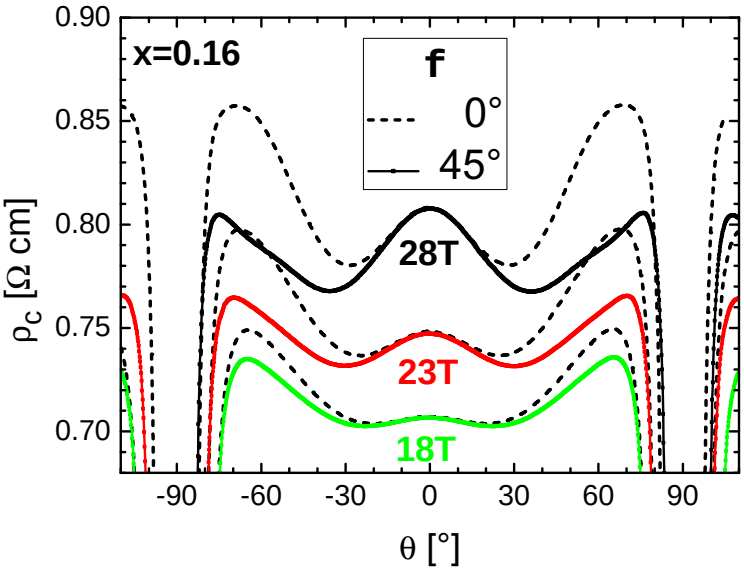

Figure 5.10: $x = 0.16$, θ-scans for different fields with $T = 1.3$K at $\phi = 0°$ (dashed lines) and 45° (solid lines)

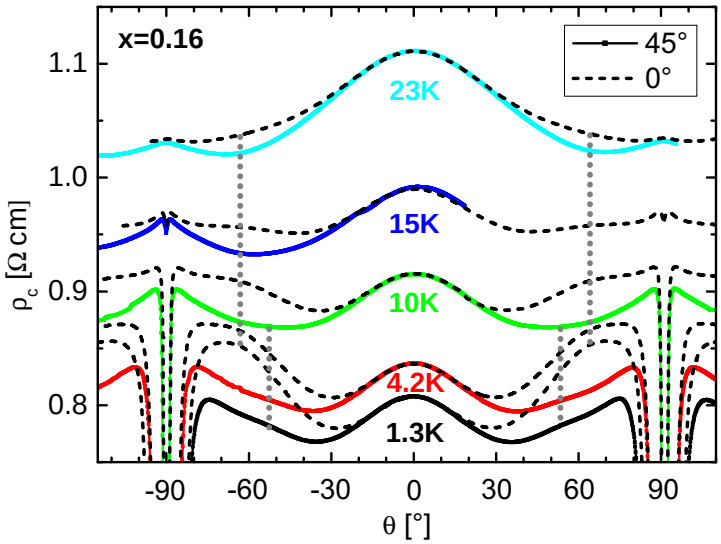

Figure 5.11: $x = 0.16$, θ-scans for different temperatures with $B = 28$T at $\phi = 0°$ (dashed lines) and 45° (solid lines)

5.2.3 Angle-dependent magnetoresistance for optimally and underdoped samples, $x = 0.15$ and $x = 0.13$

In the third part of the experiment, one sample with 15% and another one with 13% doping level were mounted and measured. Neither of these samples shows AMRO-like features. Except that for $x = 0.15$, see Fig.5.12, at the lowest temperature and highest field a ϕ-independent hump at $\theta = 0°$, similar to that for higher doping levels, shows up. The effect of resistivity enhancement, due to changing ϕ from 45° to 0°, reaches at maximum about 1.2% (at the point right before the superconductivity onset) and is five times smaller compared to $x = 0.16$.

Furthermore, as shown in Fig.5.13, by lowering the magnetic field to 23T, the wings with

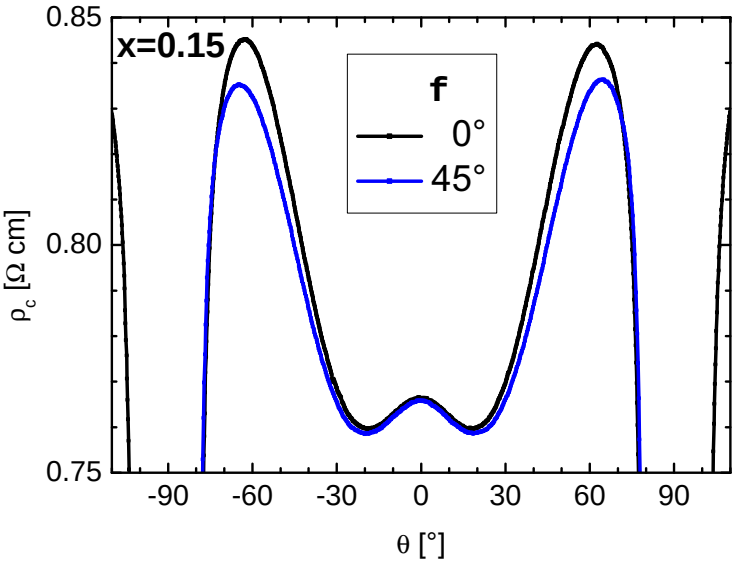

Figure 5.12: x=0.15, θ-scans for two different ϕ settings at $T = 1.3$K and $B = 28$T

positive slope $\frac{d\rho_c}{d|\theta|}$ diminish and then, at lower fields, transform into a dome-like shape for $-40° \leq \theta \leq +40°$. Since highest T_c is reached for optimal doping, his change might be related to the superconductivity onset which, of course, moves towards $\theta = 0°$ by decreasing field. To check that, the field component $B_\perp$ perpendicular to the a, b-plane, which is necessary to suppress SC in 28T, is calculated to $B_\perp(B, \theta) = B \cos\theta$. Having $B_\perp(28\text{T}, 62°) \approx 14$T one can estimate the angles at which SC should set in for lower fields to the values given in Table 5.1.

If one compares these positions with Fig.5.13, it becomes clear that the above described diminishing of the wings and the change in the slope of $\rho_c(\theta)$ is due to a rapid increase of the normal-state resistivity and not to the onset of superconductivity.

The dome-like shape of the $\rho(\theta)$ dependence becomes even more pronounced for lower doping level $x = 0.13$. In Fig.5.14 one sees clearly that the influence of SC is weaker, because the critical field is much lower: for $B = 28$T and $T = 1.3$K it sets in at $\theta \geq 70°$. We, therefore, conclude that the dome-like shape of the $\rho_c(\theta)$ dependence is an intrinsic feature of the normal-state magnetoresistance.

B[T]	θ_{onset}[°]
28	62
23	52.5
20	45.5
18	38.9
15	21

Table 5.1: $x = 0.15$, Estimated angles at which SC should set in for smaller fields, based on the onset positions measured in the θ-scan at 28T

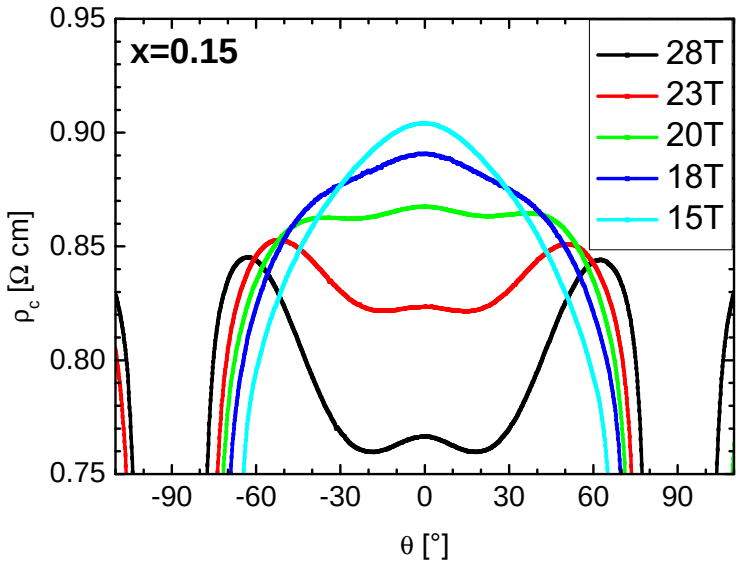

Figure 5.13: $x = 0.15$, θ-scans in different magnetic fields for ϕ set to 0° and 45° at $T = 1.25$K

There is a new effect showing up, which should be mentioned here. A hysteresis-like behavior shows up in θ-scans for the $x = 0.13$ sample at $\phi = 45°$. The resistivity for sweeping up, that is turning from $\theta = -90°$ to 0°, is about 0.7% shifted, compared to the down sweep, until it rapidly changes at $-15° \leq \theta \leq +15°$ around the $\mathbf{B} \parallel c$-axis position, and both, up and down sweep, coincide. This behaviour is likely related to spin ordering effects like those observed recently in magnetotransport of electron-underdoped cuprates [63–65]. This is, however, a topic for separate studies and will not be discussed in the present thesis.

5.2.4 Traces of Shubnikov-de Haas oscillations in fields up to 28T

Incidentally, field sweeps up to the 28T were done at different θ positions and analyzed if one can find any traces of oscillations. For the samples with $x = 0.16$ only few data of sweeps with the field direction oriented parallel to the c-axis were available. But, as one can see in Fig.5.15, both simultaneously measured samples at 1.3K showed similar oscillations within the field range of $21 - 28$T, where the peak-to-peak amplitude is about 0.05% of the background. The three observed maximums, obtained after subtracting the

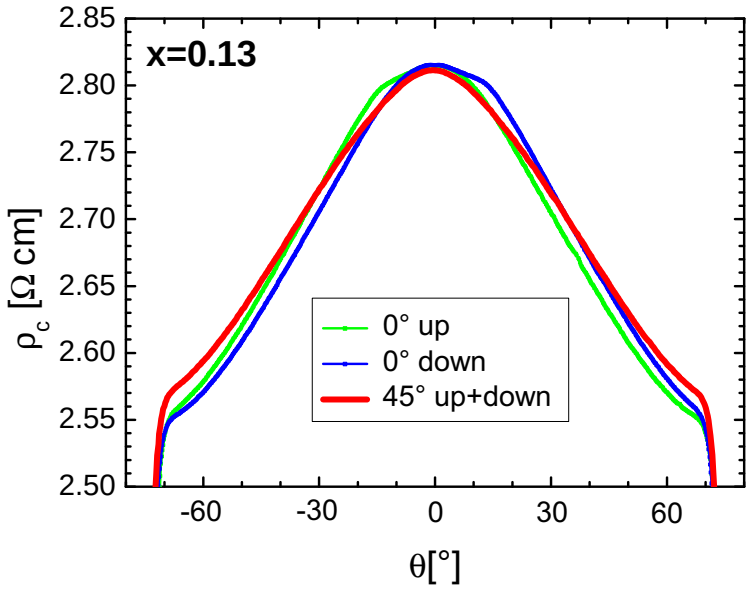

Figure 5.14: $x = 0.13$, θ-scans for different ϕ settings at $T = 1.25$K and $B = 28$T

slowly varying background resistivity from the $\rho(B)$ curves, are located at $21.8, 23.5$ and 25.5T. This would correspond to a SdH oscillation frequency of $F = 300$T.

Finally for this section, Fig.5.16 shows oscillations, obtained from one field sweep $23 - 28$T for the sample with 15% doping level at $T = 1.3$K and field parallel to the c-axis. After subtracting the resistivity background, we also observed two maximums, appearing at 24 and 26.3T, which yield a frequency of 275T

At that time we could not state whether these are real quantum oscillations, since the amplitude is close to the noise level and only one field sweep, useful for evaluation, was made for the $x = 0.15$ sample and the experiment was rather more focused on examining the discovered AMRO features than on searching for quantum oscillations. However, the data presented in Fig.5.15 and 5.16 encouraged our endeavor to search for magnetic quantum oscillations in higher magnetic fields, where one expects the amplitude of real oscillations to increase.

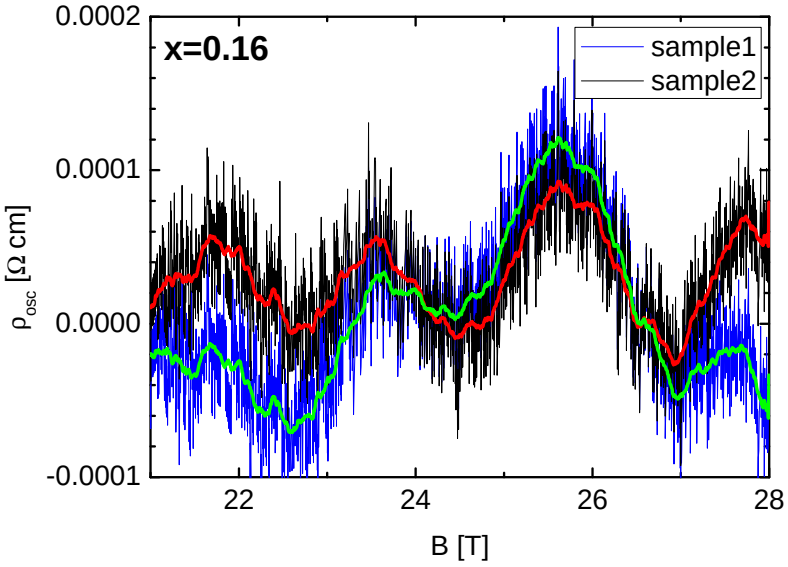

Figure 5.15: x= 0.16, Background subtracted resistivity vs. magnetic field applied perpendicular to the a, b-plane at $T = 1.3$K; green and red curves are obtained by smoothing the data from sample 1 and sample 2, respectively

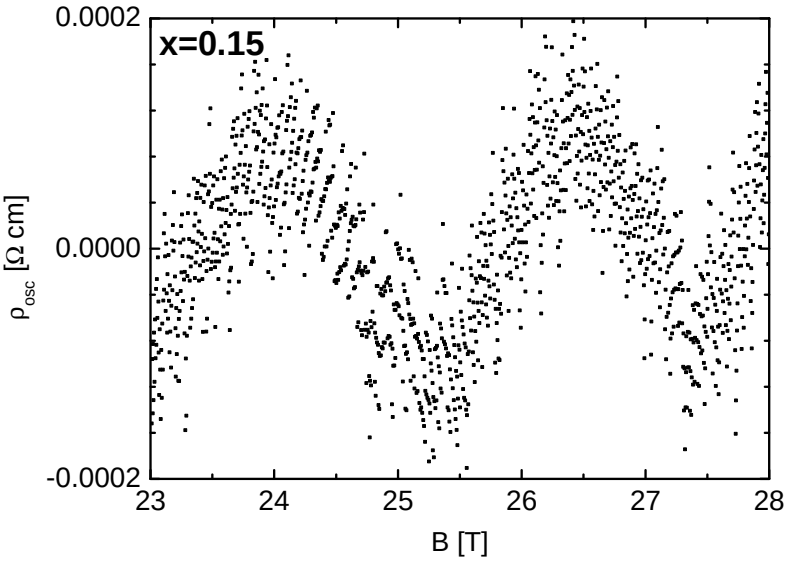

Figure 5.16: x= 0.15, Background subtracted resistivity vs. magnetic field perpendicular to the a, b-plane at $T = 1.3$K

5.3 Pulsed magnetic fields up to 65T

The observation of the angle-dependent magnetoresistance oscillations in steady fields up to $B = 28$T, as presented in the section above, demonstrates that the field strength parameter $\omega_c\tau$ is sufficiently high to reveal properties of the Fermi surface through magnetotransport in experimentally accessible magnetic fields. It is, therefore, tempting to search for Shubnikov-de Haas (SdH) oscillations in the field-dependent magnetoresistance. Indeed, a very weak slow oscillation was observed in the magnetoresitance in fields above 22T for $x = 0.15$ and $x = 0.16$, as it is shown in Fig.5.15 and 5.16. In order to verify whether this oscillations are due to the SdH effect or just noise and to search for this effect in samples with other doping levels, a series of measurements was performed in pulsed magnetic fields up to 65T in the Dresden High Magnetic Field Laboratory (DHFL).

Taking into account the high layer-type electronic anisotropy of our system, the field direction perpendicular to the layers was chosen for the experiments, as the most favorable direction for observation of magnetic quantum oscillations.

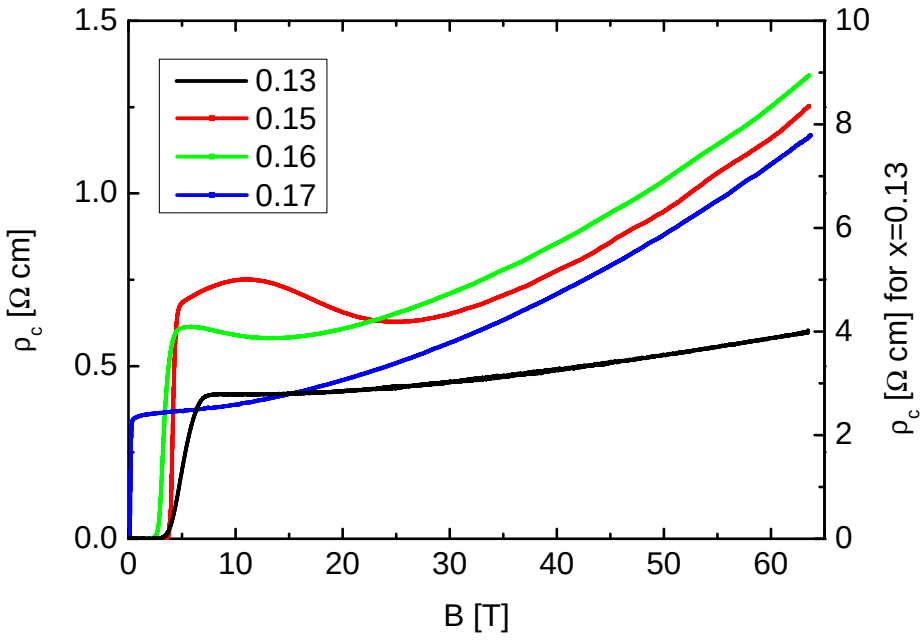

Figure 5.17: Resistivity versus magnetic field, applied perpendicular to the conducting layers for four different doping levels: $x = 0.13, 0.15, 0.16, 0.17$ at $T \approx 3$K; NOTE: For $x = 0.15$ (red curve) slow oscillations are visible by eye.

Fig.5.17 shows the resistivity as a function of magnetic field **B** for four different doping levels. All measured samples were set with the a, b-plane perpendicular to the magnetic field.
The sample with 13% doping level shows a broader transition than the others, which is consistent with our data presented in Section 5.1. For this sample we measured three further pulses: two of them up to 63.5T and one with 60T at maximum, each at lowest possible temperature. No oscillatory features have been observed.

5.3.1 Fast SdH oscillations for $x = 0.17$

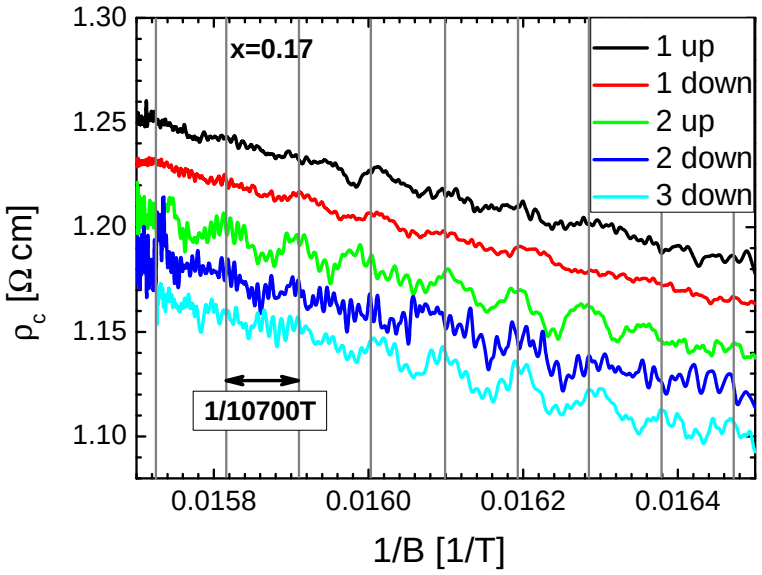

Figure 5.18: $x = 0.17$, Resistivity versus inverse magnetic field for three different pulses at $T = 3$K in the range of $60.5 - 64.5$T, the curves are shifted vertically with an offset of $n \cdot 0.1\Omega$cm, $n = 0, 1, 2, 3, 4$ for clarity, $n = 0$ for pulse 3

In Fig.5.19 the high field part of the magnetoresistance recorded during three pulses is plotted in the inverse field scale. Labels "up" and "down" mark the fast increasing and the slower decreasing side of the pulse, respectively (see pulse profile in Fig.4.4b). All the curves exhibit oscillatory behavior periodic in $1/B$. Their periodicity is visualized by a grid with interval steps of 10700T. This is verified through a Fast Fourier Transformation in Fig.5.20. The peak-to-peak amplitude

$$A = 2 \cdot \frac{\rho_c - \rho_{bg}}{\rho_{bg}},$$

where ρ_{bg} denotes the nonoscillating background resistivity, is for each pulse slightly different. In pulses 2 and 3 it becomes most pronounced and reaches at maximum about 2% of the background. Here, the problems of temperature control and mechanical noise during the pulse, mentioned in the experimental section, made it impossible to extract quantitative information about the temperature- and field-dependent damping. This needs to be studied in more detail on samples with the same doping level, with possibly smaller contact resistances and under improved temperature conditions. Nevertheless, what we can definitely state at present is that there are high frequency quantum oscillations, due to the fact that they are periodic in $1/B$, become suppressed at higher temperatures and reproduce in several pulses at lowest T.

From Eq.(2.25) we know that the SdH frequency is directly related to the area of the extremal cross-section of the FS perpendicular to the applied magnetic field. With the observed frequency $F_{0.17} = (10700 \pm 400)$T, for $x = 0.17$, and Eq.(2.25) an area of

$$S_{extr}^{0.17} = (102 \pm 4)\text{nm}^{-2}$$

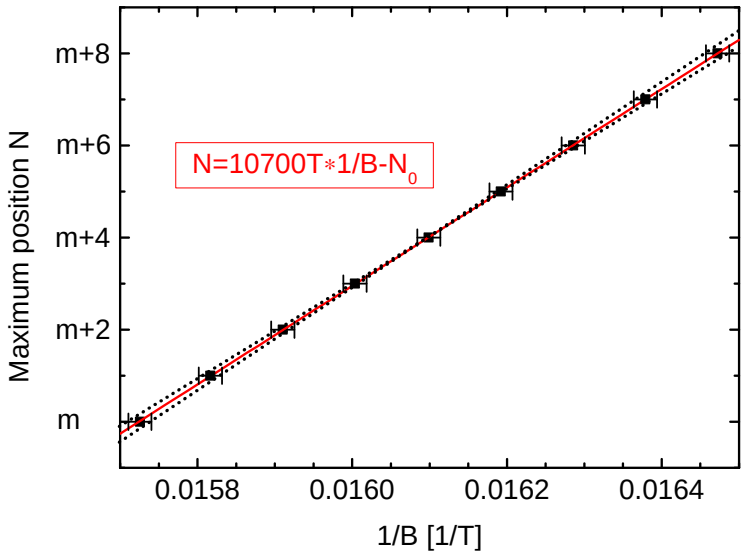

Figure 5.19: $x = 0.17$, Positions of the oscillation maximums versus reciprocal field

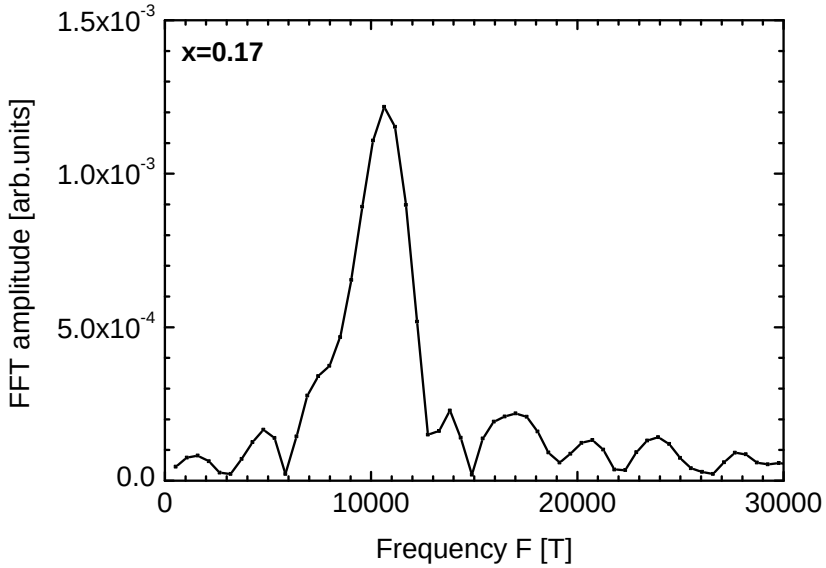

Figure 5.20: x= 0.17, Fast Fourier Transformation of the field-dependent resistivity at 3K within a field window of 60 − 63.5T

is calculated. This corresponds to $(40.5 \pm 1.5)\%$ of the Brillouin zone, taking $a = 3.95$Å as the lattice parameter from X-ray diffractometer measurements [6]. There is, to our knowledge, no reported temperature dependent change of the lattice parameters and, comparing our measured a and c parameters with literature, [66–68] they all state similar values within less than 1% deviation. Therefore, this error is negligible for calculations of the orbit area.

5.3.2 Slow SdH oscillations for $x = 0.16$

At lower doping levels no fast oscillations have been observed. But already by looking at the original $\rho(B)$ curves in Fig.5.17, a very low frequency oscillation can be resolved for $x = 0.15$ and, although less pronounced, for $x = 0.16$ too.

For further analysis, the underlying nonoscillating resistivity background was fitted by

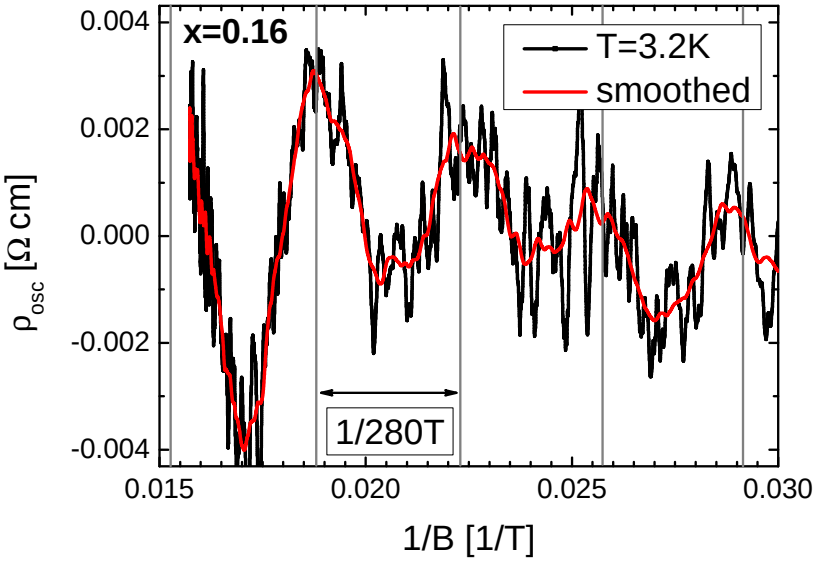

Figure 5.21: $x = 0.16$, Background subtracted resistivity versus inverse magnetic field for a pulse with $B_{max} = 63.6$T at $T = 3.2$K

a polynom and subtracted from the original curves. Fig.5.21 exhibits the background-subtracted low frequency oscillations, observed in the sample with 16% doping level at 3.2K plotted versus the inverse field. They are definitely periodic in $1/B$ and the peak-to-peak amplitude A is about 1% at maximum with respect to the nonoscillating background resistivity.

Several pulses have been done for this sample at different temperatures, which show all these oscillations with the same period and confirm the result. Like in the case with the $x = 0.17$ sample, temperature control and the signal-to-noise ratio were not good enough to extract clear data about the temperature- or field-dependence of the oscillation amplitude. However, the most important quantity, the oscillation frequency, could be reliably determined as (280 ± 25)T from plotting the maximum positions versus the inverse field, shown in Fig.5.22 and confirmed by the Fast Fourier transformation, given in Fig.5.23.

As it is explained in Section 2.4.1, the SdH effect is suppressed at increasing temperature. To check that, one pulse was done at $T = 20$K and, as one can see in Fig.5.24, there are no oscillations discernible that show the characteristic frequency of 280T.

From the observed frequency one can again calculate the area of the extremal FS cross-section perpendicular to the magnetic field direction. Hence, with $F_{0.16} = (280 \pm 25)$T an area of

$$S_{extr}^{0.16} = 2.67 \pm 0.3\text{nm}^{-2} \tag{5.1}$$

is obtained, corresponding to $(1.06 \pm 0.1)\%$ of the first Brillouin zone.

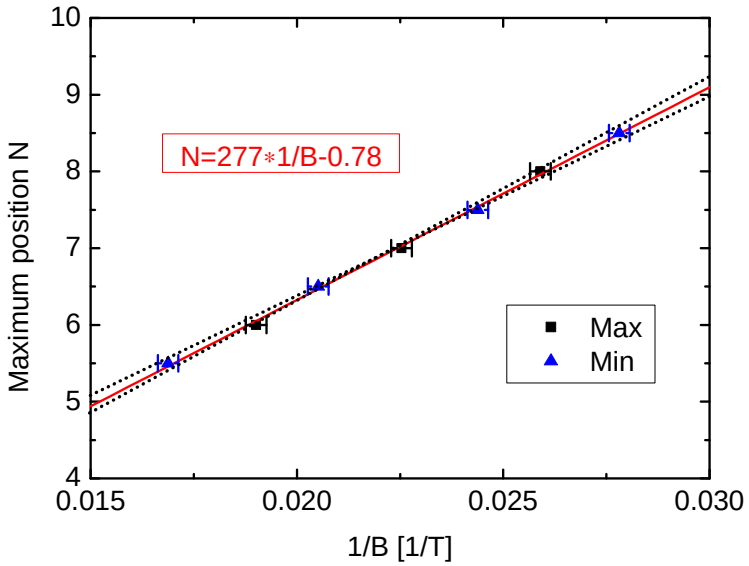

Figure 5.22: $x = 0.16$, *Positions of the minimums (blue triangles) and maximums (black squares) plotted versus* $1/B$*; The slope of the fit gives a SdH frequency of* $F = (280 \pm 25)\mathrm{T}$

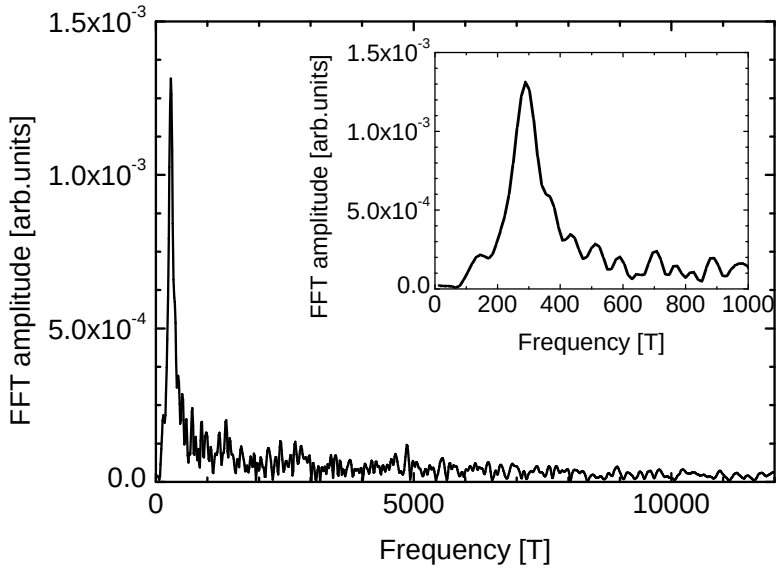

Figure 5.23: $x = 0.16$, *Fast Fourier Transformation within a field window* $26 - 63.6\mathrm{T}$ *for the slow oscillation at* $T = 3.2\mathrm{K}$ *in Fig.5.21*

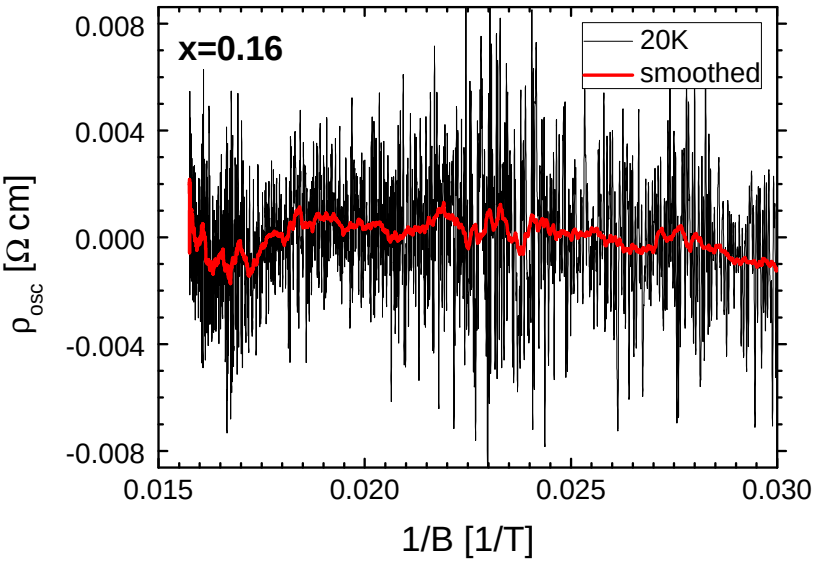

Figure 5.24: $x = 0.16$, Background subtracted resistivity plotted versus the $1/B$ for a pulse with $B_{max} = 63.5$T at $T = 20$K, Note: There are no oscillations with $F = 280$T discernible

5.3.3 Slow SdH oscillations for $x = 0.15$

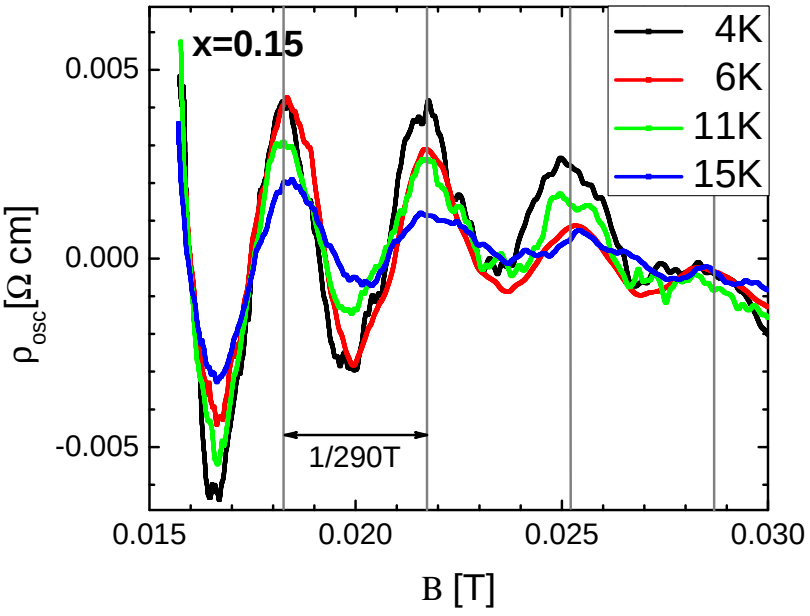

Figure 5.25: $x = 0.15$, Background subtracted resistivity versus inverse magnetic field for four different temperatures

The most detailed studies were done for a sample with 15% doping. Due to the experience, gained during the previous pulses, and very low-ohmic contacts for this sample, at

the very end of the experiment we achieved more reliable temperature conditions and a better signal-to-noise ratio. For the following analysis only pulses are chosen, where the temperatures (evaluated from comparison of the transition for each pulse to the preliminary data, as explained in Section 5.1) in up and down sweeps, deviate from each other within 1K. Therefore, the analysis of the temperature and field dependence of the oscillation amplitude becomes possible. Fig.5.25 shows the measured oscillations in the inverse field scale for four different temperatures, after the background resistivity was subtracted. They are periodic with the frequency of (290 ± 25)T and show a maximum peak-to-peak amplitude of $\simeq 2\%$ of the background. Compared to the $x = 0.16$ sample, here the amplitude is two times higher. So for x= 0.15 we observe a slightly higher slow frequency

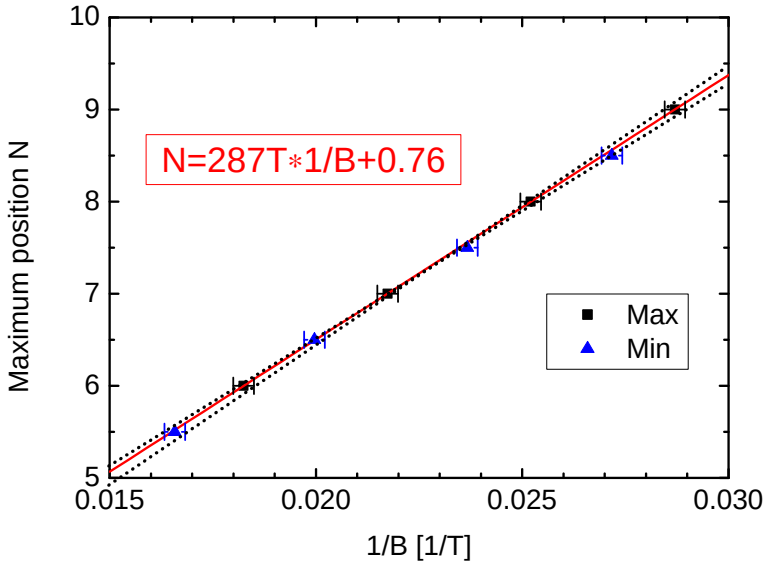

Figure 5.26: $x = 0.15$, Positions of the minimums (blue triangles) and maximums (black squares) plotted versus $1/B$; The slope of the fit gives a SdH frequency of $F = (290 \pm 25)$T

$F_{0.15} = (290 \pm 25)$T, compared to $x = 0.16$, which corresponds to a slightly larger FS cross-section area of

$$S_{extr}^{0.15} = (2.77 \pm 0.3)\text{nm}^{-2} \tag{5.2}$$

Hence, compared to the in-plane Brillouin zone area, this FS covers $(1.09 \pm 0.1)\%$, taking a= 3.95Å as the lattice parameter.

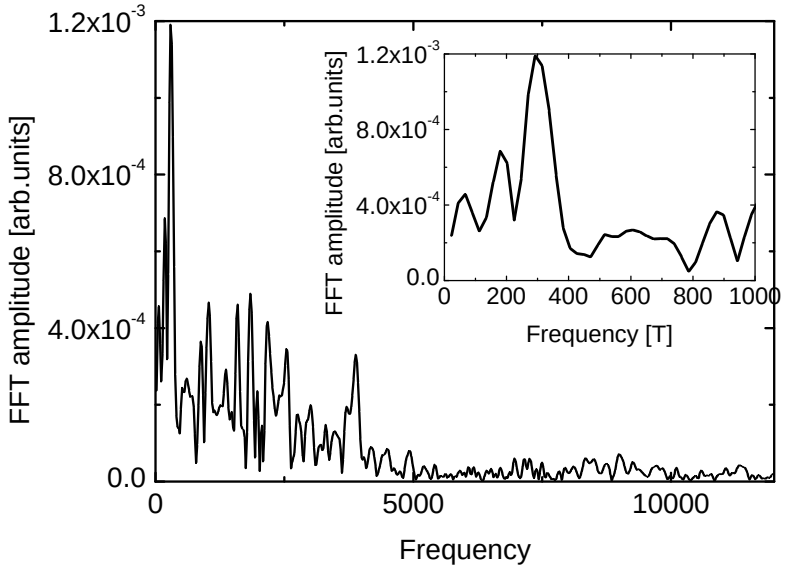

Figure 5.27: $x = 0.15$, Fast Fourier Transformation within field window $30 - 63.6$T for the slow oscillation at 4K in Fig.5.25

5.3.4 Effective cyclotron mass evaluated from the T-dependence of the oscillation amplitude for $x = 0.15$

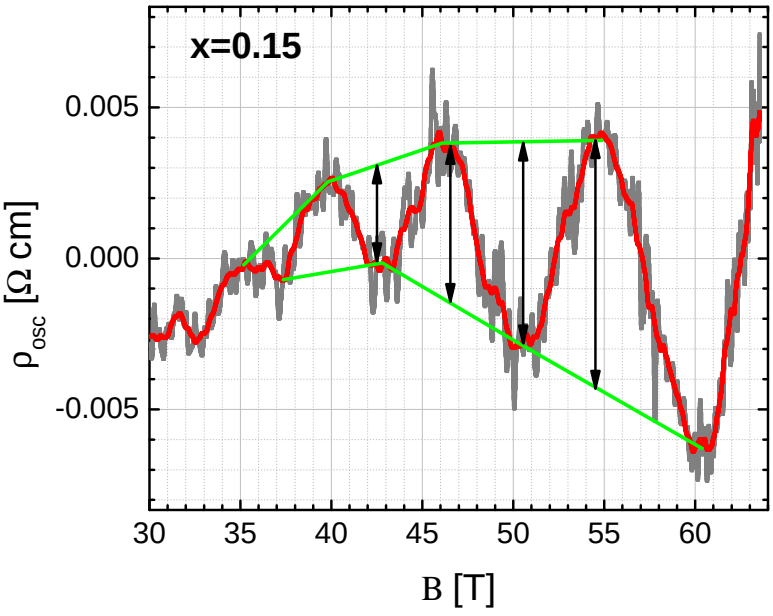

Figure 5.28: The $T = 4$K oscillation from Fig.5.25 (grey) is smoothed by averaging over 800 points (red) to determine the peak to peak amplitude at different field values (arrows)

Because of the, within 1K, stable temperatures during the four pulses shown in Fig.5.25, it is reasonable to fit their temperature-dependence, using Eq.(2.35). Here the peak-to-peak amplitudes at different fields were taken by hand. Fig.5.28 illustrates the procedure:
The background subtracted resistivity is plotted versus magnetic field, see the grey curve in Fig.5.28, and smoothed by averaging over 800 points. Than hand-drawn curves (green), connecting, respectively, subsequent maximums and minimums, are used to determine the peak-to-peak amplitude at different fields. These data are listed in Table 5.2. By

B [T] / T [K]	54.5	50.5	46	42.5
4	0.00825	0.0066	0.0051	0.0032
6	0.0075	0.0062	0.0045	0.0025
11	0.006	0.0041	0.0033	0.0022
15	0.0037	0.0024	0.00145	0.0009

Table 5.2: Peak-to-peak amplitude A at different fields and temperatures, extracted from the plots in Fig.5.25

fitting Eq.(2.35) to these, see Fig.5.29, one obtains a relative effective cyclotron mass (see Eq.(2.36)), of $\mu = 0.6 \pm 0.03$.

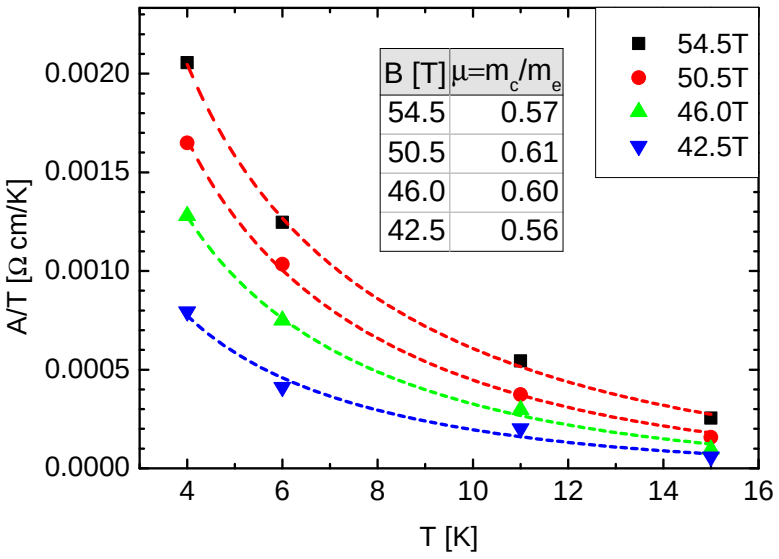

Figure 5.29: $x = 0.15$, Effective mass plot for the in Table 5.1 given data, using Eq.(2.35) for fitting

5.3.5 Dingle temperature evaluated from the field dependence of the oscillation amplitude for $x = 0.15$

The next step, after having determined the effective cyclotron mass μ, is to examine the scattering-induced damping effect from the field-dependence of the oscillation amplitude, see Section 2.4.2, regarding μ as given. In Fig.5.30 the quantity $\ln(AB^{1/2}/R_T)$ is plotted versus $1/B$. Here A is the oscillation peak-to-peak amplitude given in Table 5.1. The resulting slope α of the linear fit gives the Dingle temperature $T_D = -\alpha/K\mu$ with $K = 14.69\text{T/K}$, see Eq.(2.37). For such a plot one expects the data to be aligned along one

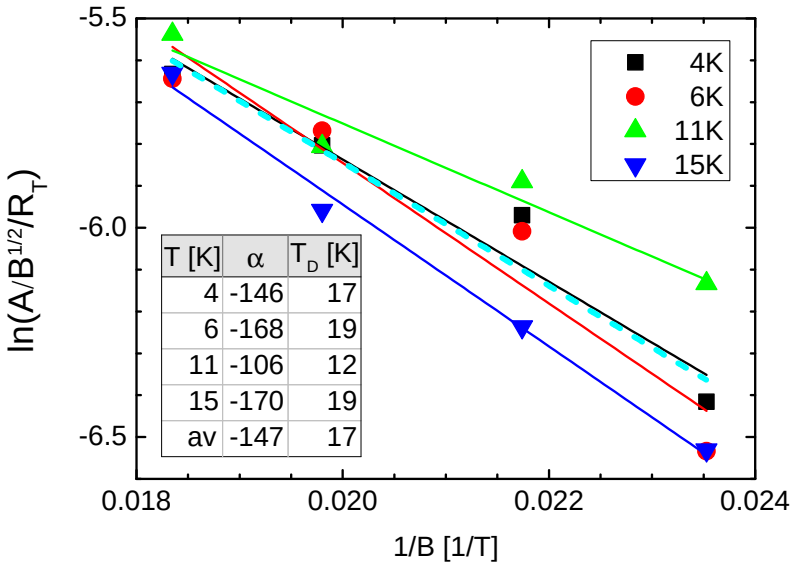

Figure 5.30: $x = 0.15$, Dingle plot

straight line. Unfortunately, in our case the scattering of the data points is very strong. It is strongest for small field values and high temperatures, but the main trend is recognizable. We, therefore, present here a preliminary evaluation of the Dingle temperature, which should be revisited after further experiments with more stable temperature conditions. In Fig.5.30, separate fits to the data for each temperature are shown in different colors and the cyan dashed line corresponds to the average fit over all points concatenated. From this we conclude that the Dingle temperature can be set to (17 ± 2)K and by using Eq.(2.38) the scattering rate τ is calculated to:

$$\tau = \frac{\hbar}{2\pi k_B T_D} = 7.2 \cdot 10^{-14}\text{s} \tag{5.3}$$

For a rough estimation of the mean free path l one can use the averaged Fermi wave vector $k_F^{\text{av}} = (S_{extr}^{0.15}/\pi)^{1/2} = 0.94\text{nm}^{-1}$ from the calculated small cross-section area, see Eq.(5.3). This corresponds to $l = \tau v_F \simeq \tau\hbar k_F^{\text{av}}/m_c$

$$l(x = 0.15) \approx 13\text{nm}$$

with an effective cyclotron mass $\mu = 0.6$.
Fig.5.31 shows simulated Shubnikov-de Haas oscillations at 4K. Here the results for μ and T_D, which we obtained from the preceding analysis, are put into Eq.(2.40). It confirms that

our evaluations of the effective cyclotron mass and Dingle temperature are very reasonable.

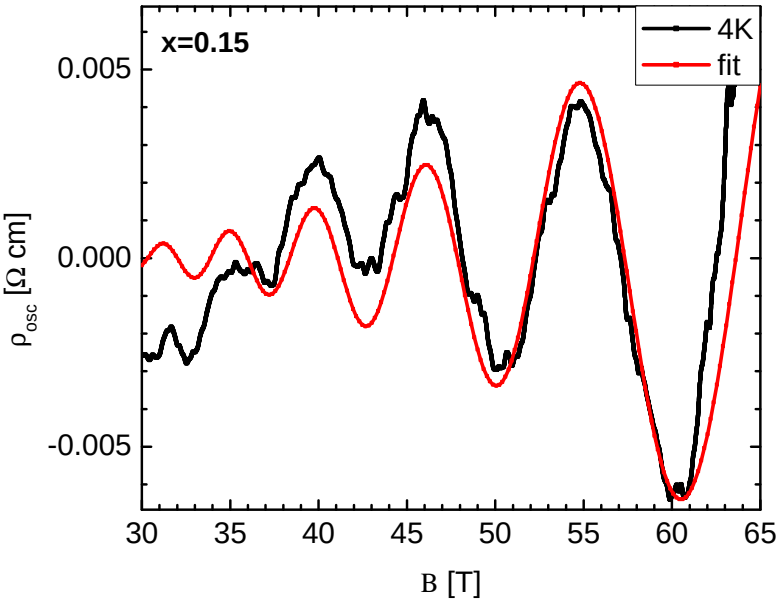

Figure 5.31: $x = 0.15$, Simulation of SdH-oscillations at 4K by using μ and T_D from the analysis above and Eq.(2.40)

6 Discussion

6.1 Angle-dependent magnetoresistance oscillations (AMRO)

Starting from the point, that we state that the observed features in the angle-dependent magnetoresistance are related to the AMRO phenomenon, there are two possible scenarios for the interpretation of our data. On the one hand, one can analyze the data by using the standard analytical AMRO theory with Yamaji's condition, see Section 2.6. On the other hand, there is the interpretation for observed similar AMRO in hole-overdoped Tl2201 compounds by Hussey et. al [7]. They performed numerical simulations of the interlayer magnetoresistance at moderately high magnetic fields ($\omega_c\tau \lesssim 1$) and associated their AMRO with a large Fermi surface (FS) with a weak warping along the k_c-axis having a certain higher-order symmetry.

In the following both approaches will be discussed and compared.

From the AMRO theory, e.g. in organic SC [34], it is known that the evolution of the AMRO polar angle positions θ with respect to different azimuthal angles ϕ directly gives information about the size and shape of the probed FS cross-section. By considering Eq.(2.44), the plot $\tan\theta$ versus ϕ should give the circumference of an envelope function, which is, therefore, directly related to the shape of the FS cross-section.

In Fig.6.1, the tangent of the obtained positions is plotted in polar coordinates and fitted to the envelope function resulting from an elliptical orbit [34] corresponding to:

$$k_{\parallel}^{max} = [k_a^2 \cos^2\phi + k_b^2 \sin^2\phi]^{1/2}, \tag{6.1}$$

where $k_{\parallel}^{max}$ is the maximum projection of the in-plane Fermi wave vector component on the direction of the field and k_a, k_b are the characteristic ellipse axes.

The elliptical fit gives a minimum at $\phi = 45°$, which would correspond to the long axis of $k_a = 3.1\text{nm}^{-1}$. Here we assume the AMRO feature to be the first maximum and $n = 1$. Due to the fact that the hump at $\theta = 0°$ does not vanish for higher temperatures, see Section 5.2.1, we cannot relate it to the usual AMRO effect. For the short axis of the ellipse the fit gives $k_b = 1.3\text{nm}^{-1}$. This would yield an elliptical orbit enclosing an area of 4.8% of the Brillouin zone area $A_{BZ} = 4\pi^2/a^2$. From this result at this point one would not state to have a large FS cross-section area and rather assume the scenario of a small FS pocket, which contributes to the normal state conductivity.

Hussey et. al [7] claim that their AMRO data, similar to ours, only can arise from a large coherent quasi-two-dimensional FS with a significant in-plane anisotropy of warping. To express the ϕ-dependent evolution in z-direction (perpendicular to the layers) of their suggested FS they used the relation given in [69] for a body-centered-tetragonal crystal structure as it is present in Tl2201 and, by the way, also in our $Nd_{2-x}Ce_xCuO_4$

$$k_F(\phi,\kappa) = \sum_{\substack{m,n=0 \\ n\ even}} k_{mn} \cos n\kappa \begin{cases} \cos m\phi\,(m \mod 4 = 0) \\ \sin m\phi\,(m \mod 4 = 2)\,, \end{cases} \tag{6.2}$$

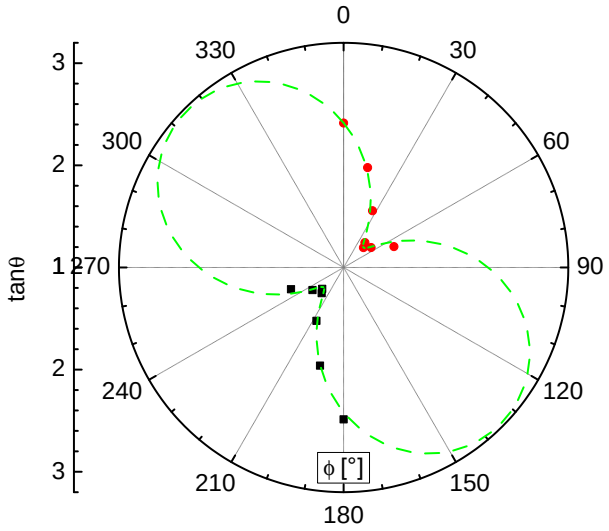

Figure 6.1: $x = 0.17$, Polar plot for AMRO positions $\tan\theta$ versus ϕ, the fit (dashed line) corresponds to an ellipse-shaped FS with its short axis k_a at 45°

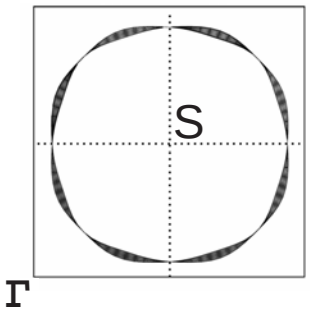

Figure 6.2: The suggested coherent FS centered around $S = (\frac{\pi}{a}, \frac{\pi}{a})$ for hole-overdoped Tl2201 by Hussey et al. [7] with a higher order in-plane symmetry for the warping in k_z-direction

where $\kappa = k_z d$ and d is the interlayer spacing (in our case $d = c/2 = 6.04$Å). Here n gives the periodicity of the warping perpendicular to the layers and m the one within the planes, depending on the azimuthal angle ϕ.

Finally Hussey et al. succeeded in simulating their data by expanding k_F, taking into account the body-centered tetragonal symmetries for k_F and hopping between adjacent layers. It resulted in a large cylindrical FS, centered at the corner of the Brillouin zone $S(\frac{\pi}{a}, \frac{\pi}{a})$, with nodes in its warping in z-direction for certain ϕs, as illustrated in Fig.6.2. From their fits they extracted a rather small $\omega\tau = 0.45$, as compared to the analytical AMRO theory where the strong-field limit, $\omega_c\tau >> 1$, is assumed. Our AMRO data is qualitatively similar to that for hole-doped Tl2201 and, therefore, it might be possible to fit it in a similar way, considering a large, hole-like FS. This analysis is currently in progress and, therefore, not included in this thesis.

At the present stage, we can compare qualitatively our data for $Nd_{2-x}Ce_xCuO_4$ to that measured in hole-overdoped Tl2201 and point out some apparent differences.

In our case we see two features: a ϕ-independent hump at $\theta = 0°$ and a ϕ-dependent feature evolving between $50° \leq \theta \leq 72°$. They are mostly pronounced at the lowest

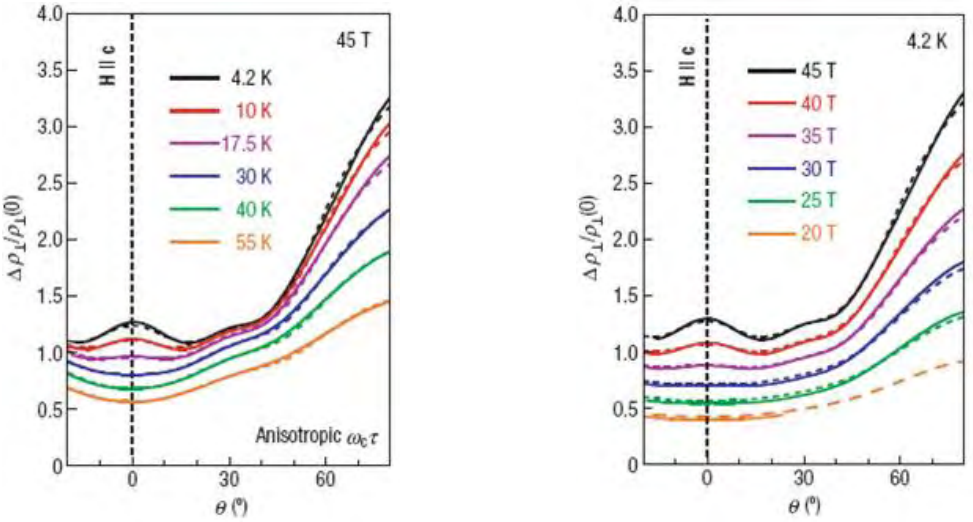

Figure 6.3: Variation of AMRO in Tl2201 with temperature (left) and field strength (right), see Hussey et. al. [7]

temperature $T = 1.4$K and maximum magnetic field 28T. The hump at $\theta = 0°$ is enhanced at increasing the field but it does not vanish for higher temperatures, as already mentioned above. In the case of Tl2201, Hussey et al. observed similar features behaving equally with respect to variation of T and B, except that the hump at $\theta = 0°$ vanished at slightly higher temperatures and fields, as compared to the ϕ-dependent feature, see Fig.6.3. At fields below 30T, the AMRO features are hardly discernible in Tl2201 (see Fig.6.3), whereas in our crystals they were clearly observed at fields of $23 - 28$T. This implies that our samples are as good or even of better crystal quality than the Tl2201 crystals used in Hussey's experiment. The evolution of the ϕ-dependent feature in Tl2201 - where θ is minimal for $\phi = 45°$ and maximal for $\phi = 0°$ - is the same for our AMRO. But the positions with $25° \leq \theta \leq 45°$ are situated nearer to the hump at $\theta = 0°$ compared to ours. In the usual picture for AMRO (simply using Yamaji's conditions) the data on Tl2201 would also fit to an elliptical FS cross-section with an area of about 47% of the Brillouin zone (taking $a = 3.6$Å, $c/2 = 1.16$nm for this system, and $n = 1$). This would mean that the usual AMRO considerations already result in a large orbit but not as big as 2/3 of the Brillouin zone, which would follow from the assumed hole-doping level of $x \approx 0.24$.

6.2 Shubnikov-de Haas oscillations

Since the upper critical fields of the hole-doped cuprates are of the order of 50-100 T, even for the underdoped compounds, such as $YBa_2Cu_3O_{6.5}$ and $YBa_2Cu_4O_8$, the observations of quantum oscillations in these compounds [12, 14] have been largely restricted to the superconducting (mixed state) part of the phase diagram so far. This raises a question: are the oscillations really due to the SdH effect? In particular, an alternative mechanism associated with quantum interference in the system of Abrikosov vortices have been proposed recently [70]. By contrast, the $Nd_{2-x}Ce_xCuO_4$ system has an order of magnitude lower $B_{c2,\perp}$, as mentioned in Section 3.3. Therefore, the oscillations observed in fields 30 to 60 T are definitely related to the normal-state SdH effect. Hence, the oscillatory magnetoresistance behavior presented in Section 5.2 is an unambiguous evidence of a well defined Fermi surface in the bulk of the electron-doped superconducting cuprates in the range from optimal doping up to the highest achieved overdoping.

As a matter of fact, the present oscillations are one of the first observations of Shubnikov-de Haas effect in a nonstoichiometric cuprate compound. By the beginning of this thesis no quantum oscillations in a nonstoichiometric hole-overdoped cuprate had been reported. Just right at the time of our pulsed-field experiment the first report [16] on the observation of quantum oscillations with a frequency $F = 18$ kT in a hole-overdoped Tl2201 was published. Those authors measured several high quality samples and only few of them showed the oscillations. Thus, the fact that we were able to detect quantum oscillations in a series of samples with different doping levels, in particular, those with a high frequency, for $x = 0.17$, clearly proves the very high quality of the electron-doped cuprate single crystals grown in our institute. In particular, the oscillation frequency for $x = 0.17$ corresponds to a large FS and, consequently, to a very large Larmor radius, $r_L = \hbar k_F/eB \approx 60$ nm at $B = 60$ T. This suggests a very large mean free path, $\ell \sim r_L$, indicating a high crystal quality.

The high frequency SdH oscillations - with $F = (10700 \pm 400)$T - for samples with 17% electron doping reveals a large orbit, occupying (40.5 ± 1.5)% of the first Brillouin zone (BZ). This is consistent with the sample's stoichiometry, which, according to the Luttinger rule, implies a FS covering 41.5% of the 1st BZ for this doping level.

The frequency of the oscillations found on samples with $x = 0.15$ and 0.16 is much smaller, and is associated with a small Fermi pocket occupying only 1.1% of the Brillouin zone. This dramatic transformation can be explained by assuming a superstructure, which emerges at $x < 0.17$ and doubles the unit cell in the a, b-plane. Such a superstructure is known to exist in undoped and underdoped $Nd_{2-x}Ce_xCuO_4$ due to the antiferromagnetic (AFM) ordering [52–59]. Moreover, several authors suggested that it persists up to $x = 0.17$, in order to explain the behaviour of the inplane magnetoresistance and Hall coefficient [6,23].

Fig.6.2a shows a two-dimensional view of the reconstruction of the original large FS for $x = 0.15$ due to a superstructure with the wave vectors $\mathbf{Q}^{\pm} = (\frac{\pi}{a}, \pm\frac{\pi}{a})$ [22,23]. Suggesting that the slow SdH oscillations originate from the small hole-like pockets centered at $(\pm\frac{\pi}{2a}, \pm\frac{\pi}{2a})$ their size was fitted to 1.1% of the original Brillouin zone area, using the gap Δ in Eq.(3.2) as a fitting parameter. The fitting yielded $\Delta = 64$ meV. The same procedure applied to the $x = 0.16$ gives $\Delta = 35.6$ meV.
Another possibility is to suggest a larger gap which would completely close the hole-like pockets of the FS and ascribe the oscillations to remnant small electron-like pockets, as shown in Fig.6.2b. This would imply a large superstructure gap, $\Delta = 0.64$ eV which is comparable to that evaluated for the undoped mother compound based on ARPES

data [21]. It is unlikely that the AFM ordering in the optimally doped compound is as strong as in the undoped one. Therefore, the reconstruction shown in Fig.6.2a looks more realistic. Note that this scenario, if true, implies the magnetoresistance behavior to be dominated by the minority hole-like carriers, while the electron-like pockets remain "invisible" in our experiment. The same conclusion, regarding the dominant role of the hole-like carriers, has been made from the Hall measurements [6, 23]. The gap values estimated by those authors are considerably higher than ours. We believe that our data is more realistic, since our derivation is more straightforward and involves only one fitting parameter, Δ.

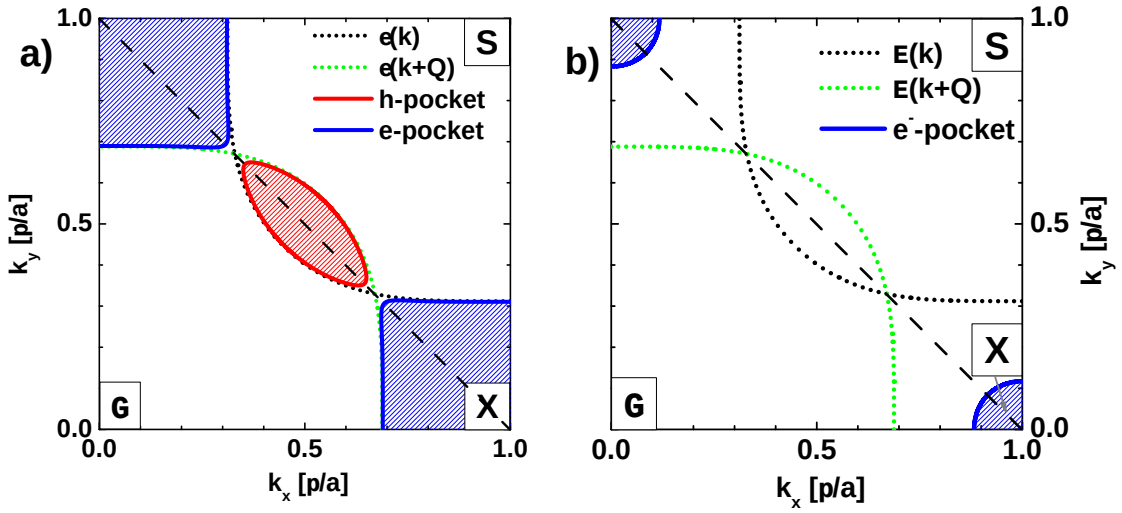

Figure 6.4: Two possibilities for a Fermi surface cross-section with $S_{extr} = 0.011 S_{firstBZ}$: a) hole-like pockets at $(\frac{\pi}{2a}, \frac{\pi}{2a})$ and b) electron-like pockets at $(\pm\frac{\pi}{a}, 0)$, $(0, \pm\frac{\pi}{a})$, respectively

Nevertheless, we note that our conclusions qualitatively confirm those based on the in-plane magnetotransport [6, 23].

Comparing our results to those, obtained on the hole-doped yttrium-barium cuprates, one can notice an interesting "antisymmetry": in these compounds the quantum oscillations and magnetotransport are also dominated by the minority carriers, but in that case they are electron-like. Another important difference with respect to the hole-doped cuprates is that the small FS is found for optimally doped and even for overdoped compositions of $Nd_{2-x}Ce_xCuO_4$. This implies that the superstructure originating, most likely, from AFM ordering persists in the overdoped side of the phase diagram. On the other hand, electron correlations in these compounds are considerably weaker than in the hole-underdoped $YBa_2Cu_3O_{6.5}$ and $YBa_2Cu_4O_8$. The effective cyclotron mass evaluated in Sect.5.3, $m_c \approx 0.6m_e$, is 3 to 5 times lower than for the latter compounds [12–14], indicating smaller effects of many-body renormalization.

The striking difference between the SdH frequencies for the compositions $x = 0.15$ and 0.16 on one hand, and for $x = 0.17$ on the other implies that the superstructure gap is either strongly suppressed or absent at $x = 0.17$.
The complete suppression of the gap and corresponding transformation of the FS would be consistent with suggestions of quantum phase transition at a doping level between 0.16 and 0.17, see, e.g., [63, 71].
However, taking into account the AMRO data in Section 5.2, it seems more likely that a small gap still exists even in the $x = 0.17$ sample. Indeed, the AMRO features are very

similar for $x = 0.17$ and 0.16, suggesting the same cyclotron orbits contributing to the magnetoresistance at both doping levels, at least, in magnetic fields below 30 T. Assuming the gap is absent at $x = 0.17$, the AMRO should be associated with large orbits on the unreconstructed FS, for both dopings. In the case of $x = 0.16$, such orbit can only emerge at a sufficiently high field as a result of magnetic breakdown. The characteristic breakdown field can be estimated roughly from Eq.(2.46), using the cyclotron mass and Fermi energy (i.e. the energy between the Fermi level and the top of the hole-like band) corresponding to the large, unreconstructed FS. Approximating the cross-section of the unreconstructed FS by a circle, assuming the Fermi velocity to be isotropic in the a, b-plane, and using semiclassical equations of motion (2.1), one can obtain the cyclotron mass on the large orbit:

$$m_{c,\text{large}} = \frac{L_{\text{large}}}{L_{\text{small}}} m_{c,\text{small}} \approx 4.0 m_e \ , \tag{6.3}$$

where $m_{c,\text{small}} \approx 0.6 m_e$ is the cyclotron mass corresponding to the small elliptic orbit determined from the SdH oscillations, see Section 5.3, and $\frac{L_{\text{large}}}{L_{\text{small}}} \approx 6.7$ is the circumference ratio between the large and small orbits depicted in Fig.6.4a (dashed black and solid red lines, respectively). Incidentally, this value is comfortably similar to $m_c = 4.1 m_e$ directly evaluated for the hole-overdoped cuprate Tl2201 from the fast SdH oscillations [13]. The Fermi energy can be estimated as:

$$\epsilon_F = \frac{\hbar^2 k_F^2}{2 m_{c,\text{large}}} \simeq \frac{\hbar^2 S_{extr}^{0.17}}{2\pi m_{c,\text{large}}} = 0.32\text{eV}, \tag{6.4}$$

where the cross-sectional area of the unreconstructed FS, $S_{extr}^{0.17} = 105$ nm^{-2}, is taken from the frequency of the fast SdH oscillations (see Section 5.3). Now, substituting the cyclotron mass, the Fermi energy, and the superstructure gap, $\Delta = 35.6$ meV obtained above for $x = 0.16$ into Eq.(2.46) one estimates the magnetic breakdown field as: $B_{\text{MB}} \simeq 540$ T. This value is much too high for the large orbit to be realized at fields 25-28 T, at which the AMRO is observed in the $x = 0.16$ sample. Thus, one can conclude that the AMRO is unlikely to be associated with the large FS orbit.

An alternative scenario, associating the AMRO with a small elliptic FS, was proposed in Section 6.1. It would be natural to suggest the small FS being the common origin for the AMRO and slow SdH oscillations observed on the $x = 0.16$ sample. However, the cross-sectional area of the FS obtained from the AMRO, 4.8% of the Brillouin zone, is 4 times larger than the area corresponding to the slow SdH oscillations. To resolve this discrepancy, we suggest to take into account the three-dimensional character of AFM ordering in the $Nd_{2-x}Ce_xCuO_4$ system. As established for underdoped compounds, there is a correlation between spins ordered in adjacent CuO_2 planes [59, 64], which makes the nearest neighboring Cu-sites in adjacent layers non-equivalent. One could, then, expect a superstructure potential to exist not only in the a, b-plane but also along c. This would lead to an effective doubling of the unit cell in the c-direction and reduction of the Brillouin zone size along $\mathbf{k}_c$ from $2\pi/d = 4\pi/c$ to $2\pi/c$ (remember that $d = c/2$ is the distance between adjacent CuO_2 layers). If the same is valid for overdoped compounds, one should replace d by c in the AMRO condition, see Eqs.(2.42), (2.44). This would lead to a decrease of the Fermi wave vector derived from the AMRO by a factor of two. As a result, the area of the reconstructed FS is reduced from 4.8% to 1.2% of the original Brillouin zone area, in excellent agreement with the value obtained from the SdH oscillations.

If the above scenario is true, the AMRO observed in the $x = 0.17$ sample are also related to a small FS pocket in the reduced Brillouin zone and, thus, indicate a finite superstructure

gap. The gap should, however, be considerably smaller than for $x = 0.16$: the absence of slow and presence of the fast SdH oscillations indicates a relatively high magnetic breakdown probability at fields $\gtrsim 30$ T. Setting the breakdown field B_{MB} in the range 30-50 T, one can evaluate the relevant energy gap as: $\Delta = 8 - 11$ meV. Thus, a comparison between the AMRO and SdH data suggests that a superstructure gap of about 10 meV exists even at the highest doping level studied.

Of course, the considerations presented above concerning the origin of the AMRO are, to a high degree, speculative and need to be verified by further detailed experiments. However, regardless of this uncertainty, the observation of slow SdH oscillations in our experiments is a solid evidence for the superstructure gap persisting up to a doping level of, at least, 16%.

This result seems to contradict recent inelastic neutron scattering experiments [72], which revealed very short range AFM correlations but no long range order in optimally doped $Nd_{2-x}Ce_xCuO_4$. The observation of slow oscillations for $x = 0.15$ and 0.16 crystals implies a periodic superstructure potential existing on the range of, at least, the mean free path evaluated from the SdH oscillations, $\ell \sim 13$ nm. This is an order of magnitude larger than the spin-correlation length, evaluated from the inelastic neutron scattering on optimally doped $Nd_{2-x}Ce_xCuO_4$ [72]. On the other hand, a number of other authors have reported some indications of AFM ordering extending into the overdoped part of the phase diagram of $Nd_{2-x}Ce_xCuO_4$ and related $Pr_{2-x}Ce_xCuO_4$ compounds [63, 65, 72–74]. A similar superstructure was suggested to exist in hole-underdoped $YBa_2Cu_3O_{6.5}$ and $YBa_2Cu_4O_8$ [12–14], where a long-range AFM order was also not found so far. For those compounds an AFM order was proposed to be induced by a high magnetic field [75]. There was, however, an argument put forward against this scenario [76]. Further studies are necessary to clarify this apparent discrepancy.

7 Conclusion and outlook

Inter-layer magnetotransport studies on a set of $Nd_{2-x}Ce_xCuO_4$, [x = 0.13; 0.15; 0.16; 0.17] single crystals, covering the superconducting part of the phase diagram of electron-doped cuprates, have been performed in high magnetic fields. For the first time angle-dependent magnetoresistance oscillations and Shubnikov-de Haas oscillations were observed for electron-doped cuprates (at different dopings x). Since these effects can be related directly to the Fermi surface (FS) topology in the bulk of the crystals, our observations reveal the existence of a well defined FS in this system and provide quantitative information on the FS properties.

The main results of this work are summarized in the following:

Rotation of samples with $x = 0.17$ in a fixed magnetic field of $B = 15$T (superconducting coil at the WMI) has shown a significant effect of the magnetic field orientation on the resistivity. The overall angular dependence of the resistivity resembles that, found on the hole-overdoped Tl2201 compound.
However, the field of 15T appears to be too low to reveal unambiguously magnetoresistance features related to the FS geometry.
It was only when the same measurements were performed at fields 20-28T (Grenoble High Magnetic Field Laboratory) that AMRO could be observed, evidencing an existing FS. The usual AMRO theory applied to this data, yields a small ellipse-like FS with an area corresponding to 4.8% of the first Brillouin zone. This picture alters from the interpretation of AMRO data in Tl2201, where the effect has been attributed to a large coherent cylindrical FS with an anisotropic warping in out-of-plane direction. Additionally, AMRO, similar to those for a carrier concentration of $x = 0.17$, were observed in less overdoped samples, with $x = 0.16$. Already field sweeps to 28T in optimally and slightly overdoped samples with $x = 0.15$ and $x = 0.16$, respectively, indicated signs of SdH oscillations.
But having found two maximums of amplitude close to the noise level was not convincing enough at that time. Therefore, for samples of the same doping levels the resistivity was measured in pulsed magnetic fields up to 65T. These experiments proved the existence of a small FS pocket manifested in slow SdH oscillations of frequency $F = 290$T and 280T for the optimally doped, $x = 0.15$, and slightly overdoped, $x = 0.16$, samples, respectively. The calculated area of the relevant FS cross-section, $2.7 - 2.8\text{nm}^{-2}$, corresponds to 1.1% of the Brillouin zone. From a series of pulses at different temperatures, for the $x = 0.15$ sample, the cyclotron mass was estimated to be $0.6m_e$. By analyzing the field dependence of the oscillation amplitude, the Dingle temperature could be calculated as (17 ± 2)K, giving the scattering time $\tau \approx 7.2 \times 10^{-14}$s, which corresponds to a mean free path of $l \simeq 13$nm.
For the 17% overdoped sample no slow oscillations were seen; instead, at fields above 60T oscillations of a high frequency, $F = 10700$T, were found, revealing a large cyclotron orbit, enclosing 41% of the Brillouin zone. The size of the corresponding FS is consistent, within the experimental error of about 1%, with the carrier concentration expected for this stoichiometry.

The small FS pockets, found for $x = 0.15$ and 0.16, can be understood as a result of a superstructure with the wave vector $\mathbf{Q} = (\pm\pi/a, \pm\pi/a)$, originating, most likely, from AFM ordering. The analysis of the slow SdH oscillations in terms of the two band model yields an evaluation of the energy gap opening in the conduction band due to this superstructure: $\Delta \approx 64$ and 36meV for the optimally doped and moderately overdoped compositions, respectively.

The ordering is strongly weakened for the far overdoped composition, $x = 0.17$, which leads to the restoration of the original large FS. Nevertheless, the comparison of the SdH data with the AMRO suggests the superstructure, with a small, $\lesssim 20$meV, gap to persist even in this case.

The present work brings a new insight into the normal state properties of the electron-doped cuprate $Nd_{2-x}Ce_xCuO_4$. It is also expected to have a significant impact on the understanding of superconductivity in this type of materials, in particular, concerning the interplay of superconductivity and magnetism.

Our results demonstrate the power of out-of-plane transport studies for the purpose of explorations of FS topologies, and show the necessity of further experiments to this subject. In pulsed fields, further studies are necessary with an improved temperature control and signal-to-noise ratio to get more detailed data on the temperature, field and, probably, the orientation dependence of the SdH oscillations for overdoped compositions.

It is very tempting to perform the AMRO and SdH oscillation studies in the highest steady magnetic fields, up to 45 T, available at the National High Magnetic Field Laboratory, Tallahassee, USA. Such experiment should give a more precise information on the AMRO parameters for overdoped samples and, probably, reveal AMRO in the optimally doped and underdoped samples. Finally, it is important to explore other samples with intermediate doping levels, such as $x = 0.14$ and $x = 0.165$, as well as some other cuprate compounds which can be grown with a high crystal quality by the TSFZ technique available at the WMI.

Bibliography

[1] J. G. Berdnoz & K. A. Mueller. Possible high T_c superconductivity in the Ba-La-Cu-0 system. *Z. Phys. B* **64**, 189 (1986).

[2] M. A. Dixon. The normal state electronic structure of cuprate superconductors: a covalent picture. *Physica C* **174**, 117 (1990).

[3] P. A. Lee, N. Nagaosa & X.-G. Wen. Doping a Mott insulator: Physics of high-temperature superconductivity. *Rev. Mod. Phys.* **78**, 17 (2006).

[4] T. B. Lindemer, J. F. Hunley, J. E. Gates, A. L. Sutton, J. Brynestad, C. R. Hubbard & P. Gallagher. Experimental and Thermodynamic Study of Nonstoichiometry in [$YBa_2Cu_3O_{7-x}$]. *J. Am. Ceram. Soc.* **72**, 1775 (1989).

[5] A. Erb, J.-Y. Genoud, M. Dhalle, E. Walker & R. Flukiger. Reversible suppression of the so-called fishtail effect in ultra pure single crystals of $YBa_2Cu_3O_{7-x}$. *Physica C* **282-287**, 2145 (1997).

[6] M. Lambacher. *Crystal growth and normal state transport of electron-doped high temperature superconductors.* Ph.D. thesis, TU Muenchen (2008).

[7] N. E. Hussey, M. Abdel-Jawad, A. Carrington, A. P. Mackenzie & L. Balicas. A coherent three-dimensional Fermi surface in a high-transition-temperature superconductor. *Nature* **425**, 814–816 (2003).

[8] M. Abdel-Jawad, M. P. Kennett, L. Balicas, A. Carrington, A. P. Mackenzie, R. McKenzie & N. E. Hussey. A coherent three-dimensional Fermi surface in a high-transition-temperature superconductor. *Nature Physics* **2**, 821–825 (2006).

[9] D. J. Singh & W. Pickett. Electronic characteristics of $Tl_2Ba_2CuO_6$. *Physica C* **203**, 193–199 (1992).

[10] E. Pavarini, I. Dasgupta, T. Saha-Dasgupta, O. Jepsen & O. K. Andersen. Band-structure trend in hole-doped cuprates and correlation with T_{cmax}. *Phys. Rev. Lett.* **87**, 047003 (2001).

[11] T. Valla, A. V. Fedorov, J. Lee, J. C. Davis & G. D. Gu. The ground state of the pseudogap in cuprate superconductors. *Science* **314**, 1914 (2006).

[12] N. Doiron-Leyraud, C. Proust, D.LeBoeuf, J.Levallois, J.-B-Bonnemaison, R. Liang, D. A. Bonn, W. N. Hardy & L. Taillefer. Quantum oscillations and the Fermi surface in an underdoped high-T_c superconductor. *Nature* **447**, 565–568 (2007).

[13] A. F. Bangura, J. D. Fletcher, A. Carrington, J. Levallois, J.Levallois, M. Nardone, B. Vignolle, N. Doiron-Leyraud, D.LeBoeuf, L. Taillefer, S. Adachi, C. Proust, & N. E. Hussey. Small Fermi surface pockets in underdoped high temperature superconductors: Observation of Shubnikov-de Haas oscillations in $YBa_2Cu_4O_8$. *Phys. Rev. Lett.* **100**, 047004 (2008).

[14] C. Jaudet, D. Vignolle, J.Levallois, D.LeBoeuf, N. Doiron-Leyraud, B.Vignolle, M. Nardone, A. Zitouni, R. L. D. A. Bonn, W. N. Hardy, L. Taillefer & C. Proust. De Haas-van Alphen oscillations in the underdoped high-temperature superconductor $YBa_2Cu_3O_{6.5}$. *Phys. Rev. Lett.* **100**, 187005 (2008).

[15] S. E. Sebastian, N. Harrison, E. Palm, T. P. Murphy, C. H. Mielke, R. Liang, D. A. Bonn, W. N. Hardy & G. G. Lonzarich. A multi-component Fermi surface in the vortex state of an underdoped high-T_c superconductor. *Nature* **454**, 200–203 (2008).

[16] B. Vignolle, A. Carrington, R. A. Cooper, M. M. J. French, A. P. Mackenzie, C. Jaudet, D. Vignolles, C. Proust & N. E. Hussey. Quantum oscillations in an overdoped high-T_c superconductor. *Nature* **455**, 952–955 (2008).

[17] N. P. Armitage, D. H. Lu, C. Kim, A. Damascelli, K. M. Shen, F. Ronning, D. L. Feng, P. Bogdanov, Z.-X. Shen, P. K. Mang, N. Kaneko, M. Greven, Y. Onose, Y. Taguchi & Y. Tokura. Anomalous electronic structure and pseudogap effects in $Nd_{1.85}Ce_{0.15}CuO_4$. *Phys. Rev. Lett.* **87**, 147003 (2002).

[18] N. P. Armitage, F. Ronning, D. H. Lu, C. Kim, A. Damascelli, K. M. Shen, D. L. Feng, H. Eisaki, Z.-X. Shen, P. K. Mang, N. Kaneko, M. Greven, Y. Onose, Y. Taguchi & Y. Tokura. Doping dependence of an n-typ cuprate superconductor investigated by angle-resolved photoemission spectroscopy. *Phys. Rev. Lett.* **88**, 257001 (2002).

[19] N. P. Armitage, D. H. Lu, D. L. Feng, C. Kim, A. Damascelli, K. M. Shen, F. Ronning, Z.-X. Shen, Y. Onose, Y. Taguchi & Y. Tokura. Superconducting gap anisotropy in $Nd_{1.85}Ce_{0.15}CuO_4$: Results from photoemission. *Phys. Rev. Lett.* **86**, 1126–1129 (2001).

[20] D. M. King, Z.-X. Shen, D. S. Dessau, B. O. Wells, W. E. Spicer, A. J. Arko, D. S. Marshall, J. DiCarlo, A. G. Loeser, C. H. Park, E. R. Ratner, J. L. Peng, Z. Y. Li & R. L. Greene. Fermi suface and electronic structure of $Nd_{2-x}C2_xCuO_{4-\delta}$. *Phys. Rev. Lett.* **70**, 3159–3162 (1993).

[21] H.Matsui, T. Takahashi, T. Sato, K. Terashima, H. Ding, T. Uefuji & K. Yamada. Evolution of the pseudogap across the magnet-superconductor phase boundary of $Nd_{2-x}Ce_xCuO_4$. *Phys. Rev. B* **75**, 224514 (2007).

[22] C. Kusko, R. S. Markiewicz, M. Lindroos & A. Bansil. Fermi surface evolution and collapse of the Mott pseudogap in $Nd_{2-x}Ce_xCuO_{4-\delta}$. *Phys. Rev. B* **66**, 140513 (2002).

[23] J.Lin & A. J. Millis. Theory of low-temperature Hall effect in electron-doped cuprates. *Phys. Rev. B* **72**, 214506 (2005).

[24] A. Kanigel, M. R. Norman, M. Randeria, U. Chatterjee, S. Souma, A. Kaminski, H. M. Fretwell, S. Rosenkranz, M. Shi, T. Sato, T. Takahashi, Z. Z. Li, H. Raffy, K. Kadowaki, D. Hinks, L. Ozyuzer & J. C. Campuzano. Evolution of the pseudogap from Fermi arcs to the nodal liquid. *Nature Phys.* **2**, 447–451 (2006).

[25] M. A. Hossain, J. D. F. Motterhead, D. Fournier, A. Bostwick, J. L. McChesney, E. Rotenberg, R. Liang, W. N. Hardy, G. A. Sawatzky, I. S. Elfimov, D. A. Bonn & A. Damascelli. In situ doping control of the surface of high-temperature superconductors. *Nature Physics* **4**, 527–531 (2008).

[26] M. Tsunekawa, A. Sekiyama, S. Kasai, S. Imada, H. Fujiwara, T. Muro, Y. Onose, Y. Tokura & S. Suga. Bulk electronic structures and strong electron-phonon interactions in an electron-doped high-temperature superconductor. *New J. Phys.* **10**, 073005 (2008).

[27] A. A. Abrikosov. *Fundamentals of the theory of metals* (Physical Sciences and Engineering Devision, 1988).

[28] E. N. Adams & T. D. Holstein. -. *J. Phys. Chem. Solids* **10**, 254 (1959).

[29] A. B. Pippard. *Magnetoresistance in Metals* (Cambridge University Press, 1989).

[30] D. Shoenberg. *Magnetic oscillations in metals* (Cambridge University Press, 1984).

[31] M. V. Kartsovnik. High magnetic fields: A tool for studying electronic properties of layered organic metals. *Chem. Rev.* **104**, 5737–5781 (2004).

[32] K. Yamaji. On the angle dependence of the magnetoresistance in quasi-two-dimensional organic superconductors. *J. Phys. Soc. J.* **58**, 1520–1523 (1989).

[33] R. Yagi, Y. Iye, T. Osada & S. Kogashima. Semiclassical interpretation of angular-dependent oscillatory magnetoresistance in quasi-tow-dimensional systems. *J. Phys. Soc. J.* **59**, 3069–3072 (1990).

[34] M. V. Kartsovnik, V. N. Laukhin, S. I. Pesotskii, I. F. Shchegolev & V. M. Yakovenko. Angular magnetoresistance oscillations and the shape of the Fermi surface in β-$(ET)_2IBr_2$. *J. Phys. I France* **2**, 89–99 (1991).

[35] M. S. Nam, S. J. Blundell, A. Ardavan, J. A. Symington & J. Singleton. Fermi surface shape and angle-dependent magnetoresistance oscillations. *J. Phys.: Condens. Mat.* **455**, 952–955 (2008).

[36] M. H. Cohen & L. M. Falicov. Magnetic breakdown in crystals. *Phys. Rev. Lett.* **7**, 231 (1961).

[37] K.-T. Wilke. *Kristallzuechtung* (Verlag Harri Deutsch, Thun, 1988).

[38] G. Adachi & N. Imanaka. The binary rare earth oxides. *Chem. Rev.* **98**, 1479 (1998).

[39] I.Tanaka, N. Komai & H. Kojima. Phase equilibrium in the Nd-Ce-Cu-O system. *Physica C* **190**, 112 (1991).

[40] Y. Hidaka & M. Suzuki. Growth and anisotropic superconducting properties of $Nd_{2-x}Ce_xCu0_{4-\delta}$ single crystals. *Nature* **338**, 635–637 (1989).

[41] A. ERB, E. WALKER & R. FLUKIGER. The use of $BaZrO_3$ crucibles in crystal growth of the high-T_c superconductors : Progress in crystal growth as well as in sample quality. *Physica C* **258**, 9–20 (1996).

[42] A. N. Maljuk, A. A. Jokhov, I. G. Naumenko, I. K. Bdikin, S. A. Zver'kov & G. A. Emel'chenko. Growth and characterization of bulk $Nd_{2-x}Ce_xCuO_4$ single crystals. *Physica C* **329**, 51 (2000).

[43] M. Matsuda, Y. Endoh & Y. Hidaka. Crystal growth and characterization of $Pr_{2-x}Ce_xCuO_4$. *Physica C* **179**, 347 (1991).

[44] T. Uefuji, K. Kurahashi, M. Fujita, M. Matsuda & K. Yamada. Electron doping effect on magnetic order and superconductivity in $Nd_{2-x}Ce_xCuO_4$ single crystals. *Physica C* **273**, 378–381 (2002).

[45] K. Kurahashi, H. Matsushita, M. Fujita & K. Yamada. Heat treatment effects on the superconductivity and crystal structure of $Nd_{1.85}Ce_{1.15}CuO_4$ studied using a single crystal. *J. Phys. Soc. Jap.* **71**, 910 (2002).

[46] V. Pankov, N. Kalanda, V. Truchan, D. Zhigunov & O. Babushkin. Oxygen nonstoichiometry and superconductivity of the $Nd_{2-x}Ce_xCuO_{4-\delta}$ single crystal. *Physica C* **377**, 521 (2002).

[47] J. S. Kim & D. R. Gaskell. The phase stability diagrams for the systems $Nd_2CuO_{4-\delta}$ and $Nd_{1.85}Ce_{0.15}CuO_{4-\delta}$ single crystal. *Physica C* **209**, 381 (1993).

[48] Y. Ando, G. S. Boebinger, A. Passner, L. F. Schneemeyer, T. Kimura, M. Okuya, S. Watauchi, J. Shimoyama, K. Kishio, K. Tamasaku, N. Ichikawa & S. Uchida. Resistive upper critical fields and irreversibility lines of optimally doped high-Tc cuprates. *Phys. Rev. B* **60**, 12475 (1999).

[49] Y. Wang, L. Li & N. P. Ong. Nernst effect in high-Tc superconductors. *Phys. Rev. B* **73**, 024510 (2006).

[50] . K. Andersen, A. I. Liechtenstein, . Jepsen & E. Paulsen. LDA energybands, low-energy Hamiltonians, t', t'', $t_\perp(\mathbf{k})$, and $J_\perp$. *J. Phys. Chem. Solids* **56**, 1573–1591 (1995).

[51] L. Mattheiss & D. Hamann. Electronic band properties of $CaSr_2Bi_2Cu_2O_8$. *Phys. Rev. B* **38**, 5012 (1988).

[52] J. M. Tranquada, D. E. Cox, W. Kunnmann, H. Moudden, G. Shirane, M. Suenaga, P. Zolliker, D. Vaknin, S. K. Sinha, M. S. Alvarez, A. J. Jacobson, & D. C. Jonhston. Neutron-diffraction determination of antiferromagnetic structure of Cu ions in $YBa_2Cu_3O_{6+x}$ with $x = 0.0$ and 0.15. *Phys. Rev. Lett.* **60**, 156 (1988).

[53] D. Vaknin, S. K. Sinha, D. E. Moncton, D. C. Johnston, J. M.Newsam, C. R. Safinya, & H. E. King. Antiferromagnetism in La_2CuO_{4-y}. *Phys. Rev. Lett.* **58**, 2802 (1987).

[54] M. Matsuura, P. Dai, H. J. Kang, J. W. Lynn, D. N. Argyriou, K. Prokes, Y. Onose & Y. Tokura. Effect of a magnetic field on the long-range magnetic order in insulating Nd_2CuO_4 and nonsuperconducting and superconducting $Nd_{1.85}Ce_{0.15}CuO_4$. *Phys. Rev. B* **68**, 144503 (2003).

[55] M. Matsuda, K. Yamada, K. Kakurai, H. Kadowaki, T. R. Thurston, Y. Endoh, Y. Hidaka, R. J. Birgeneau, M. A. Kastner, P. M. Gehring, A. H. Moudden & G. Shirane. Three-dimensional magnetic structures and rare earth magnetic ordering in Nd_2CuO_4 and Pr_2CuO_4. *Phys. Rev. B* **42**, 10098 (1990).

[56] M. Matsuda, Y. Endoh, K. Yamada, H. Kojima, I. Tanaka, R. J. Birgeneau, M. A. Kastner & G. Shirane. Magnetic order, spin correlations and superconductivity in single-crystal $Nd_{1.85}Ce_{0.15}CuO_{4-\delta}$. *Phys. Rev. B* **45**, 12548 (1992).

[57] E. Manousakis. The spin-1/2 Heisenberg antiferromagnet on a square lattice and its application to the cuprous oxides. *Rev. Mod. Phys.* **63**, 1 (1991).

[58] Y. Endoh, M. Matsuda, K. Yamada, K. Kakurai, Y. Hidaka, G. Shirane & R. J. Birgenau. Two-dimensional spin correlations and successive magnetic phase transitions in Nd_2CuO_4. *Phys. Rev. B* **40**, 7023 (1989).

[59] S. Skanthakumar, J. W. Lynn, J. L. Peng & Z. Y. Li. Observation of noncollinear magnetic structure for the Cu spins in Nd_2CuO_4-type systems. *Phys. Rev. B* **47**, 6173 (1993).

[60] A. Erb, B. Greb & G. Müller-Vogt. In-situ resistivity measurements during the oxygenation of $YBa_2Cu_3O_{7-\delta}$ and $Gd_{0.8}Y_{0.2}Ba_2Cu_3O_{7-\delta}$ single crystals. *Physica C* **259**, 83–91 (1996).

[61] M. Kläser, J. Kaiser, F. Stock, G. Müller-Vogt & A. Erb. Comparative study of oxygen diffusion in rare earth $REBa_2Cu_3O_{7-\delta}$ single crystals (RE = Y, Er, Dy) with different impurity levels. *Physica C* **306**, 188–198 (1998).

[62] M. Wagenknecht, D. Koelle, R. Kleiner, S. Graser, N. Schopohl, B. Chesca, A. Tsukada, S. T. B. Goennenwein & R. Gross. Phase diagram of the electron-doped $La_{2-x}Ce_xCuO_4$ cuprate superconductor from Andreev bound states at grainboundary Junctions. *Phys. Rev. Lett.* **100**, 227001 (2008).

[63] Y. Dagan, M. Qazilbash, C. P. Hill, V. N. Kulkarni & R. L. Greene. Evidence of quantum phase transition in $Pr_{2-x}Ce_xCuO_{4-\delta}$ from transport measurements. *Phys. Rev. Let.* **92**, 167001 (2004).

[64] X. H. Chen, T. Wu, C. H. Wang, G. Wu, D. F. Fang, J. L. Luo & G. T. Liu. Giant anisotropy and scaling behavior of magnetoresistance in antiferromagnetic $Nd_{2-x}Ce_xCuO_4$. *arxiv:0707.0104v2* (2007).

[65] W. Yu, J. S. Higgins, P. Bach & R. L. Greene. Transport evidence of a magnetic quantum phase transition in electron-doped high-temperature superconductors. *Phys. Rev. B* **76**, 020503 (2007).

[66] H. J. Kang, P. Dai, J. W. Lynn, M. Matsuura, J. R. Thompson, S.-C. Zhang, D. N. Argyriouk, Y. Onose & Y. Tokura. Antiferromagnetic order as the competing ground state in electron-doped $Nd_{2-x}Ce_xCuO_4$. *Nature* **423**, 522 (2003).

[67] Z. Z. Wang, T. R. Chien, N. P. Ong, J. Tarascon & E. Wang. Positive Hall coefficients observed in single-crystal $Nd_{2-x}Ce_xCuO_{4-\delta}$ at low temperatures. *Phys. Rev. B* **43**, 3020 (1991).

[68] L. Jia, X. Yan & X. Chen. Growth of semiconducting Nd_2CuO_4 and as-grown superconductive $Nd_{1.85}Ce_{0.15}CuO_{4-\delta}$ single crystals $Nd_{2-x}Ce_xCuO_4$. *J. Crystal Growth* **254**, 437–442 (2003).

[69] C. Bergemann, A. P. Mackenzie, S. R. Julian, D. Forsythe & E. Ohmichi. Quasi-two-dimensional Fermi-liquid properties of the unconventional superconductor Sr_2RuO_4. *Adv. Phys.* **52:7**, 639–725 (2003).

[70] A. S. Alexandrov. Theory of quantum magneto-oscillations in underdoped cuprate superconductors. *J. Phys.: Condens. Matter* **20**, 192202 (2008).

[71] A. Zimmers, J. M. Tomczak, R. P. S. M. Lobo, N. Bontemps, C. P. Hill, M. C. Barr, Y. Dagan, R. L. Greene, A. J. Millis & C. C. Homes. Infrared properties of electron-doped cuprates: Tracking normal-state gaps and quantum critical behavior in $Pr_{2-x}Ce_xCuO_4$. *Europhys. Lett.* **70**, 225–231 (2005).

[72] E. M. Motoyama, G. Yu, I. M. Vishik, O. P. Vajk, P. K. Mang & M. Greven. Spin correlations in the electron-doped high-transition-temperature superconductor $Nd_{2-x}Ce_xCuO_{4-\delta}$. *Nature* **445**, 187–189 (2007).

[73] P. Li, F. F. Balakirev & R. L. Greene. High-field Hall resistivity and magnetoresistance of electron-doped $Pr_{2-x}Ce_xCuO_{4-\delta}$. *Phys. Rev. Let.* **99**, 047003 (2007).

[74] I. W. Sumarlin, J. W. Lynn, T. Chattopadhyay, S. N. Barilo, D. I. Zhigunov & J. L. Peng. Magnetic structure and spin dynamics of the Pr and Cu in Pr2CuO4. *Phys. Rev. B* **51**, 5824–5839 (1995).

[75] W.-Q. Chen, K.-Y. Yang, T. M. Rice & F. C. Zhang. Quantum oscillations in magnetic field induced antiferromagnetic phase of underdoped cuprates: Application to ortho-II $YBa_2Cu_3O_{6.5}$. *Europhys. Lett.* **82**, 17004 (2008).

[76] P. A. Lee. From high temperature superconductivity to quantum spin liquid: progress in strong correlation physics. *arxiv:0708.2115v2* (2007).

8 Acknowledgments

At the end of this work I would like to express my gratitude to the persons, who made this work possible.

First of all it is Dr. Mark Kartsovnik whom I am deeply grateful for being my teacher, advisor and fellow during the last year. He supported me with his great expertize and perpetual patience.

Special thanks also to Dr. Michael Lambacher for teaching me many experimental skills that made me come this far.

I would like to thank Dr. Andreas Erb for accepting me as his diploma student and teaching me in the field of crystal growth.

I would like to thank Prof Dr. Rudolf Gross for introducing me to the High-T_c group.

Of course, I would like to thank Dr. Werner Biberacher, Dr. Mark Kartsovnik and Dr. Andreas Erb for their many helpful advices.

Many thanks to the staff of the Walther-Meissner-Institut and the Kristalllabor of the faculty of physics TU Munich who, without exception, helped us when- and wherever manual skills or material have been necessary.

Many thanks to the fellow students and scientists in the institute for their help in case of need and the nice working atmosphere.

I would like to thank the staff in the Dresden and Grenoble High Field Laboratories, as without them the new results of this thesis could not have been obtained.

Thank you Marika Wagner for accepting me the way I am and for being my second half.

Erklärung

des Diplomanden

Name:

Vorname:

Mit der Abgabe der Diplomarbeit versichere ich, dass ich die Arbeit selbständig verfasst und keine anderen als die angegebenen Quellen und Hilfsmittel benutzt habe.

....

(Ort, Datum) (Unterschrift)